DEPARTMENT OF TECHNOLOGY
BUFFALO PUBLIC LIBRARY

JOURNAL OF THE AERONAUTICAL SCIENCES

VOLUME 18 NOVEMBER, 1951 NUMBER 11

CONTENTS

Some Results of Sweptback Wing Structural Studies.....A. L. LANG AND R. L. BISPLINGHOFF 705

Gyro Pickoff Indications at Arbitrary Plane Attitudes.....LEONARD BECKER 718

Effect of Turbulence Level of Incident Air Stream on Local Heat Transfer and Skin Friction on a Cylinder.....W. H. GIEDT 725

On the Stability of Two-Dimensional Laminar Jet Flow of Gas.....S. I. PAI 731

Interrelationship Between Boundary Layer and Base Pressure.....H. H. KURZWEG 743

Shear Center for Thin-Walled Open Sections Beyond the Elastic Limit.....G. H. HANDELMAN 749

The Effect of Flight and Configuration Variables on Thermal Stresses in Diamond-Shaped Supersonic Wings.....FRANKLIN P. DURHAM 755

Readers' Forum: "A Simple Graphical Method for Constructing Families of Nyquist Diagrams," by Robert M. Stewart; "Strength of Reflected Shock in Mach Reflection," by H. S. Tan; "A Simple Rule for the Velocity Rise with Subsonic Mach Number on Ellipsoids of Revolution," by D. Küchemann; "On Slender Wing Theory," by John W. Miles; "Proper Use of the M.I.T. Tables for Supersonic Flow Past Inclined Cones," by Antonio Ferri; "Visualization of Boundary-Layer Flow," by James S. Murphy and Ralph E. Phinney; "Local Compressible Pressure Coefficient," by V. G. Szebehely; "The Effect of Compressibility of the Material on Plastic Buckling Stresses," by Elbridge Z. Stowell and Richard A. Pride; "An Integral Relation from the Turbulent Energy Equation," by Stanley Corrsin; "Concerning Hadamard's Solution for a Source in Supersonic Flow," by E. V. Laitone; "On the Unsteady Motion of a Thin Rectangular Wing in Supersonic Flow" by N. Rott.....767–776

Published by the

INSTITUTE OF THE AERONAUTICAL SCIENCES, INC.

JOURNAL OF THE AERONAUTICAL SCIENCES

Editor: HUGH L. DRYDEN, *Director, N.A.C.A.*

Associate Editor: ROBERT R. DEXTER *Managing Editor:* BERNEICE H. JARCK

Editorial Committee

Aerodynamics

Francis Clauser
Howard Emmons
Alexander Flax
R. Paul Harrington
R. T. Jones
Carl Kaplan
H. W. Liepmann
C. C. Lin
H. F. Ludloff
Harold Luskin
John R. Markham
Clark B. Millikan
Shatswell Ober
W. Bailey Oswald
Allen E. Puckett
Elliott G. Reid
H. J. F. Reid
Russell Robinson
G. B. Schubauer
W. R. Sears
John Stack
Theodore von Kármán
Richard von Mises

Flight Testing

W. K. Ebel
R. R. Gilruth
Melvin N. Gough
E. G. Stout

Meteorology

C. F. Brooks
D. M. Little
E. I. Minser
F. W. Reichelderfer
H. C. Willett

Structures and Materials

W. B. Bleakney
E. W. Conlon
L. H. Donnell
E. C. Hartmann
N. J. Hoff
Samuel Levy
E. E. Lundquist
J. S. Newell
Alfred S. Niles
W. Ramberg
E. Reissner
F. R. Shanley
H. W. Sibert
C. R. Strang
S. Timoshenko
H. S. Tsien
Chi-Teh Wang

Rotating Wing Aircraft

F. B. Gustafson
K. H. Hohenemser
Bartram Kelley
R. B. Maloy
Ralph McClarren
R. H. Miller
R. H. Prewitt
Igor I. Sikorsky

Physiologic Problems

H. G. Armstrong
Louis H. Bauer
Eugene Du Bois
W. Randolph Lovelace, II
Ross A. MacFarland
A. D. Tuttle

Flight Propulsion

George W. Brady
Frank W. Caldwell
L. S. Hobbs
E. E. Johnson
Joseph Keenan
R. P. Kroon
Hans Reissner
Abe Silverstein
C. Fayette Taylor
E. S. Taylor
P. Taylor
E. S. Thompson
H. S. Tsien

Aircraft Design

W. E. Beall
W. K. Ebel
Hall L. Hibbard
Richard Hutton
C. L. Johnson
A. A. Kartveli
C. J. McCarthy
Fred E. Weick
Robert J. Woods

Air Transport

Charles Froesch
J. A. Herlihy
R. D. Kelly
Otto E. Kirchner
Jerome Lederer
John C. Leslie
R. Dixon Speas

Instruments

Allan G. Binnie
W. G. Brombacher
Charles H. Colvin
E. M. Craig
C. S. Draper
S. O. Eskin
O. E. Esval
W. L. Howland
George H. Purcell
C. F. Savage
O. Hugo Schuck
L. N. Schwien
C. L. Seward, Jr.
L. D. Statham
R. C. Sylvander
D. K. Warner
P. F. Weber
Elmer P. Wheaton

Vibration and Flutter

Lee Arnold
M. A. Biot
R. L. Bisplinghoff
William Bollay
Chieh-Chien Chang
I. E. Garrick
Martin Goland
J. P. Den Hartog

Fuels and Oils

D. P. Barnard
J. H. Doolittle
Graham Edgar
R. T. Goodwin
S. D. Heron
A. M. Rothrock

SUBSCRIPTION RATES

JOURNAL OF THE AERONAUTICAL SCIENCES, Published Monthly.—United States and Possessions: 1 Year, $12.00; Single Copies, $1.50. Foreign Countries Including Canada (American Currency Rates): 1 Year, $13.00; Single Copies, $1.50.

AERONAUTICAL ENGINEERING REVIEW, Published Monthly.—United States and Possessions: 1 Year, $3.00; Single Copies, $0.50. Foreign Countries Including Canada (American Currency Rates): 1 Year, $3.50; Single Copies, $0.50.

Notices of change of address should be sent to the Institute at least 30 days prior to actual change of address.

Manuscripts for publication, proofs, and all correspondence should be addressed to the Editorial Office of the JOURNAL.

Correspondence regarding subscriptions may be addressed to Publication Office, 20th and Northampton Sts., Easton, Pa., or to the Editorial Office of the JOURNAL OF THE AERONAUTICAL SCIENCES, 2 East 64th Street, New York 21, New York.

Copyright, 1951, by the Institute of the Aeronautical Sciences, Inc.

Entered as Second Class Matter at the Post Office, Easton, Pa., May 1, 1937. Acceptance for mailing at a special rate of Postage provided for in the Act of August 24, 1912. Authorized April 29, 1937.

JOURNAL OF THE AERONAUTICAL SCIENCES

VOLUME 18 NOVEMBER, 1951 NUMBER 11

Some Results of Sweptback Wing Structural Studies

A. L. LANG* AND R. L. BISPLINGHOFF†

Massachusetts Institute of Technology

SUMMARY

Static stress and deflection tests have been conducted in the laboratory on a 45° sweptback single-cell beam. The results of these tests are compared with simplified theories for predicting stresses and deformations in swept shell beams. The agreement between theoretically and experimentally determined deflections is closer than the stresses, but both agree within acceptable engineering accuracy. Both cases of skewed ribs and ribs perpendicular to the spars are included. Since some degree of root support deformation is unavoidable in sweptback wing static tests, a method is described of accounting for this effect in the theory.

NOTATION

A = corner flange area (except as used in matrices), in.^{2}
b = wing chord perpendicular to spars, in.
$C_T(x, \xi)$ = disturbance influence function due to the effect of sweep
$C_{ST}(x, \xi)$ = influence function associated with a straight wing clamped at the root
E = Young's modulus, lbs. per sq.in.
G = shear modulus (except as used in matrices), lbs. per sq.in.
h = depth of cross section, in.
I = cross-sectional moment of inertia, in.^{4} (also denotes unit matrix)
l = length of straight wing, in.
M = bending moment (vector perpendicular to spars), in.lb.
P = concentrated shear force, lb.
T = torque (vector parallel to spars), in.lb.
t_c = cover thickness, in.
t_w = web thickness, in.
U_e = potential energy of external loads, in.lb.
U_i = internal strain energy, in.lb.
v = vertical displacement, in.
α = beam slope, rad.
β = torsion-bending parameter, in.$^{-1}$
Γ = sweep back angle, deg.
φ = warping angle of cross section, rad.
σ = flange normal stress, lbs. per sq in.
τ = shear stress, lbs. per sq.in.
θ = twist of cross section, rad.

Presented at the Structures Session, Nineteenth Annual Meeting, I.A.S., New York, January 29–February 1, 1951.

*Engineer, Aero-Elastic and Structures Research, M.I.T.
†Associate Professor of Aeronautical Engineering, M.I.T.

(I) INTRODUCTION

THE CALCULATION OF THE STRESS distribution in the vicinity of the root of a sweptback shell beam is an extremely difficult problem. Solutions to the exact equations are obtainable by numerical methods, but they are much too cumbersome for the designer. An approach is needed which is sufficiently comprehensive to yield the significant effects of sweep, yet simple enough to be usable by the structural designer. Experimental data have shown that the effects of the sweep which are of greater significance to the structural engineer are the concentration of normal and shear stresses at the root of the rear spar, and the coupling induced by the sweep between bending and torsional deflections.

Little theoretical and experimental data have been published by the sweptback wing structural problem. Levy[1] described a method of computing stresses and deflections in swept wings with ribs parallel to the air stream. This method consisted of breaking the structure into its elements and determining the internal forces by solving the equilibrium equations plus additional equations determined from the principle of minimum strain energy. Thompson and Wittrick[2, 3] present a scheme based on the work of Hadji-Argyris for calculating the stress distribution in a swept tube with rigid ribs parallel to the air stream. Goodman[4] presents a computation of the stress distribution in a sweptback sheet based upon the methods of reference 1. Zender and Libove[5] and Zender and Heldenfels[6] give excellent and useful experimental data on the behavior of a 45° sweptback box beam subjected to bending and torsion. In their latest paper, Heldenfels, Zender, and Libove[7] present methods for the analysis of a 45° swept box beam with ribs perpendicular to the spars and with an

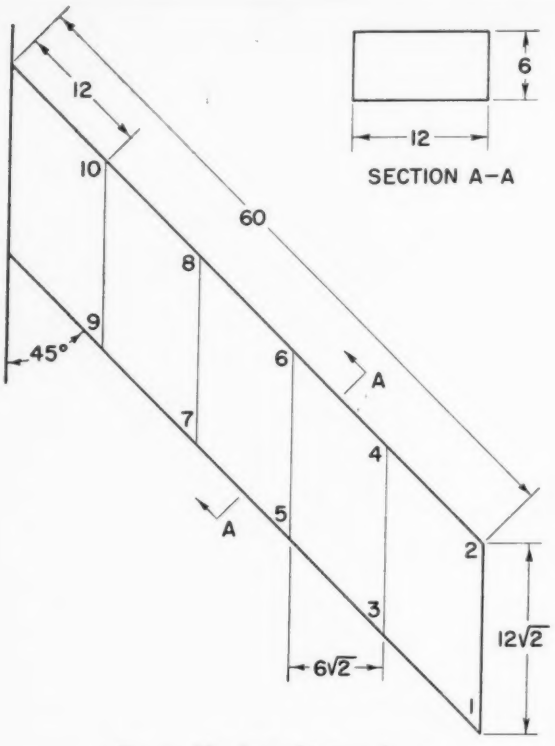

FIG. 1. Plan form of test specimen.

FIG. 2. Test specimen.

elastic carry-through structure. This paper, which has recently come to the attention of the authors, employs methods and reaches conclusions similar to those presented in the present paper. These eight papers, outside of the M.I.T. Report[8] upon which the present paper is based, seem to comprise the main published theoretical and experimental literature on the swept shell beam problem.

The purpose of the present paper is to compare known methods of analysis with experimental data and to present simplified methods that can be applied to a single-cell shell beam. In the first part of the paper, laboratory experiments on a 45° sweptback beam are described in which both stresses and deflections were measured. The remainder of the paper is devoted to analysis of the test specimen and comparison of theoretical and experimental results. At first, a modification of the method proposed by Levy in reference 1 is applied. Secondly, a method based upon the principle of minimum potential energy is applied. Finally, a simplified approach is suggested which can be used in preliminary design.

(II) Test Specimen

The plan form and cross section of the sweptback wing specimen used in the present investigation are illustrated in Fig. 1, and a photograph is shown in Fig. 2. The specimen is a stressed skin, single-cell box swept back at 45°. The two spars are parallel and of equal cross section along the span. Top and bottom surfaces are identical. Each spar flange is composed of two $^3/_4$ by $^3/_4$ by $^1/_8$ 24-ST extruded angles back to back and separated by the spar webs. Three equally spaced $^1/_2$ by $^1/_2$ by $^1/_{16}$ 24-ST extruded angles are used as longitudinal stiffeners on the upper and lower skins. Six solid ribs parallel to the wind stream are spaced $6\sqrt{2}$ in. along a line normal to the airplane centerline. The webs and ribs are 0.051-in. 75 ST sheet, and the upper and lower skins are 0.032-in. 75 ST sheet. The overall length of the wing specimen measured parallel to the spars is 60 in. The section inboard of the inner rib is built around a heavy steel attachment fitting as shown by Fig. 3.

(III) Static Tests

The objectives of the static tests of the sweptback wing were to obtain experimental data for purposes of comparison with theory. In the present paper, the experimental determination of the following are included:

(a) Nine by nine matrix of flexibility influence coefficients.

(b) Normal and shear stresses in the flanges and webs due to a single load applied midway between Stations 2 and 3 (cf. Fig. 1).

Fig. 3 illustrates the arrangement employed in the static tests. Vertical deflections were measured by dial gages attached to a fixed supporting structure above the

wing. Stresses were measured at 43 points on the flanges and webs by means of electric strain gages. The gages were mounted longitudinally along the flanges to measure the normal stresses and at 45° to the vertical on the webs to measure the shear stresses. The majority of the gages were located in the vicinity of the root.

The wing was loaded by a single hydraulic jack. The procedure for determining the matrix of influence coefficients consisted of applying a 1,000-lb. load at points 2 to 10 (cf. Fig. 1) and recording the nine dial gage readings for each point of load application. This procedure yields 81 numbers, which form the square matrix of flexibility influence coefficients for the wing denoted by $[C]_{9\times 9}$.

In conducting static tests on sweptback wings at M.I.T., it has been found that it is difficult to design and construct a root fitting that provides anything approximating complete root fixity. The fitting finally selected shown by Fig. 3 did not provide sufficient root fixity so that its elastic effects could be neglected completely. Root fitting deformations have a significant effect on the wing deflections and a somewhat lesser effect on the stresses. Corrections for both effects should be introduced in the comparison between theory and experiment. In the present method of correction, experimentally determined data on root deflections are introduced into the theoretical computation of the stresses and deflections. This experimental data is represented by four column matrixes as follows:

$$\{C_{2F}{}^{\delta P} \ \dots \ C_{10F}{}^{\delta P}\}, \quad \{C_{2R}{}^{\delta P} \ \dots \ C_{10R}{}^{\delta P}\}, \quad \{C_{2F}{}^{\alpha P} \ \dots \ C_{10F}{}^{\alpha P}\}, \quad \{C_{2R}{}^{\alpha P} \ \dots \ C_{.0R}{}^{\alpha P}\}$$

The elements of these matrices are defined as follows:

$C_{iF}{}^{\delta P}$ = front spar deflection at root due to unit load at Station 1

$C_{iR}{}^{\delta P}$ = rear spar deflection at root due to unit load at Station 1

$C_{iF}{}^{\alpha P}$ = front spar slope at root due to unit load at Station 1

$C_{iR}{}^{\alpha P}$ = rear spar slope at root due to unit load at Station 1

Linear root deformations were measured with 0.010-in. dial gages, and slopes were measured by means of an optical system. In the latter, a plane first surface mirror was attached to a bar pinned to the upper and lower flanges of the spar at the root. By means of a light beam, a hairline was projected onto the mirror and reflected to a screen.

(IV) Idealized Section

The swept-wing problem entails an investigation of secondary normal and shear stresses in the vicinity of the root. Because of the complexity of the theory necessary to investigate such effects, it is common to simplify the cross section in order to reduce the labor in obtaining a solution. Such simplifications are discussed, for example, in reference 9. In addition, the effective cross section will depend upon the type loading to which the structure is subjected. This effect, which has been neglected here, requires further investigation since it is not possible to separate bending and torsion effects near the root of a swept wing.

In constructing simplified sections in the present application, the cover skin is assumed fully effective. This assumption seems reasonable due to the relatively low magnitude of the applied loads in the static tests. Fig. 4 shows the actual wing section and the simplified section employed in the analyses.

(V) The Levy Method

(*a*) *General Remarks*

In general, for complex structures such as are sometimes found in the root regions of sweptback wings, the general principles described by Levy[1] are often the only tool that can be used to obtain a satisfactory solution. This is especially true when the yielding of elastic ribs forms an important part of the problem. Although the scheme used by Levy in setting up the problem of a swept wing with ribs parallel to the air stream leads to incorrect results, the case of ribs perpendicular to the spars can be readily handled.

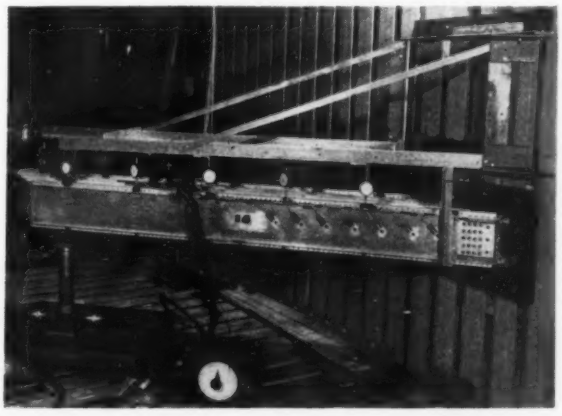

Fig. 3. Arrangement for deflection and stress measurement of test specimen

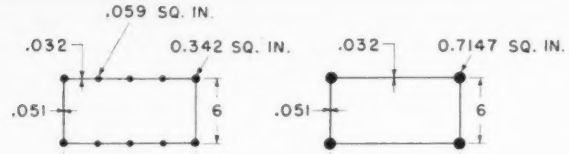

FIG. 4. Simplification of cross section perpendicular to spars.

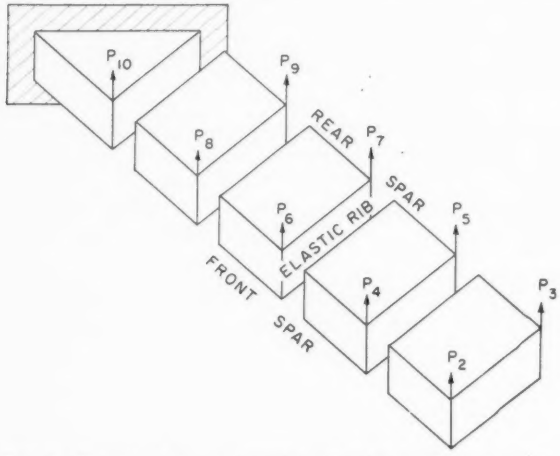

FIG. 5. Structural segments and loading for analysis of swept-back wing by the Levy method.

(b) *Application to a Swept Wing with Elastic Ribs Perpendicular to the Spars*

As an illustration, the 45° sweptback wing described in Section (II) is analyzed as though its ribs are perpendicular to the spars. Fig. 5 illustrates schematically the assumed loading and the manner in which the elastic ribs divide the wings into segments. Using the methods of reference 1, the wing may be broken up into structural units, and each unit can be put into equilibrium with internal forces. This results in the diagram shown in Fig. 6. In this diagram, each sheet and stringer is in equilibrium, and 15 unknown internal forces $a_1 \ldots a_{15}$ have been introduced. The stress distribution is completely known when these 15 values are determined. By inspection of Fig. 6, it is clear that nine equations of equilibrium can be written as follows:

$$\{P_2 \ldots P_{10}\} = [T]\{a_1 \ldots a_{15}\} \tag{1}$$

The system has six redundants, and six additional equations must be derived by applying the principle of minimum strain energy.

In writing an expression for the total internal strain energy in the structure, three fundamental formulas are required. Two of these are given in reference 1 for the flanges and rectangular panels. In computing the internal strain energy in the triangular panel, it is assumed that the shear flow is uniform over its area. This approximation results in an expression for strain energy as follows:

$$U_i = 1.3(q^2A/Et) \tag{2}$$

where A is the triangular area and t is the skin thickness.

By means of the three fundamental formulas, the strain energy can be expressed in terms of the internal forces in the following bilinear form,

$$U_i = (1/2E)[a_1 \ldots a_{15}][F]\{a_1 \ldots a_{15}\} \tag{3}$$

Since it is necessary to express the strain energy in terms of the external forces and the six redundant members, the following equation is constructed from Eq. (1):

$$\{a_1 \ldots a_{15}\} = [G]\{P_2 \ldots P_{10}, a_2, a_5, a_8, a_{11}, a_{14}, a_{15}\} \tag{4}$$

Substituting Eq. (4) into Eq. (3),

$$U_i = 1/2E[P_2 \ldots P_{10}, a_2, a_5, a_8, a_{11}, a_{14}, a_{15}] \times [H]\{P_2 \ldots P_{10}, a_2, a_5, a_8, a_{11}, a_{14}, a_{15}\} \tag{5}$$

where $[H] = [G]'[F][G]$ and $[G]'$ is the transpose of $[G]$.

Applying the principle of minimum strain energy,

$$\partial U_i/\partial a_j = 0 \qquad (j = 2, 5, 8, 11, 14, 15) \tag{6}$$

the internal redundant forces are obtained,

$$\{a_2, a_5, a_8, a_{11}, a_{14}, a_{15}\} = [H_{aa}]^{-1}[H_{aP}]\{P_2 \ldots P_{10}\} \tag{7}$$

The matrices $[H_{aa}]^{-1}$ and $[H_{aP}]$ are found by partitioning $[H]$ as follows,

$$[H] = \begin{bmatrix} [H_{PP}]_{9\times 9} & [H_{Pa}]_{9\times 6} \\ \hline [H_{aP}]_{6\times 9} & [H_{aa}]_{6\times 6} \end{bmatrix} \tag{8}$$

Substituting the result given by Eq. (7) into Eq. (4), the stress distribution can be seen to be

$$\{a_1 \ldots a_{15}\} = [S]\{P_2 \ldots P_{10}\} \tag{9}$$

where

$$[S] = [G]\begin{bmatrix} [I]_{9\times 9} \\ \hline -[H_{aa}]^{-1}[H_{aP}] \end{bmatrix}$$

Substituting the result given by Eq. (7) into Eq. (5) and using the relation,

$$U_i = {}^1/_2[P_2 \ldots P_{10}][C]\{P_2 \ldots P_{10}\} \tag{10}$$

where $[C]$ is the matrix of flexibility influence coefficients, there results for $[C]$

$$[C] = (1/E)\left[[H_{PP}] - [H_{Pa}][H_{aa}]^{-1}[H_{aP}]\right] \tag{11}$$

The 15 by 9 matrix for the internal load distribution and the 9 by 9 matrix of flexibility influence coefficients can be obtained from the partitioned members of the strain energy matrix $[H]$.

(c) *Corrections for Root Deformations*

Because of the impracticability of constructing a root fitting that completely suppresses root deformations, it is necessary to include these effects when comparing theory with swept-wing experimental data. In the present case, this is done by introducing experimentally determined root stiffnesses into the analysis carried out above. This results in corrected expressions for Eqs. (9) and (11).

Using the experimentally determined column matrices from Section (III), the linear and angular deflections at the root of the front and rear spars are

$$\delta_F = [P_2 \ldots P_{10}] \left\{ C_{2F}{}^{\delta P} \ldots C_{10F}{}^{\delta P} \right\} \quad (12)$$

$$\delta_R = [P_2 \ldots P_{10}] \left\{ C_{2R}{}^{\delta P} \ldots C_{10R}{}^{\delta P} \right\} \quad (13)$$

$$\alpha_F = [P_2 \ldots P_{10}] \left\{ C_{2F}{}^{\alpha P} \ldots C_{10F}{}^{\alpha P} \right\} \quad (14)$$

$$\alpha_R = [P_2 \ldots P_{10}] \left\{ C_{2R}{}^{\alpha P} \ldots C_{10R}{}^{\alpha P} \right\} \quad (15)$$

The root reactions can be expressed in terms of the internal forces,

$$R_F = [T_F] \{a_1 \ldots a_{15}\} \quad (16)$$

$$R_R = [T_R] \{a_1 \ldots a_{15}\} \quad (17)$$

$$V_F = [S_F] \{a_1 \ldots a_{15}\} \quad (18)$$

$$V_R = [S_R] \{a_1 \ldots a_{15}\} \quad (19)$$

where

R_F = flange force in front spar at root
R_R = flange force in rear spar at root
V_F = vertical shear on front web at root
V_R = vertical shear on rear web at root

$$[T_F] = [2 -8 \ 0 \ 2 -6 \ 0 \ 2 -4 \ 0 \ 2 -2 \ 0 \ 2 \ 0 -2]$$

$$[T_R] = [2 -8 \ 0 \ 2 -6 \ 0 \ 2 -4 \ 0 \ 2 -2 \ 0 \ 0 \ 0 \ 0]$$

$$[S_F] = [0 \ 0 \ 0 \ 0 \ 0 \ 0 \ 0 \ 0 \ 0 \ 0 \ 0 \ 0 \ 1 \ 0 \ 0]$$

$$[S_R] = [0 \ 0 \ 0 \ 0 \ 0 \ 0 \ 0 \ 0 \ 0 \ 0 \ 0 \ 1 \ 0 \ 1 \ 0] .$$

The total internal strain energy in the wing plus root fitting is given by

$$\bar{U}_i = U_i + (1/2)[h\alpha_F \quad h\alpha_R \quad \delta_F \quad \delta_R] \{R_F \quad R_R \quad V_F \quad V_R\} \quad (20)$$

where U_i is given by Eq. (3). Introducing Eqs. (12) to (19) into Eq. (20) yields

$$\bar{U}_i = (1/2E)[P_2 \ldots P_{10}, a_2, a_5, a_8, a_{11}, a_{14}, a_{15}][\bar{H}] \{P_2 \ldots P_{10}, a_2, a_5, a_8, a_{11}, a_{14}, a_{15}\} \quad (21)$$

where $[\bar{H}] = [H] + [H_1]$ and $[H_1]$ is given by

$$[H_1] = E\left[h\left\{C_{2F}{}^{\alpha P} \ldots C_{10F}{}^{\alpha P}, 0, 0, 0, 0, 0, 0\right\} [T_F] + h \left\{C_{2R}{}^{\alpha P} \ldots C_{10R}{}^{\alpha P}, 0, 0, 0, 0, 0, 0\right\} [T_R] + \left\{C_{2F}{}^{\delta P} \ldots C_{10F}{}^{\delta P}, 0, 0, 0, 0, 0, 0\right\} [S_F] + \left\{C_{2R}{}^{\delta P} \ldots C_{10R}{}^{\delta P}, 0, 0, 0, 0, 0, 0\right\} [S_R]\right] [G]$$

The matrix $[H_1]$ has the following form,

$$[H_1] = \left[\begin{array}{c|c} [H_{PP}]_{9 \times 9} & [H_{Pa}]_{9 \times 6} \\ \hline [H_{aP}]_{6 \times 9} & [0]_{6 \times 6} \end{array}\right] \quad (22)$$

In general, $[H_1]$ will not be symmetrical, but can be made symmetrical by putting

$$a_{ij} = a_{ji} = (A_{ij} + A_{ji})/2 \quad (23)$$

where

a_{ij} = an element of $[H_1]$ symmetrical
A_{ij} = an element of $[H_1]$ unsymmetrical

Referring to the results given by Eqs. (9) and (11), it can be seen that the corrected stress and influence coefficient matrices are given by

$$[S] = [G] \left[\begin{array}{c} [I]_{9 \times 9} \\ \hline -[\bar{H}_{aa}]^{-1}[\bar{H}_{aP}] \end{array}\right] \quad (24)$$

$$[\bar{C}] = 1/E \ [[\bar{H}_{PP}] - [\bar{H}_{Pa}][\bar{H}_{aa}]^{-1}[\bar{H}_{aP}]] \quad (25)$$

It should be observed that $[\bar{H}_{aa}] = [H_{aa}]^{-1}$ so that further matrix inversion is unnecessary when including root deformations in the analysis.

(d) *Comparison of Experiment and Theory*

The results of applying Eqs. (24) and (25) to the 45° sweptback wing are compared with experimental data from the test specimen. This comparison is not completely justified since the rib direction assumed in the analysis is perpendicular to the spars, whereas the rib direction in the test specimen is parallel to the air stream.

Figs. 7 and 8 compare flange normal stresses and web shear stresses for a unit shear force applied midway between Stations 2 and 3. Fig. 9 compares front and rear spar deflections for a unit load applied at Station 2.

In comparing these results, it can be seen that the agreement in deflections is somewhat better than the agreement in stresses. It is important to observe that the assumption of constant shear stress over each bay does not permit the theory to predict the critical root shear stress in the rear spar. On the other hand, the assumption of a linearly varying normal stress yields results that compare favorably with theory at the root of the rear spar.

(VI) The Method of Minimum Potential Energy

(a) Application to a Swept Wing with Ribs Perpendicular to the Spars

When it is assumed that all ribs are rigid except the root rib, the method of minimum potential energy can be conveniently applied. It can, of course, be applied also to the elastic rib case, but it is somewhat more tedious than the method of minimum strain energy (Levy method).

Fig. 10 illustrates the loading that is assumed in the present application. The wing shown in Fig. 10 is assumed to have nineteen degrees of freedom which completely define its strained configuration. These consist of a linear and two angular displacements at the juncture of the elastic rib with the front spar (γ_0, α_0, and v_0), and four displacements at each of the four loading stations. These four displacements are slope, angle of twist, warping, and vertical displacement denoted by α_i, θ_i, φ_i, and v_i, respectively. Fig. 11 illustrates positive displacements.

The internal strain energy in terms of the linear and angular displacements can be written in the following matrix form,

$$U_i = 1/2[v_1 \ldots v_4, \theta_1 \ldots \theta_4, \alpha_1 \ldots \alpha_4, \varphi_1 \ldots \varphi_4, v_0, \alpha_0, \gamma_0][K] \times \{v_1 \ldots v_4, \theta_1 \ldots \theta_4, \alpha_1 \ldots \alpha_4, \varphi_1 \ldots \varphi_4, v_0, \alpha_0, \gamma_0\} \quad (26)$$

The potential energy of the external loads in matrix form is given by

$$U_e = -[P_1 \ldots P_4, T_1 \ldots T_4]\{v_1 \ldots v_4, \theta_1 \ldots \theta_4\} \quad (27)$$

The total potential energy is given by,

$$U = U_i + U_e \quad (28)$$

Applying the principle of minimum potential energy,

$$\delta U = 0 \quad (29)$$

there is obtained,

$$[K]\{v_1 \ldots v_4, \theta_1 \ldots \theta_4, \alpha_1 \ldots \alpha_4, \varphi_1 \ldots \varphi_4, v_0, \alpha_0, \gamma_0\} = \{P_1 \ldots P_4, T_1 \ldots T_4, 0\,0\,0\,0\,0\,0\,0\,0\,0\,0\,0\} \quad (30)$$

Inverting the matrix $[K]$, Eq. (30) becomes,

$$\{v_1 \ldots v_4, \theta_1 \ldots \theta_4, \alpha_1 \ldots \alpha_4, \varphi_1 \ldots \varphi_4, v_0, \alpha_0, \gamma_0\} = [C]\{P_1 \ldots P_4, T_1 \ldots T_4, 0\,0\,0\,0\,0\,0\,0\,0\,0\,0\,0\} \quad (31)$$

The matrix $[C]$ can be partitioned as follows,

$$[C] = \left[\begin{array}{c|c} [C_{11}]_{8\times 8} & [C_{12}]_{8\times 11} \\ \hline [C_{21}]_{11\times 8} & [C_{22}]_{11\times 11} \end{array}\right] \quad (32)$$

where

$$[C_{12}]_{8\times 11} = [C_{21}]'_{11\times 8}$$

The 8 by 8 matrix in the upper left-hand corner, $[C_{11}]_{8\times 8}$, is of most interest in problems involving calculations of deformations of the wing and in problems in dynamics. The elements of this matrix represent the linear and angular displacements at the i^{th} section due to unit force or torque at the j^{th} station.

In determining the matrix $[C_{11}]_{8\times 8}$, it is not necessary to invert the entire $[K]$ matrix. It is observed that the $[K]$ matrix can be partitioned as follows:

$$[K] = \left[\begin{array}{c|c} [K_{11}]_{8\times 8} & [K_{12}]_{8\times 11} \\ \hline [K_{21}]_{11\times 8} & [K_{22}]_{11\times 11} \end{array}\right] \quad (33)$$

where

$$[K_{21}]_{11\times 8} = [K_{12}]_{8\times 11}'$$

The desired matrix of flexibility influence coefficients, $[C_{11}]_{8\times 8}$, can be written in terms of the partitioned elements of the $[K]$ matrix as follows,

$$[C_{11}]_{8\times 8} = [[K_{11}]_{8\times 8} - [K_{12}]_{8\times 11}\,[K_{22}]_{11\times 11}{}^{-1}\,[K_{21}]_{11\times 8}]^{-1} \tag{34}$$

Some simplification in the analysis is obtained if it can be assumed that the wing is composed of an infinite number of closely spaced rigid ribs outboard of Station 1 (cf. Fig. 12). Fig. 12 illustrates the wing loaded at a station located a distance $x = \xi$ from the most inboard rigid rib. The deformations of the wing at a distance x are denoted by $v(x)$ and $\theta(x)$, and at the first station by v_1, α_1, θ_1, and φ_1. It is convenient to write the deformations at the point x as follows:

$$\{v(x)\theta(x)\} = \begin{bmatrix} 1 & x & 0 & 0 \\ 0 & 0 & 1 & K(x) \end{bmatrix} \{v_1\ \alpha_1\ \theta_1\ \varphi_1\} + \begin{bmatrix} 1 & 0 \\ 0 & 1 \end{bmatrix} \{\bar{v}(x)\bar{\theta}(x)\} \tag{35}$$

where $\bar{v}(x)$ and $\bar{\theta}(x)$ denote the deformations at the point x when it is assumed that the wing is rigidly clamped at the first station. The term $K(x)$ denotes the angle of twist at point x due to unit warping at Station 1, and is given by

$$K(x) = \frac{\beta AE}{8Gb}\left(\frac{b}{t_c} - \frac{h}{t_w}\right)\left(\sinh \beta x - \frac{\cosh \beta x - 1}{\coth \beta l}\right) \tag{36}$$

where

$$\beta^2 = 8G/[AE(b/t_c + h/t_w)]$$

The internal strain energy can be written in two parts,

$$U_i = 1/2[v_1\ \alpha_1\ \theta_1\ \varphi_1][K_1]\ \{v_1\ \alpha_1\ \theta_1\ \varphi_1\} + \bar{U}_i[\bar{v}(x), \bar{\theta}(x), \bar{\varphi}(x)] \tag{37}$$

where $\bar{U}_i$ is the internal strain energy associated with $\bar{v}(x)$, $\bar{\theta}(x)$, $\bar{\varphi}(x)$. The matrix $[K_1]$ is derived in Appendix (A).

The potential energy of the external loads is,

$$U_e = -[PMT]\begin{bmatrix} v_1 + \xi\alpha_1 \\ \alpha_1 \\ \theta_1 + K(\xi)\varphi_1 \end{bmatrix} - [PMT]\begin{bmatrix} v(\xi) \\ \bar{\alpha}(\xi) \\ \bar{\theta}(\xi) \end{bmatrix} \tag{38}$$

Applying the principle of minimum potential energy, there results two separate sets of equations,

$$[K_1]\ \{v_1\alpha_1\theta_1\varphi_1\} = [A]\ \{PMT\} \tag{39}$$

where

$$[A] = \begin{bmatrix} 1 & 0 & 0 \\ \xi & 1 & 0 \\ 0 & 0 & 1 \\ 0 & 0 & K(\xi) \end{bmatrix}$$

and

$$\left.\begin{array}{ll} x \le \xi & x \ge \xi \\ \dfrac{d\bar{v}(x)}{dx} = \dfrac{1}{EI}\left[Mx + Px\left(\xi - \dfrac{x}{2}\right)\right] + \dfrac{P}{2Ght_w} & \bar{v}(x) = \bar{v}(\xi) + \dfrac{d\bar{v}(\xi)}{dx}(x - \xi) \\ \bar{\theta}'(x) = \dfrac{2T}{Gbh(t_wb + t_ch)} + \dfrac{1}{b}\left(\dfrac{t_wb - t_ch}{t_ch + t_wb}\right)\bar{\varphi}(x) & \bar{\theta}'(x) = \dfrac{1}{b}\left(\dfrac{t_wb - t_ch}{t_ch + t_wb}\right)\bar{\varphi}(x) \\ \bar{\varphi}''(x) - \beta^2\bar{\varphi}(x) = -\dfrac{4}{AEbh^2}\left(\dfrac{t_wb + t_ch}{t_ch + t_wb}\right)T & \bar{\varphi}''(x) - \beta^2\bar{\varphi}(x) = 0 \end{array}\right\} \tag{40}$$

The solution of Eq. (39) yields the deformation of the system assuming that outboard of Station 1 the wing is completely rigid in bending and twisting but elastic in warping. The solutions of Eqs. (40) yield the elastic deformation of the wing outboard of Station 1 when it is assumed that the wing is completely clamped at Station 1.

The solution of Eq. (39) can be written as,

$$\{v_1\alpha_1\theta_1\varphi_1\} = [R]\{PMT\} \tag{41}$$

where

$$[K_1]^{-1}[A] = [R]$$

The solutions of Eqs. (40) can be written as,

$$\{\bar{v}(x)\bar{\theta}(x)\} = [\bar{C}(x, \xi)]\{PMT\} \tag{42}$$

where $[\bar{C}(x, \xi)]$ represents a matrix of influence functions resulting from solutions of Eqs. (40), and is a well-known result[10] for straight wings with warping restraint at the root.

Substituting the results of Eqs. (41) and (42) into the deformation Eq. (35), there is obtained,

$$\{v(x)\theta(x)\} = [[C_{ST}(x, \xi)] + [C_{\Gamma}(x, \xi)]]\{PMT\} \tag{43}$$

where

$$[C_{ST}(x, \xi)] = \begin{bmatrix} 1 & 0 \\ 0 & 1 \end{bmatrix}[\bar{C}(x, \xi)] \tag{44}$$

is the matrix of influence functions assuming that the wing is rigidly clamped at Station 1. Each term represents the linear or angular deflection at x due to a unit force or moment at ξ.

$$[C_{\Gamma}(x, \xi)] = \begin{bmatrix} 1 & x & 0 & 0 \\ 0 & 0 & 1 & K(x) \end{bmatrix}[R] \tag{45}$$

is the matrix of influence functions assuming that the wing is rigid in bending and twisting but elastic in warping outboard of Station 1.

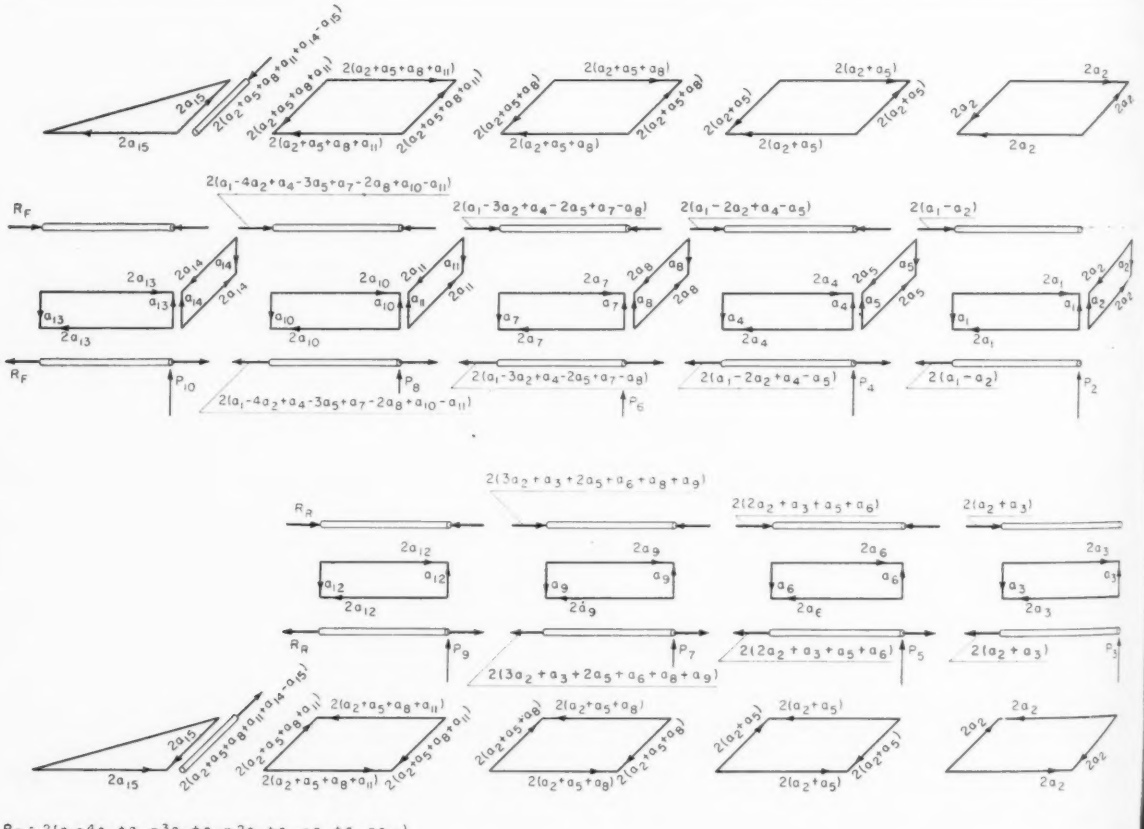

$R_F = 2(a_1 - 4a_2 + a_4 - 3a_5 + a_7 - 2a_8 + a_{10} - a_{11} + a_{13} - a_{15})$

$R_R = 2(4a_2 + a_3 + 3a_5 + a_6 + 2a_8 + a_9 + a_{11} + a_{12})$

FIG. 6. Sweptback wing broken down into structural units each in equilibrium.

(VII) Simplified Solution by the Method of Minimum Potential Energy

(a) *Application to a Swept Wing with Closely Spaced Rigid Ribs Perpendicular to the Spars*

The method described in Section (VI) suggests a somewhat more simplified approach to the problem. The outer section of the wing is assumed to be a box with closely spaced rigid ribs and joined to the inner part of the wing at Station 0 as shown by Fig. 14 instead of at Station 1 as shown by Fig. 12. The displacement of the juncture of the inner and outer section is assumed to be described by v_0 and α_0 and the displacements at a point x in the outer section by $v(x)$ and $\theta(x)$. With this arrangement, the continuity conditions are obviously not satisfied at Station 0; however, the essential features of the problem are preserved.

The following transformation is introduced,

$$\{v(x)\theta(x)\} = \begin{bmatrix} 1/2 & x/2 \\ 1/b & K(x) \end{bmatrix} \{v_0\alpha_0\} + \begin{bmatrix} 1 & 0 \\ 0 & 1 \end{bmatrix} \{\bar{v}(x)\bar{\theta}(x)\} \tag{46}$$

where $\bar{v}(x)$ and $\bar{\theta}(x)$ denote the deformations at a point x if it is assumed that the wing is rigidly clamped at Station 0. The factor $K(x)$ is given by Eq. (36).

The internal strain energy is written in two parts,

$$U_1 = (1/2)[v_0\alpha_0][K_1]\{v_0\alpha_0\} + \bar{U}_1[\bar{v}(x)\ \bar{\theta}(x)\ \bar{\varphi}(x)] \tag{47}$$

and the potential energy of the external loads is, accordingly,

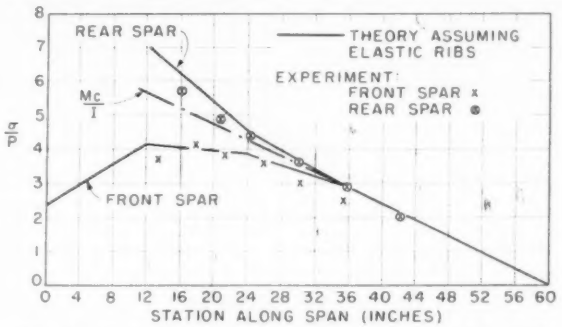

Fig. 7. Normal stresses in flanges of sweptback wing resulting from unit shear force at center of Section 2-3 (obtained by Levy method).

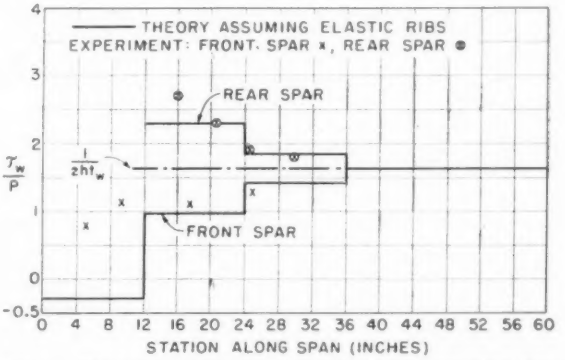

Fig. 8. Shear stresses in webs of sweptback wing resulting from unit shear force at center of Section 2-3 (obtained by Levy method).

$$U_e = -[PMT]\begin{bmatrix} (v_0/2) + \xi(\alpha_0/2) \\ \alpha_0/2 \\ (v_0/b) + K(\xi)\alpha_0 \end{bmatrix} - [PMT]\begin{bmatrix} v(\xi) \\ \bar{\alpha}(\xi) \\ \bar{\theta}(\xi) \end{bmatrix} \tag{48}$$

Applying the principle of minimum potential energy, two separate sets of equations are obtained,

$$[K_1]\{v_0\alpha_0\} = \begin{bmatrix} 1/2 & 0 & 1/b \\ \xi/2 & 1/2 & K(\zeta) \end{bmatrix}\{PMT\} \tag{49}$$

and the results given by Eqs. (40).

The deformations at any point x, due to loads at point ξ, are given by

$$\{v(x)\theta(x)\} = [[C_{ST}(x,\xi)] + [C_\Gamma(x,\xi)]]\{PMT\} \tag{50}$$

where $[C_{ST}(x,\xi)]$ is the matrix of influence functions assuming that the wing is unswept, and

$$[C_\Gamma(x,\xi)] = \begin{bmatrix} 1/2 & x/2 \\ 1/b & K(x) \end{bmatrix}[K_1]^{-1}\begin{bmatrix} 1/2 & 0 & 1/b \\ \xi/2 & 1/2 & K(\xi) \end{bmatrix} \tag{51}$$

are correction influence functions to be superimposed upon the unswept wing results to account for the effects of sweepback.

The stresses in the wing can also be regarded as a superposition of the stresses in an unswept wing plus correction terms accounting for the effects of sweep. Considering the important rear spar stresses, the normal stress in the rear flange at point x due to loads P, M, and T at point ξ is given by

$$\sigma_{RS}(x) = \sigma_{ST}(x) + \sigma_\Gamma(x) \tag{52}$$

where

$$\sigma_{ST}(x) = \left[\frac{\xi - x}{2Ah} \quad \frac{1}{2Ah} \quad \frac{\beta E}{8Ghb}\left(\frac{b}{t_c} - \frac{h}{t_w}\right)\left(\sinh \beta x - \frac{\cosh \beta x}{\cosh \beta \xi}\right)\right] \{PMT\} \tag{53}$$

is the normal stress distribution in the rear spar assuming the wing clamped at $x = 0$, and

$$\sigma_\Gamma(x) = (h\beta E/4)\ [(\cosh \beta x/\coth \beta \xi) - \sinh \beta x]\ [S_2]\ \{PMT\} \tag{54}$$

in which

$$[K_1]^{-1}\begin{bmatrix} 1/2 & 0 & 1/b \\ \xi/2 & 1/2 & K(\xi) \end{bmatrix} = \begin{bmatrix} [S_1]_{1\times 3} \\ [S_2]_{1\times 3} \end{bmatrix}$$

is the correction normal stress distribution for the effects of sweep.

The rear spar shear stress can be expressed in a similar manner,

$$\tau_{RS}(x) = \tau_{ST}(x) + \tau_\Gamma(x) \tag{55}$$

where

$$\tau_{ST}(x) = \left[-\frac{1}{2ht_w} \quad 0 \quad \frac{\beta^2 AE}{16Ghbt_w}\left(\frac{b}{t_c} - \frac{h}{t_w}\right)\left(\cosh \beta x - \frac{\sinh \beta x}{\coth \beta \xi}\right)\right] \{PMT\} \tag{56}$$

is the shear stress distribution in the rear spar assuming the wing clamped at $x = 0$, and

$$\tau_\Gamma(x) = \frac{h\beta^2 AE}{8t_w}\left(\frac{\sinh \beta x}{\coth \beta \xi} - \cosh \beta x\right)[S_2]_{1\times 3}\ \{PMT\} \tag{57}$$

is the correction shear stress distribution. The normal and shear distributions above have been computed on the assumption that the applied torque does not introduce normal stresses at the point of application.

If the torque and moment vectors are perpendicular and parallel, respectively, to the air stream, the following transformation may be introduced into all the previous equations developed for torque and moment vectors parallel and perpendicular, respectively, to the spars.

$$\{PMT\} = \begin{bmatrix} 1 & 0 & 0 \\ 0 & \cos \Gamma & \sin \Gamma \\ 0 & -\sin \Gamma & \cos \Gamma \end{bmatrix} \{P'M'T'\} \tag{58}$$

(b) *Comparison of Experiment and Theory*

As an illustration of the validity of the simplified theory, Figs. 15 and 16 compare theoretical and experimental deflections and spar normal stresses for a single shear load midway between the spars at the tip. The theoretical curves have been corrected for the effects of root deformation.

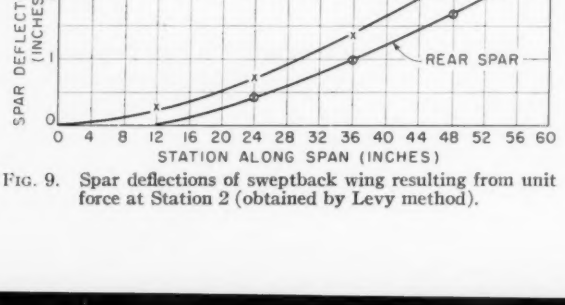

FIG. 9. Spar deflections of sweptback wing resulting from unit force at Station 2 (obtained by Levy method).

(VIII) CONCLUDING REMARKS

In the discussions above, theories based upon the assumption of ribs normal to the spars have been compared with experimental results from a wing with ribs parallel to the air stream. The influence of the rib direction does not seem to be important except for the possible presence of a root rib normal to the spars which closes the triangular section. In such cases, the rib is heavily loaded, and it should be included in the analysis if its design stresses are required. On the other hand, if ribs parallel to the air stream are used and if the most inboard rib is somewhat removed from the root, it can probably be assumed that the wing outboard of this rib behaves like a box with closely spaced rigid ribs normal to the spars.

As a final illustration of the effects of sweep on stresses and deflections, Figs. 17 and 18 have been prepared for a four-flange beam with double symmetry. Fig. 17 illustrates the variation with sweep of the ratio of rear spar normal and shear stress at the root of the

swept wing to the corresponding stresses in the straight wing for a single shear force applied remote from the root and midway between the spars. Fig. 18 illustrates similar ratios for tip deformations—namely, tip deflection due to a concentrated shear force at the tip midchord and tip twist due to a concentrated torque at the wing tip. The curves of Figs. 17 and 18 are based on the simplified theory described in Section (VII), and the ratios are developed in Appendix (B).

It is important to emphasize some simplifying assumptions employed in the present paper. The problem of shear lag in the cover skin and the effects of buckling have been neglected. In order to include shear lag effects, it is necessary to analyze a cross section that more closely approximates the true structure than the simplified four-flange box beam. To include shear lag greatly complicates the analysis, and a discussion of this procedure is presented in reference 7. The effect of shear lag is a reduction of structural efficiency resulting in increased deflections and increased stresses in the corner flanges. Skin and stringer buckling introduce nonlinearity into the problem and are usually accounted for by approximations. The inclusion of shear lag and buckling effects in the swept-wing problem must be a subject for further research.

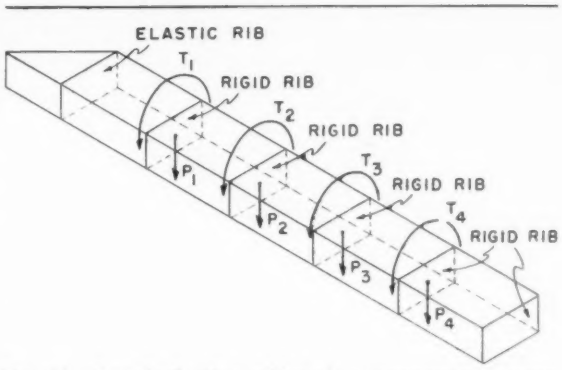

FIG. 10. Sweptback wing subjected to concentrated torques and vertical loads.

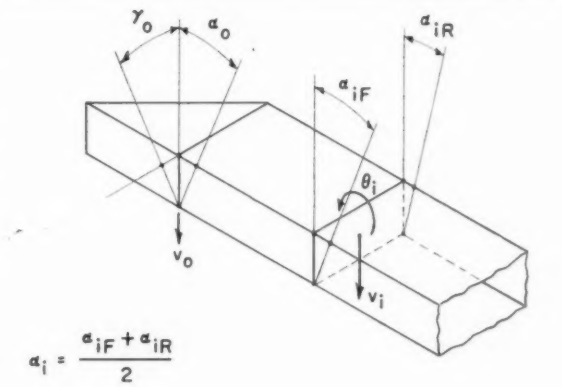

$$\alpha_i = \frac{\alpha_{iF} + \alpha_{iR}}{2}$$

$$\phi_i = \alpha_{iF} - \alpha_{iR}$$

FIG. 11. Displacement notations.

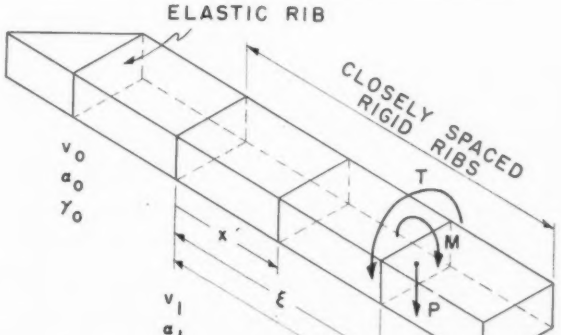

FIG. 12. Sweptback wing with closely spaced rigid ribs outboard of Station 1.

REFERENCES

[1] Levy, S., *Computation of Influence Coefficients for Aircraft Structures with Discontinuities*, Journal of the Aeronautical Sciences, Vol. 14, No. 10, p. 547, October, 1947.

[2] Wittrick, W. H., *Preliminary Analysis of a Highly Swept Cylindrical Tube Under Torsion and Bending*, Aeronautical Research Report ACA-39, Commonwealth of Australia, 1948.

[3] Thompson, J. J., and Wittrick, W. H., *The Stresses in Certain Cylindrical Swept Tubes Under Torsion and Bending*, Aeronautical Research Report ACA-43. Commonwealth of Australia, January, 1949.

[4] Goodman, Stanley, *Root Stress Distribution in Sweptback Sheet*, National Bureau of Standards Report, September 20, 1950.

[5] Zender, George, and Libove, Charles, *Stress and Distortion Measurements in a 45° Swept Box Beam Subjected to Bending and to Torsion*, N.A.C.A. T.N. No. 1525, March, 1948.

[6] Zender, George, and Heldenfels, Richard, *Stress and Distortion Measurements in a 45° Swept Box Beam Subjected to Antisymmetrical Bending and Torsion*, N.A.C.A. T.N. No. 2054, April, 1950.

[7] Heldenfels, Richard R., Zender, George W., and Libove, Charles, *Stress and Distortion Analysis of a Swept Box Beam Having Bulkheads Perpendicular to the Spars*, N.A.C.A. T.N. No. 2232, November, 1950.

[8] Bisplinghoff, R. L., and Lang, Arthur, *An Investigation of Deformations and Stresses in Sweptback and Tapered Wings with Discontinuities*, M.I.T. Aero-Elastic and Structures Research Report, July 1, 1949.

[9] Kuhn, Paul, *Deformation Analysis of Wing Structures*, N.A.C.A. T.N. No. 1361, July, 1947.

[10] Kuhn, Paul, *A Method of Calculating Bending Stresses Due to Torsion*, N.A.C.A. Wartime Report, L-352, December, 1942.

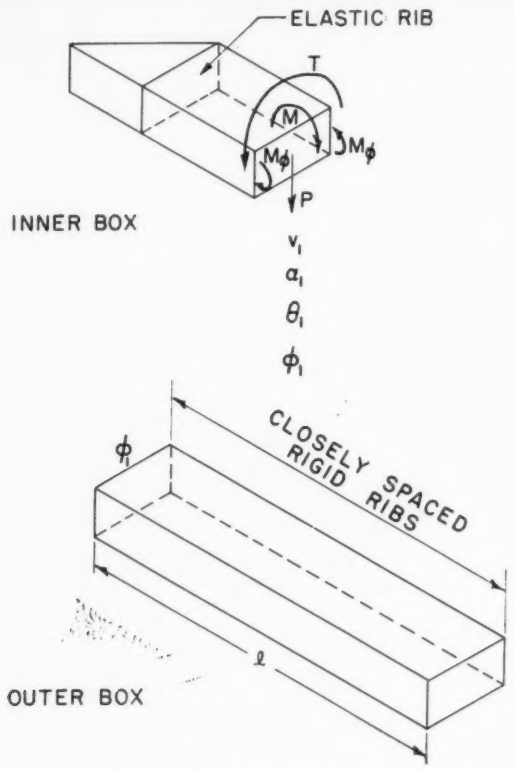

FIG. 13. Structural division of sweptback wing for determination of energy matrix $[K_1]$ in Appendix (A).

APPENDIX (A)

Development of Energy Matrix $[K_1]$

The energy matrix $[K_1]$ of Eq. (37) may be determined by the following procedure. The wing structure of Fig. 12 is divided into two parts as shown in Fig. 13. Here, the inner box is completely elastic with finite rib spacing, whereas the outer box is assumed to be elastic in warping only. The inner box is subjected to the indicated loads, and by applying the Levy method of Section (V), the internal strain energy is written as

$$U_i = (1/2)[PMTM_\varphi][C]\{PMTM_\varphi\} \qquad (A1)$$

The matrix $[C]$ may then be inverted to express the inner box strain energy in terms of displacements as

$$U_i = (1/2)[v_1\alpha_1\theta_1\varphi_1][C]^{-1}\{v_1\alpha_1\theta_1\varphi_1\} \qquad (A2)$$

Using the results of reference 10, the strain energy in the outer box due to warping φ_1 at the inboard end is written as

$$U_i = (1/2)[(h^2\beta AE)/4 \coth \beta l]\varphi_1^2 \qquad (A3)$$

The total strain energy in the inner and outer boxes is the sum of Eqs. (A2) and (A3), which yields

$$U_i = 1/2[v_1\alpha_1\theta_1\varphi_1][K_1]\{v_1\alpha_1\theta_1\varphi_1\} \qquad (A4)$$

where

$$[K_1] = [C]^{-1} + [K']$$

$$[K'] = \begin{bmatrix} 0 & 0 & 0 & 0 \\ 0 & 0 & 0 & 0 \\ 0 & 0 & 0 & 0 \\ 0 & 0 & 0 & \dfrac{h^2\beta AE}{4 \coth \beta l} \end{bmatrix}$$

APPENDIX (B)

Stress and Deflection Variation with Sweep

In general, the important design stresses of the swept-wing problem are the normal and shear stresses at the root of the rear spar. For the test specimen of Section (II), these stresses have been plotted versus sweepback angle in Fig. 17 as the ratio of swept-wing stress to corresponding straight-wing stress. The curves are based on the simplified theory of Section (VII), and are obtained as follows.

From Eqs. (53) and (54) we obtain

$$\frac{\sigma_{ST}(0) + \sigma_\Gamma(0)}{\sigma_{ST}(0)} = 1 + \frac{\beta}{2\xi}\left(\frac{2\xi + b\tan\Gamma}{[2/b\tan\Gamma)] + \beta}\right) \qquad (B1)$$

and from Eqs. (56) and (57),

$$\frac{\tau_{ST}(0) + \tau_\Gamma(0)}{\tau_{ST}(0)} = 1 + \frac{\beta^2}{4}\left(\frac{2\xi + b\tan\Gamma}{[2/(b\tan\Gamma)] + \beta}\right) \qquad (B2)$$

By introducing into Eqs. (B1) and (B2) appropriate values for the parameters β, ξ, and b, the curves of Fig. 17 may be duplicated for other four-flange, doubly symmetrical cross sections.

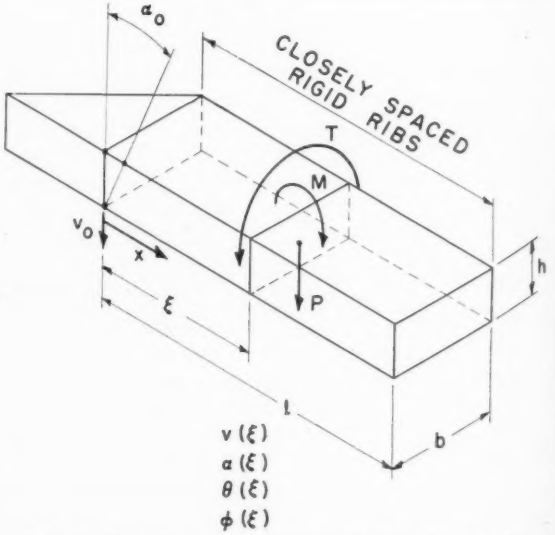

FIG. 14. Sweptback wing with closely spaced rigid ribs outboard of Station 0.

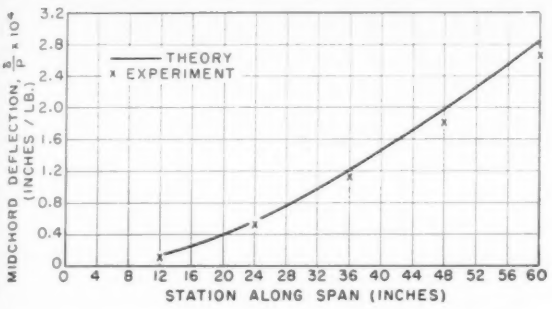

FIG. 15. Mid-chord deflection of sweptback wing resulting from unit shear force at center of Section 2-3 [obtained by the simplified method of Section (VII)].

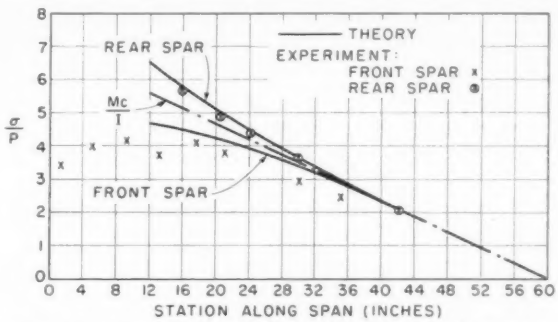

FIG. 16. Normal stresses in flanges of sweptback wing resulting from unit shear force at center of Section 2-3 [obtained by simplified method of Section (VII)].

The deflection curves of Fig. 18 are the result of a more complicated derivation. The deflection ratios may be obtained as follows.

From Eqs. (40) and (51), respectively,

$$C_{ST}{}^{vP}(\xi, \xi) = (l^3/3AEh^2) + (l/2ht_wG) \qquad \text{(B3)}$$

$$C_\Gamma{}^{vP}(\xi, \xi) = \frac{\frac{1}{4}\left(K_{M\alpha} + \frac{h^2\beta AE}{4 \coth \beta l} - 2\xi K_{P\alpha} + \xi^2 K_{Pr}\right)}{K_{Pr}\left(K_{M\alpha} + \frac{h^2\beta AE}{4 \coth \beta l}\right) - K_{P\alpha}{}^2} \qquad \text{(B4)}$$

where, from Eq. (47),

$$[K_1] \equiv \begin{bmatrix} K_{P_t} & K_{P\alpha} \\ K_{Mt} & \left(K_{M\alpha} + \frac{h^2\beta AE}{4 \coth \beta l}\right) \end{bmatrix}$$

For a concentrated shear load midway between the spars at the wing tip ($x = \xi$), the ratio of swept-wing tip deflection to the corresponding deflection of a straight wing is

$$[C_{ST}{}^{vP}(\xi, \xi) + C_\Gamma{}^{vP}(\xi, \xi)]/C_{ST}{}^{vP}(\xi, \xi) \qquad \text{(B5)}$$

Similarly, from Eqs. (40) and (51), respectively,

$$C_{ST}{}^{\theta T}(\xi, \xi) = (l/GJ)\,[1 - (\eta^2/\beta l)] \qquad \text{(B6)}$$

$$C_\Gamma{}^{\theta T}(\xi, \xi) = \frac{\frac{1}{b^2}\left(K_{M\alpha} + \frac{h^2\beta AE}{4 \coth \beta l}\right) - \frac{2}{b}K(\xi)K_{P\alpha} + K^2(\xi)K_{Pr}}{K_{Pr}\left(K_{M\alpha} + \frac{h^2\beta AE}{4 \coth \beta l}\right) - K^2{}_{P\alpha}} \qquad \text{(B7)}$$

where

$$\eta = [(b/t_c) - (h/t_w)]/[(b/t_c) + (h/t_w)]$$
$$J = 2b^2h^2/[(b/t_c) + (h/t_w)]$$

$K(\xi)$ is defined by Eq. (36).

For a concentrated torque at the tip, the ratio of swept-wing tip twist to the corresponding twist of a straight wing is

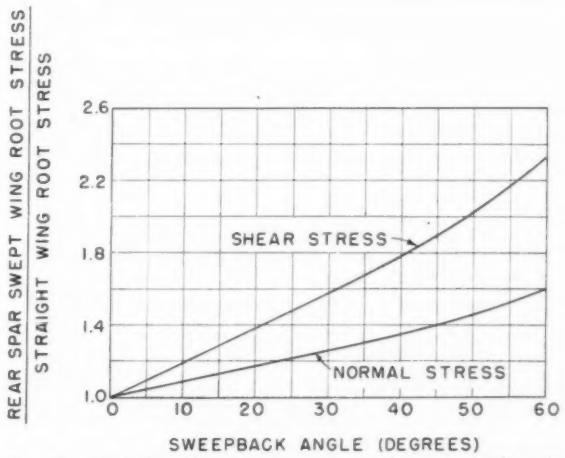

FIG. 17. Variation of rear spar root stress with sweepback angle for a shear force at the center of Section 2-3.

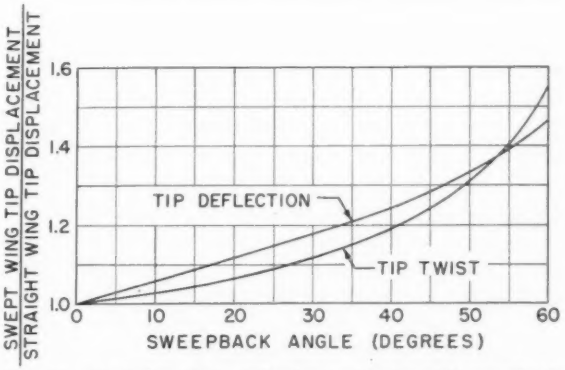

FIG. 18. Variation of tip deflection and twist with sweepback angle for a shear force and torque, respectively, at Section 2-3.

$$[C_{ST}{}^{\theta T}(\xi, \xi) + C_\Gamma{}^{\theta T}(\xi, \xi)]/C_{ST}{}^{\theta T}(\xi, \xi) \qquad \text{(B8)}$$

The ratios (B7) and (B8) are plotted versus sweep angle in Fig. 18 for the experimental wing of Section (II). Similar curves may be developed for other four-flange, doubly symmetrical cross sections by introducing appropriate parameters into the equations.

Gyro Pickoff Indications at Arbitrary Plane Attitudes

LEONARD BECKER*

Lear, Incorporated

SUMMARY

The error sensing device most often used in present-day aircraft having autopilot control—free or displacement gyros—generally gives pickoff indications at arbitrary plane attitudes for small deviations from these attitudes, which are functions not only of the departures about the axes that these pickoffs are supposed to detect, but also the departures about the other two axes. These functional relationships are calculated for a common arrangement of vertical and directional gyros for an arbitrary attitude of the plane and various special attitudes which might occur in maneuvers. In the general case, the resolution of the pickoff signals to feed correctly the autopilot servos for stabilization purposes is indicated. Gyro interactions which would impair stabilization are shown to exist.

INTRODUCTION

THE USE OF DISPLACEMENT or free gyros as attitude-error sensing devices for autopilot control of aircraft is well known. These gyros give accurate indications for small deviations from level flight. However, in the case where the autopilot is used for stabilization while extended maneuvers are taking place, the gyro error signals will generally not be accurate indications of departures of the plane about its own axes, since these inaccuracies arise as a geometrical consequence of the inertial properties of the gyro spin axes, and the arrangements of pickoffs and gimbals. The importance of obtaining correct indications of the plane's perturbations about its axes, however they may happen to be oriented in space, is due to the fact that control moments, used to stabilize the plane, are always applied about the airplane axes. Furthermore, as stability criteria demand that the applied control moments be certain functions of the perturbations about the mean orientations of the airplane axes, it becomes necessary to interpret the apparent perturbations about the space axes, represented by the gyros, in terms of the true perturbations, about the plane's axes, in order that the correct control moments may be applied. It is the purpose of this paper to calculate the consequences of large plane departures from level flight on the pickoff readings of a set of commonly arranged vertical and directional position gyros.

PICKOFF AND DIRECTION COSINE RELATIONSHIPS

Vertical and directional displacement gyros are usually free gyros with two gimbal rings which permit the gyro spin axis to remain fixed in direction while the gyro case, integral with the airplane, rotates in an arbitrary fashion within certain limits.

Schematically the vertical gyro may be represented as shown in Fig. 1.

The arrangement of the directional gyro is similar to that of the vertical unit, except that its spin axis is horizontal.

The gyros are assumed to be mounted so that, initially, the orientation of the inertial, airplane, gimbal, and spin axes is as shown in Fig. 2.

The axes may be defined as follows:

X, Y, Z are inertial axes

x_a, y_a, z_a are the airplane symmetry axes through the c.g.

A_{sv}, A_{sd} are spin axes of vertical and directional gyros

A_{ogv}, A_{igv} are outer and inner gimbal axes of vertical gyro

A_{ogd}, A_{igd} are outer and inner gimbal axes of directional gyro

The axis, A_{sd}, can be made to coincide initially with Y and Y_a, since there will always be a heading at which the pickoff signals will be zero. Any deviation from this heading will evidence itself in pickoff signals. This convention, while greatly simplifying the analysis, in no way decreases its generality.

ANALYSIS

If the airplane departs from its initial position, the orientation of the gimbal axes relative to the other axes will change. From properties and constraints of the gyro assemblies, the ensuing gimbal axes' orientation and pickoff angles may readily be ascertained by noting the following relations:

A.—Due to structural constraints

(1) A_{ogv} remains coincident with x_a

(2) A_{ogd} remains coincident with z_a

(3) A_{igv} always remains $\perp$ to A_{sv} and x_a

(4) A_{igd} always remains $\perp$ to A_{sd} and z_a

B.—Due to the geometry of the gimbals

(1) p_1 = outer pickoff v.g. (roll) = $\sphericalangle$ between y_a, A_{igv}

(2) p_2 = inner pickoff v.g. (pitch) = $\sphericalangle$ between A_{sv} and line which is mutually $\perp$ to A_{ogv}, A_{igv}

(3) p_3 = outer pickoff d.g. (yaw) = $\sphericalangle$ between A_{igd}, y_a

Received December 11, 1950.

* Project Engineer, LearCal Division.

(4) From initial orientation of the axes, it is then seen that the initial reading of p_1 is 0; p_2 is 0; p_3 is 90°

Suppose that the airplane has assumed some large, arbitrary attitude. The relation between the airplane axes and the inertial axes may then be expressed by the transformation matrix:

$$[L] = \begin{array}{c|ccc} & x_a & y_a & z_a \\ X & l_1 & l_4 & l_7 \\ Y & l_2 & l_5 & l_8 \\ Z & l_3 & l_6 & l_9 \end{array}$$

where the l's represent the direction cosines.

The new orientation of the axes, as defined by the transformation matrix $[L]$, can then be represented by the system shown in Fig. 3.

From the properties of the gyro assemblies, it can be deduced that: (a) X, Y, A_{igr} are coplanar (due to inertial rigidity); (b) x_a, y_a, A_{igd} are coplanar (due to structural constraint); (c) $A_{igd} \perp$ to plane formed by A_{sd} and z_a; (d) $A_{igr} \perp$ to plane formed by A_{sr} and x_a.

The pickoff angles p_1, p_2, p_3, which are the only available data defining the position of the plane in space, can be shown to have the following values in terms of the direction cosines:

$$\left.\begin{aligned} \tan p_1 &= l_6/l_9 \\ -\sin p_2 &= l_3 \\ \cot p_3 &= l_2/l_5 \end{aligned}\right\} \qquad (1)$$

Conversely:

$$l_1 = [\cos p_2\,(Q^2 - \cos^2 p_1)^{1/2}]/Q$$

where

$$\left.\begin{aligned} Q &= (1/\cos p_3)\left\{(\cos p_2 \sin p_3 \sin p_1 - \cos p_3 \sin p_2)^2 + \cos^2 p_1 \cos^2 p_2\right\}^{1/2} \\ l_2 &= (\cos p_1 \cos p_2)/Q \\ l_3 &= -\sin p_2 \\ l_4 &= \left\{(\sin p_2 - \sin p_1 \cos p_2 \tan p_3)^2 + \cos^2 p_2(\cos^2 p_1 - \sin^2 p_1 Q^2)\right\}^{1/2}/Q \\ l_5 &= (\cos p_1 \cos p_2 \tan p_3)/Q \\ l_6 &= \sin p_1 \cos p_2 \\ l_7 &= [\cos p_1 \cos p_2\,(\tan^2 p_3 - Q^2)^{1/2}]/Q \\ l_8 &= (\sin p_2 - \sin p_1 \cos p_2 \tan p_3)/Q \\ l_9 &= \cos p_1 \cos p_2 \end{aligned}\right\} \qquad (2)$$

In determining these expressions, the relations

$$l_1^2 + l_2^2 + l_3^2 = 1$$

etc., were used, as well as the orthogonality relations, such as

$$l_1 l_4 + l_2 l_5 + l_3 l_6 = 0$$

Calculation of Proper Signals To Be Inserted into Stabilization System

Suppose now that the airplane suffers small yaw, roll, and pitch deviations, ψ, ϕ, θ, respectively, from its new attitude. In order to stabilize the plane about its new attitude, and since the control moments are applied about the airplane axes, it is necessary to compute Δp_1, Δp_2, Δp_3 for these small deviations and determine how to insert the appropriate error signals into the control systems. The steady signals arising from the angles p_1, p_2, p_3 are assumed to be cancelled out by appropriate means. To accomplish this computation, the following procedure might be used:

For a small rotation, ψ, about z_a, the rotation matrix is

Case

$$[\psi] = \begin{array}{c|ccc} & x_a' & y_a' & z_a \\ x_a & \cos\psi & \sin\psi & 0 \\ y_a & -\sin\psi & \cos\psi & 0 \\ z_a & 0 & 0 & 1 \end{array}$$

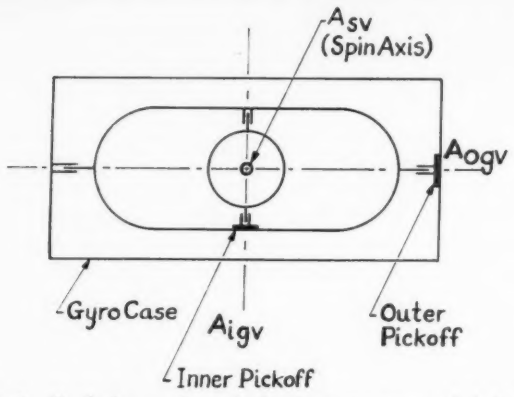

FIG. 1. Vertical gyro schematic showing arrangement of gimbals and pickoffs.

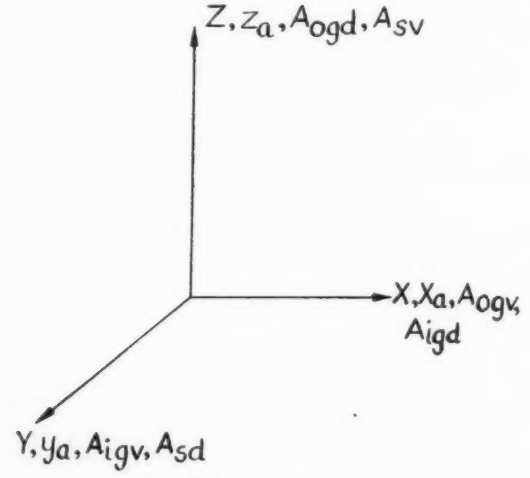

FIG. 2. Initial orientation of axes.

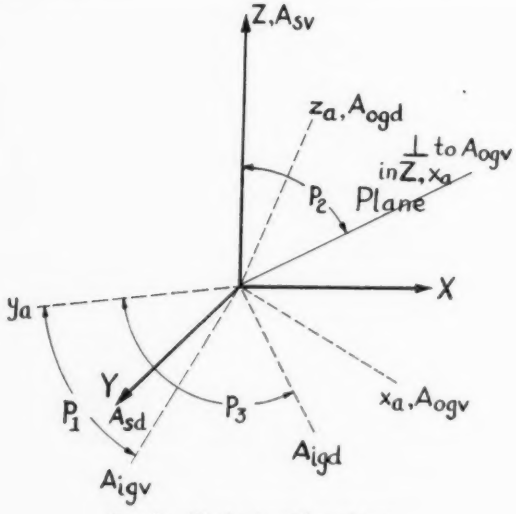

FIG. 3. Final orientation of axes.

where x_a' and y_a' are the perturbed positions of x_a, y_a.

The relation between x_a', y_a', z_a and X, Y, Z may be found from the matrix multiplication, $[\psi] \times [L]$, the result of which is

$$[\psi] \times [L] = \begin{array}{c|cc|c} & x_a' & y_a' & z_a \\ \hline X & \begin{matrix} l_1 \cos\psi \\ -l_4 \sin\psi \end{matrix} & \begin{matrix} +l_1 \sin\psi \\ +l_4 \cos\psi \end{matrix} & l_7 \\ Y & \begin{matrix} l_2 \cos\psi \\ -l_5 \sin\psi \end{matrix} & \begin{matrix} +l_2 \sin\psi \\ +l_5 \cos\psi \end{matrix} & l_8 \\ Z & \begin{matrix} l_3 \cos\psi \\ -l_6 \sin\psi \end{matrix} & \begin{matrix} +l_3 \sin\psi \\ +l_6 \cos\psi \end{matrix} & l_9 \end{array}$$

Similarly, for a rotation, ϕ, about x_a

Case II

$$[\Phi] = \begin{array}{c|ccc} & x_a & y_a'' & z_a'' \\ \hline x_a & 1 & 0 & 0 \\ y_a & 0 & \cos\phi & \sin\phi \\ z_a & 0 & -\sin\phi & \cos\phi \end{array}$$

and by the matrix multiplication, $[\Phi] \times [L]$,

$$[\Phi] \times [L] = \begin{array}{c|cc|c} & x_a & y_a'' & z_a'' \\ \hline X & l_1 & \begin{matrix} l_4 \cos\phi \\ -l_7 \sin\phi \end{matrix} & \begin{matrix} l_4 \sin\phi \\ +l_7 \cos\phi \end{matrix} \\ Y & l_2 & \begin{matrix} l_5 \cos\phi \\ -l_8 \sin\phi \end{matrix} & \begin{matrix} l_5 \sin\phi \\ +l_8 \cos\phi \end{matrix} \\ Z & l_3 & \begin{matrix} -l_9 \sin\phi \\ +l_6 \cos\phi \end{matrix} & \begin{matrix} l_6 \sin\phi \\ +l_9 \cos\phi \end{matrix} \end{array}$$

and for a rotation, θ, about y_a,

Case III

$$[\theta] = \begin{array}{c|ccc} & x_a''' & y_a & z_a''' \\ \hline x_a & \cos\theta & 0 & \sin\theta \\ y_a & 0 & 1 & 0 \\ z_a & -\sin\theta & 0 & \cos\theta \end{array}$$

and by the matrix multiplication, $[\theta] \times [L]$,

$$[\theta] \times [L] = \begin{array}{c|cc|c} & x_a''' & y_a & z_a''' \\ \hline X & \begin{matrix} +l_1 \cos\theta \\ -l_7 \sin\theta \end{matrix} & l_4 & \begin{matrix} +l_7 \cos\theta \\ +l_1 \sin\theta \end{matrix} \\ Y & \begin{matrix} +l_2 \cos\theta \\ -l_8 \sin\theta \end{matrix} & l_5 & \begin{matrix} +l_2 \sin\theta \\ +l_8 \cos\theta \end{matrix} \\ Z & \begin{matrix} -l_9 \sin\theta \\ +l_3 \cos\theta \end{matrix} & l_6 & \begin{matrix} +l_3 \sin\theta \\ +l_9 \cos\theta \end{matrix} \end{array}$$

Since only small rotations were made in each case from the arbitrary attitude denoted by $[L]$, the new

direction cosines detailing the perturbed attitude may be denoted as $l_1 + \Delta l_1$, etc. Comparing these perturbed direction cosines with corresponding elements of $[\psi] \times [L]$, and also noting that for small enough ψ, $\cos \psi \approx 1$, $\sin \psi \approx \psi$, the following expressions are obtained:

$$
\left.\begin{array}{lll}
\textit{Case I} & & \\
\Delta l_1 = -l_4\psi & \Delta l_4 = l_1\psi & \Delta l_7 = 0 \\
\Delta l_2 = -l_5\psi & \Delta l_5 = l_2\psi & \Delta l_8 = 0 \\
\Delta l_3 = -l_6\psi & \Delta l_6 = l_3\psi & \Delta l_9 = 0 \\
\text{Similarly} & & \\
\textit{Case II} & & \\
\Delta l_1 = 0 & \Delta l_4 = -l_7\phi & \Delta l_7 = l_4\phi \\
\Delta l_2 = 0 & \Delta l_5 = -l_8\phi & \Delta l_8 = l_5\phi \\
\Delta l_3 = 0 & \Delta l_6 = -l_9\phi & \Delta l_9 = l_6\phi \\
\textit{Case III} & & \\
\Delta l_1 = -l_7\theta & \Delta l_4 = 0 & \Delta l_7 = l_1\theta \\
\Delta l_2 = -l_8\theta & \Delta l_5 = 0 & \Delta l_8 = l_2\theta \\
\Delta l_3 = -l_9\theta & \Delta l_6 = 0 & \Delta l_9 = l_3\theta
\end{array}\right\} \quad (3)
$$

The quantities Δp_1, Δp_2, Δp_3 may be found by differentiating Eq. 1.

Then

$$
\left.\begin{array}{l}
\Delta p_1 = (\cos^2 p_1/l_9^2)(l_9\Delta l_6 - l_6\Delta l_9) \\
\Delta p_2 = -\Delta l_3/\cos p_2 \\
\Delta p_3 = (\sin^2 p_3/l_5^2)(l_2\Delta l_5 - l_5\Delta l_2)
\end{array}\right\} \quad (4)
$$

In order to express the Δp_1, Δp_2, Δp_3 in terms of the airplane's angular deviations θ, ϕ, and ψ from the arbitrary attitude, Eqs. (2) and (3) are used to evaluate (4). The results are:

$$
\textit{Case I} \quad \left.\begin{array}{l}
\Delta p_1 = (-\sin p_2 \cos p_1)\psi/\cos p_2 \\
\Delta p_2 = \sin p_1\psi \\
\Delta p_3 = \psi
\end{array}\right\} \quad (5)
$$

$$
\textit{Case II} \quad \left.\begin{array}{l}
\Delta p_1 = -\phi \\
\Delta p_2 = 0 \\
\Delta p_3 = \\
\dfrac{-\cos p_3(\sin p_2 \cos p_3 - \sin p_1 \cos p_2 \sin p_3)\phi}{\cos p_1 \cos p_2}
\end{array}\right\} \quad (6)
$$

$$
\textit{Case III} \quad \left.\begin{array}{l}
\Delta p_1 = (\sin p_2 \sin p_1)\theta/\cos p_2 \\
\Delta p_2 = (\cos p_1)\,\theta \\
\Delta p_3 = \\
\dfrac{\sin p_3(\sin p_2 \cos p_3 - \sin p_1 \cos p_2 \sin p_3)\,\theta}{\cos p_1 \cos p_2}
\end{array}\right\} \quad (7)
$$

Since the rotations are small, the results of the three rotations may be added, with the resultant signals, Δp_1, Δp_2, Δp_3 expressible as

$$
\left.\begin{array}{l}
\Delta p_1 = a_1\psi + b_1\phi + c_1\theta \\
\Delta p_2 = a_2\psi + b_2\phi + c_2\theta \\
\Delta p_3 = a_3\psi + b_3\phi + c_3\theta
\end{array}\right\} \quad (8)
$$

where the coefficients are given in Eqs. (5), (6), and (7).

Solving for ψ, ϕ, θ:

$$
\psi = \frac{\begin{vmatrix} \Delta p_1 & b_1 & c_1 \\ \Delta p_2 & b_2 & c_2 \\ \Delta p_3 & b_3 & c_3 \end{vmatrix}}{D}
$$

where

$$
D = \begin{vmatrix} a_1 & b_1 & c_1 \\ a_2 & b_2 & c_2 \\ a_3 & b_3 & c_3 \end{vmatrix}
$$

$$
\phi = \frac{\begin{vmatrix} a_1 & \Delta p_1 & c_1 \\ a_2 & \Delta p_2 & c_2 \\ a_3 & \Delta p_3 & c_3 \end{vmatrix}}{D}
$$

$$
\theta = \frac{\begin{vmatrix} a_1 & b_1 & \Delta p_1 \\ a_2 & b_2 & \Delta p_2 \\ a_3 & b_3 & \Delta p_3 \end{vmatrix}}{D}
$$

Generally, the solutions will be of the form

$$
\left.\begin{array}{l}
\psi = d_1\,\Delta p_1 + d_2\,\Delta p_2 + d_3\,\Delta p_3 \\
\phi = e_1\,\Delta p_1 + e_2\,\Delta p_2 + e_3\,\Delta p_3 \\
\theta = f_1\,\Delta p_1 + f_2\,\Delta p_2 + f_3\,\Delta p_3
\end{array}\right\} \quad (9)
$$

and an appropriate computer will solve for the ψ, ϕ, and θ error signals from the intelligence Δp_1, Δp_2, Δp_3.

In the event that the pickoff readings are in the form of voltages, which are sinusoidal functions of the angular departures, p_1, p_2, p_3, Eq. (9) may be corrected by the following procedure:

Let v_1 be the reading of the p_1 pickoff, for instance, so that

$$
v_1 = V_1 \sin p_1 \ (V_1 \text{ being a constant})
$$

and for small departures, Δp_1, there is obtained the expression

$$
\Delta p_1 = \Delta v_1/(V_1 \cos p_1)
$$

and similarly for Δp_2, Δp_3.

Substituting these expressions in Eqs. (5), (6), and (7) and in a similar manner as above solving for ψ, ϕ, and θ, the solutions would be in the form

$$
\left.\begin{array}{l}
\psi = d_1'\Delta v_1 + d_2'\Delta v_2 + d_3'\Delta v_3 \\
\phi = e_1'\Delta v_1 + e_2'\Delta v_2 + e_3'\Delta v_3 \\
\theta = f_1'\Delta v_1 + f_2'\Delta v_2 + f_3'\Delta v_3
\end{array}\right\} \quad (9a)
$$

and again an appropriate computer will solve for the ψ, ϕ, and θ error signals from the Δv_1, Δv_2, Δv_3 readings.

Turning About a Vertical Axis

Let it be assumed that with the plane in the arbitrary attitude denoted by $[L]$ it is desired to make a change in heading by turning about a vertical axis. If the turn is through an angle λ so that x_a, y_a, z_a goes to x_a', y_a', z_a', the resulting set of direction cosines is

	x_a'	y_a'	z_a'
X	$l_1 \cos\lambda + l_2 \sin\lambda$	$l_4 \cos\lambda - l_5 \sin\lambda$	$l_7 \cos\lambda - l_8 \sin\lambda$
Y	$l_2 \cos\lambda - l_1 \sin\lambda$	$l_5 \cos\lambda + l_4 \sin\lambda$	$-l_8 \cos\lambda - l_7 \sin\lambda$
Z	l_3	l_6	l_9

and from Eq. (1), the new pickoff readings, p_1', p_2', p_3' are given by the relations below:

$$\begin{aligned}\tan p_1' &= l_6/l_9\\ \sin p_2' &= -l_3\\ \cot p_3' &= (l_2\cos\lambda - l_1\sin\lambda)/(l_5\cos\lambda + l_4\sin\lambda)\\ &= \cot(p_3 + \Delta p_3)\\ &= (\cot p_3 \cot\Delta p_3 - 1)/(\cot p_3 + \cot\Delta p_3)\end{aligned}$$

It will be noted by comparing the above with Eq. (1) that turning about a vertical axis, after the plane assumes some arbitrary attitude, does not change the p_1 or p_2 pickoff readings. The heading angle, H, may be computed from the pickoff readings, thus:

$$\tan H = \frac{-l_2}{l_1} = \frac{-\cos p_1 \cos p_3}{\{(\cos p_2 \sin p_3 \sin p_1 - \cos p_3 \sin p_2)^2 + \cos^2 p_1 (\cos^2 p_2 - \cos^2 p_3)\}^{1/2}}$$

Some Special Attitudes

The result of perturbations from some special attitudes into which a plane might be maneuvered will now be considered.

(A) *Coordinated Turn (Pitch Attitude Change Negligible)*

If initially the plane is flying straight and level and the new attitude is obtained by first rotating the plane into a bank of angle ϕ_b, the rotation matrix is

$[\phi_b] =$	x_a	y_a	z_a
X	1	0	0
Y	0	$\cos\phi_b$	$\sin\phi_b$
Z	0	$-\sin\phi_b$	$\cos\phi_b$

and then a turn λ about a vertical axis, the rotation matrix becomes

$[\lambda] \times [\phi] =$	x_a'	y_a'	z_a'
X	$\cos\lambda$	$-\cos\phi_b \sin\lambda$	$-\sin\phi_b \sin\lambda$
Y	$-\sin\lambda$	$\cos\phi_b \cos\lambda$	$-\sin\phi_b \cos\lambda$
Z	0	$-\sin\phi_b$	$\cos\phi_b$

so that the direction cosines become

$$\begin{aligned} l_1 &= \cos\lambda & l_4 &= -\cos\phi_b \sin\lambda & l_7 &= -\sin\phi_b \sin\lambda\\ l_2 &= -\sin\lambda & l_5 &= \cos\phi_b \cos\lambda & l_8 &= -\sin\phi_b \cos\lambda\\ l_3 &= 0 & l_6 &= -\sin\phi_b & l_9 &= \cos\phi_b\end{aligned}$$

From Eq. (1)

$$\begin{aligned}\tan p_1 &= l_6/l_9 = -\tan\phi_b;\ p_1 = -\phi_b\\ -\sin p_2 &= l_3 = 0;\ p_2 = 0\\ \tan p_3 &= l_5/l_2 = -\cos\phi_b/\tan\lambda\end{aligned}$$

Then, applying Eqs. (5), (6), and (7), one obtains

Case I

(small yaw)

$$\begin{aligned}\Delta p_1 &= 0\\ \Delta p_2 &= -\sin\phi_b \cdot \psi\\ \Delta p_3 &= \psi\end{aligned} \qquad (10)$$

Case II

(small roll)

$$\begin{aligned} \Delta p_1 &= -\phi \\ \Delta p_2 &= 0 \\ \Delta p_3 &= [(-\sin \phi_b \tan \lambda)/(\cos^2 \phi_b + \tan^2 \lambda)]\phi \end{aligned} \tag{11}$$

Case III

(small pitch)

$$\begin{aligned} \Delta p_1 &= 0 \\ \Delta p_2 &= \cos \phi_b \cdot \theta \\ \Delta p_3 &= [(-\sin \phi_b \cos \phi_b)/(\cos^2 \phi_b + \tan^2 \lambda)]\theta \end{aligned} \tag{12}$$

Eqs. (10), (11), and (12) show that if Δp_1, Δp_2, and Δp_3 are the error signals actuating the control surfaces (no computer as given by Eq. (9) is used), no interactions will exist between pitch and roll or yaw and roll, but that pitch to yaw to pitch interactions will exist at headings other than $\lambda = 90°$ or $270°$. At $\lambda = 0°$ or $180°$ maximum interactions occur where

$$\Delta p_3 = -\tan \phi_b \cdot \theta \tag{13}$$

Thus, as may be seen from Eq. (12), a small pitch disturbance, θ, will actuate both elevator and rudder. Rudder motion in turn will give rise to a ψ disturbance which will again cause the elevator to act (Eq. (10)), giving rise to a possible instability. This kind of interaction cannot involve the roll channel because of the $\Delta p_1 = 0$ expressions in Eqs. (10) and (12). A roll departure will give a rudder signal from Eq. (11), causing a ψ disturbance, but this ψ disturbance cannot in turn cause an aileron motion.

Eq. (13) shows that the effect of θ on Δp_3 can be extremely large at high bank angles. Finally, Eq. (12) shows that the pitch gyro sensitivity, insofar as the pitch control signal is concerned, is decreased by the factor, $\cos \phi_b$

(B) *Climbing Turn*

If the new attitude is obtained by first making a pitch rotation, θ_p, the rotation matrix is

$[\theta_p]$

	x_a'	y_a	z_a'
X	$\cos \theta_p$	0	$\sin \theta_p$
Y	0	1	0
Z	$-\sin \theta_p$	0	$\cos \theta_p$

and then a bank ϕ_b, the matrix of which is

$[\phi_b]$

	x_a'	y_a''	z_a''
x_a'	1	0	0
y_a	0	$\cos \phi_b$	$\sin \phi_b$
z_a'	0	$-\sin \phi_b$	$\cos \phi_b$

the resulting matrix is

$[\phi_b] \times [\theta_p]$

	x_a'	y_a''	z_a''
X	$\cos \theta_p$	$-\sin \theta_p \sin \phi_b$	$\sin \theta_p \cos \phi_b$
Y	0	$\cos \phi_b$	$\sin \phi_b$
Z	$-\sin \theta_p$	$-\cos \theta_p \sin \phi_b$	$\cos \theta_p \cos \phi_b$

If in addition a turn λ is made about a vertical axis, the matrix becomes

$[M]$

	x_a'''	y_a'''	z_a'''
X	$\cos \theta_p \cos \lambda$	$-\sin \theta_p \sin \phi_b \cos \lambda - \cos \phi_b \sin \lambda$	$\sin \theta_p \cos \phi_b \cos \lambda - \sin \phi_b \sin \lambda$
Y	$-\cos \theta_p \sin \lambda$	$\cos \phi_b \cos \lambda - \sin \theta_p \sin \phi_b \sin \lambda$	$-\sin \phi_b \cos \lambda - \sin \theta_p \cos \phi_b \sin \lambda$
Z	$-\sin \theta_p$	$-\cos \theta_p \sin \phi_b$	$\cos \theta_p \cos \phi_b$

so that from Eq. (1) and comparison of $[L]$ and $[M]$

$$\tan p_1 = \frac{l_6}{l_9} = -\tan \phi_b, \qquad p_1 = -\phi_b$$

$$-\sin p_2 = l_3 = -\sin \theta_p, \qquad p_2 = \theta_p$$

$$\tan p_3 = l_5/l_2 = (\cos \phi_b \cos \lambda - \sin \theta_p \sin \phi_b \sin \lambda)/(-\cos \theta_p \sin \lambda)$$

and, solving for Δp_1, Δp_2, Δp_3 from Eqs. (5), (6), and (7),

Case I

$$\begin{aligned} \Delta p_1 &= -\tan \theta_p \cos \phi_b \psi \\ \Delta p_2 &= -\sin \phi_b \psi \\ \Delta p_3 &= \psi \end{aligned} \tag{14}$$

Case II

$$\begin{aligned} \Delta p_1 &= -\phi \\ \Delta p_2 &= 0 \\ \Delta p_3 &= [(-\cos^2 p_3 \sin \theta_p - \sin \phi_b \cos \theta_p \sin p_3 \cos p_3)/(\cos \phi_b \cos \theta_p)]\,\phi \end{aligned} \tag{15}$$

Case III

$$\begin{aligned} \Delta p_1 &= \tan \theta_p \sin \phi_b \theta \\ \Delta p_2 &= \cos \phi_b \theta \\ \Delta p_3 &= [(\sin \theta_p \sin p_3 \cos p_3 + \sin \phi_b \cos \theta_p \sin^2 p_3)/(\cos \phi_b \cos \theta_p)]\theta \end{aligned} \tag{16}$$

It may be seen that in this case, if no computer is used, roll and yaw, yaw and pitch interact through the gyros, but that roll and pitch still do not interact. The pitch gyro sensitivity is, however, decreased by the factor $\cos \phi_b$.

Alternative Arrangement of Vertical Gyro

In the preceding discussion, the axis of the outer gimbal of the vertical gyro was made to coincide initially with the X-axis. If, instead, it is made to coincide with the Y-axis, then a similar discussion will hold.

The details will not be repeated, but in the case of the coordinated turn the result will be

Case I

$$\begin{aligned} \Delta p_1 &= -\tan \phi_b \psi \\ \Delta p_2 &= 0 \\ \Delta p_3 &= \psi \end{aligned} \tag{17}$$

Case II

$$\begin{aligned} \Delta p_1 &= 0 \\ \Delta p_2 &= \phi \\ \Delta p_3 &= -[(\sin \phi_b \tan \lambda)/(\cos^2 \phi_b + \tan^2 \lambda)]\phi \end{aligned} \tag{18}$$

Case III

$$\begin{aligned} \Delta p_1 &= -\theta \\ \Delta p_2 &= 0 \\ \Delta p_3 &= -[(\sin \phi_b \cos \lambda)/(\cos^2 \phi_b + \tan^2 \lambda)]\,\theta \end{aligned} \tag{19}$$

Note that in this case Δp_1 represents the pitching error and Δp_2 the rolling error. Interaction again will exist between pitch and yaw if no computer is used, but more violently, because of the $\tan \phi_b$ factor in Eq. (17) as compared to the $\sin \phi_b$ factor in Eq. (10). On the other hand, none of the gyro sensitivities, insofar as the normal control signals are concerned, are lowered by the maneuver, ϕ_b, as was the pitch sensitivity in the previous arrangement.

Conclusions

Gyro interactions will in general occur between yaw-pitch and yaw-roll if no computer as given by Eq. (9) is used. The computer necessary, however, would be a complex affair and probably not practical. One method of reducing the gyro interaction during a coordinated turn would be to cut off the direction gyro during such a turn and utilize some other sensing device, such as a rate gyro (displacement signals not being necessary for the period of the turn), for stabilization purposes. It should also be mentioned that in actual flight tests such interactions have been noticed but are not disturbing for departures from level flight below about 45°.

Effect of Turbulence Level of Incident Air Stream on Local Heat Transfer and Skin Friction on a Cylinder

W. H. GIEDT*

University of California at Berkeley

ABSTRACT

At the conclusion of a previous investigation[1] of local heat-transfer and local pressure coefficients around a cylinder, the need for simultaneous local skin-friction coefficient measurements was indicated. In addition, the results of the skin-friction measurements of Fage and Falkner[2] suggested that the influence of the turbulence level in the free air stream on the local heat transfer should be investigated. Data were therefore taken and are presented herein for the local heat-transfer coefficient, pressure coefficient, and skin-friction coefficient on a cylinder below and in the critical range of Reynolds Number. The effect of artificially increased turbulence in the free air stream on these local quantities was also determined. Data for these quantities, taken under identical flow conditions and on models of the same geometry, have not been available previously. The results are partly explicable in terms of available theory and experience and in part present new effects requiring further consideration.

NOMENCLATURE

A = area of heat-transfer surface, ft.^{2}
D = outside diameter of cylinder with nichrome ribbon around it, ft.
h_θ = unit heat-transfer coefficient at cylinder surface at angle θ, B.t.u./hr.-ft.^{2} °F.
i = current flowing through nichrome ribbon, amps.
k_a = thermal conductivity of air, B.t.u./hr.-ft.^{2} (°F./ft.)
p = static pressure at any point on the cylinder surface, lb./ft.^{2}
p_0 = free-stream static pressure, lb./ft.^{2}
Δp = pressure reading of surface tube above local static pressure, lb./ft.^{2}
q = rate of heat transfer by convection from cylinder surface at any point defined by the angle θ, B.t.u./hr.
R = electrical resistance of nichrome ribbon at 70°F., ohms/ft. of length
t = temperature of nichrome ribbon at any point around the cylinder, °F.
t_0 = free air-stream temperature, °F.
U_0 = free air-stream velocity, ft./sec.
U = velocity at edge of boundary layer, ft./sec.
u' = average value of turbulent velocity fluctuation behind grid, ft./sec.
x = distance around cylinder circumference measured from stagnation point, ft.
y = distance from nichrome ribbon measured perpendicular to cylinder surface, ft.
β = slope of velocity distribution at the edge of the boundary layer at the stagnation point, ft./sec./ft.
μ = absolute viscosity of air, lb.-sec./ft.^{2}
θ = angle at center of cylinder measured from the forward stagnation point, deg.
ρ_0 = mass density of air in free stream, lb.-sec.^{2}/ft.^{4}
τ_0 = shear stress at wall of cylinder, lb./ft.^{2}
$\tau_0/\rho_0 U_0^2 = (C_f/2)_{U_0}$ = intensity of skin friction at the cylinder wall based on free-stream velocity
$\tau_0/\rho_0 U^2 = (C_f/2)_U$ = intensity of skin friction at the cylinder wall based on local velocity at the edge of the boundary layer
$\nu = \mu/\rho_0$ = kinematic viscosity, ft.^{2}/sec.
$C_p = \dfrac{p - p_0}{(1/2)\rho_0 U_0^2}$ = local pressure coefficient
C_D = cylinder drag coefficient
$(N_{Nu})_\theta = h_\theta D/k_a$ = Nusselt Number based on h_θ
$(N_{Re}) = DU_0\rho_0$ = Reynolds Number based on cylinder diameter
$(N_{Pr}) = \mu C_p/k_a$ = Prandtl Number for air
$ST = h_\theta/(\rho_0 U C_p)$ = Local Stanton Number

INTRODUCTION

WORK ON THE INVESTIGATION to be described began with measurements of local skin-friction coefficient distributions on a circular cylinder normal to an air stream. These data were desired to supplement previous heat-transfer and pressure coefficient measurements on a cylinder[1] in order to determine if some readily recognizable relationship existed between the heat-transfer and skin-friction coefficients in the turbulent boundary-layer region. The results of these measurements, which were made with a surface tube and in the same air stream as used for taking the previous heat-transfer data, showed that, throughout the entire range of Reynolds Number (70, 800 to 219,000), laminar separation occurred before the 90° point, and in no case was there a turbulent boundary layer present on the back half of the cylinder as the heat-transfer and pressure distributions had indicated.

This testing was conducted in a 3-ft. open-throat-type tunnel (see Fig. 1) with the test section exactly in the center of a cylinder, which extended 2 in. on each end beyond the edge of the wind stream. Further measurements were made after installing some plates on the cylinder parallel to the air flow about 12 in. on either side of the center and placing a $^1/_2$-in. mesh wire screen across the wind-tunnel nozzle exit. A noticeable change in the pressure coefficient distribution occurred, and, at the higher Reynolds Numbers, a small turbulent boundary layer appeared. This indicated that, al-

Received February 19, 1951.
*Assistant Professor, Division of Mechanical Engineering.

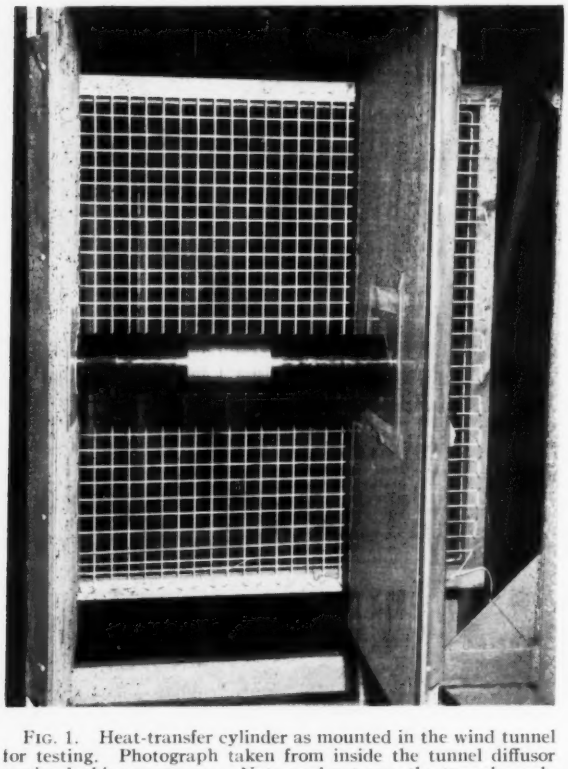

FIG. 1. Heat-transfer cylinder as mounted in the wind tunnel for testing. Photograph taken from inside the tunnel diffusor section looking upstream. Note cord net over the tunnel nozzle exit.

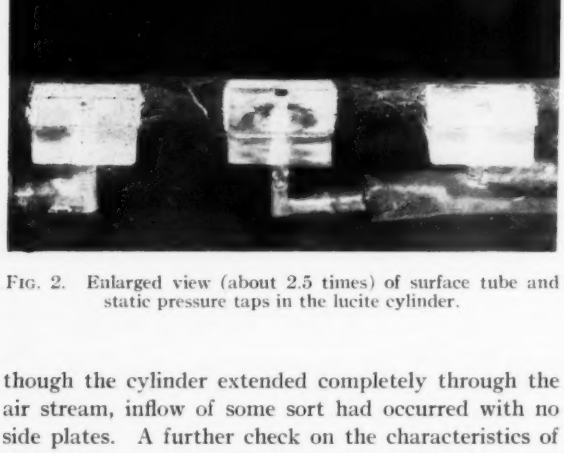

FIG. 2. Enlarged view (about 2.5 times) of surface tube and static pressure taps in the lucite cylinder.

though the cylinder extended completely through the air stream, inflow of some sort had occurred with no side plates. A further check on the characteristics of the air flow around the cylinder with no side plates was obtained by determination of a form drag coefficient from the pressure distribution curves. Since in this region of Reynolds Number form drag constitutes in general 98 per cent or more of the total drag (p. 428, reference 3), these values should have compared favorably with accepted data. They failed to do this, and it was therefore considered desirable to repeat the heat-transfer and pressure distribution along with skin-friction measurements under improved airflow conditions and variable air-stream turbulence.

This does not necessarily invalidate the previous data but indicates that caution is necessary in its interpretation. An examination of the work of Schmidt and Wenner,[4] which is the other most recent investigation of this nature, indicated that their air stream also possessed serious limitations. This will be discussed in more detail later.

Experimental Equipment and Procedure

The extended test program involved the use of two models: a heat-transfer cylinder fitted with electrically heated surface ribbons, as shown in Fig. 1, and a cylinder fitted with a surface tube, as shown in Fig. 2, for the skin-friction and pressure measurements. They were mounted, as shown in Fig. 1, in the University of California 3-ft. wind tunnel. The environment for the tests was, therefore, exactly the same for the heat-transfer and skin-friction test cylinders. A more detailed description of their construction as well as the test technique employed is given in the Appendix.

The primary parameter involved in the test program was the variation of the turbulence level of the incident air stream. Data were taken first with a 16-mesh damping screen placed upstream of the wind-tunnel nozzle in order to minimize the turbulent fluctuations occurring in the normal tunnel stream. The estimated turbulence level, u'/U_0, was negligible, being of the order of less than 1 per cent.[5] In contrast to this, data were then taken with greatly increased tunnel turbulence, accomplished by placing a 1.25- by 1.25-in. rope net ($^3/_{16}$-in. diameter shot cord) over the nozzle exit. The cylinder leading edge was placed about 24 in. behind this net, the test arrangement being shown in Fig. 1. The estimated turbulence level in this case was of the order of 4 per cent.[6] Data were also taken at the maximum velocity obtainable in the normal tunnel stream insofar as this nominally extended the Reynolds Number range of the investigation.

Heat-transfer data and the pressure and skin-friction data were taken separately but at as nearly the same Reynolds Number as could be realized by the air-stream speed control. All Reynolds Numbers are based on free-stream velocities calculated from the rise in pressure at the cylinder stagnation point referred to the static pressure indicated by a pitot tube in the air stream 10 in. upstream from the cylinder leading edge with the stagnation point pressure coefficient assumed to be unity.

Presentation and Discussion of Results

Local Heat-Transfer, Pressure, and Skin-Friction Distributions

Representative curves of the experimental results throughout the test range of Reynolds Number for local

values of heat-transfer, pressure coefficient, and skin-friction coefficient distributions are plotted in Figs. 3, 4, and 5. Referring to Fig. 3, it is noted that all of the heat-transfer curves, with the exception of the one for Reynolds Number equal to 99,300, are what might be described as characteristic of the critical range—i.e., they have two maximums and two minimums (the critical range refers to the Reynolds Number region in which the rapid drop in the cylinder drag coefficient occurs). The data for Reynolds Number equal to 99,300 are definitely associated with the pre-critical range with laminar separation as is indicated by the magnitude of the overall drag coefficient (see Fig. 6) and also by the local skin friction as shown on Fig. 5. The coincidence of the location on the cylinder surface of the minimum heat-transfer coefficient and the zero value of the skin-friction coefficient, which presumably indicated laminar separation, should be noted. Flow conditions for Reynolds Number equal to 167,500 appear to be of a transitional nature. The skin-friction data do not show the presence of a turbulent boundary layer, but neither does the skin-friction coefficient decrease to zero as rapidly as for the case with Reynolds Number equal to 99,300. The curves of Fig. 5 for the other three values of Reynolds Number show definite skin-friction magnitudes in the region $\theta > 90°$, and such boundary layers as exist in this region can be presumed to be turbulent in nature.

The pressure coefficient curves of Fig. 4 reveal definite inflection points in the 90° region for Reynolds Numbers of 90,300, 172,000, and 212,000, as have been previously noted by Fage and Falkner and assumed by them to indicate the point of transition from laminar to turbulent flow in the boundary layer. Form drag coefficients obtained from the local pressure as recommended by Goldstein (Fig. 161, p. 431, reference 3), confirm the flow over the test cylinders as being in the critical range. As a matter of interest, the pressure distribution curves given by Schmidt and Wenner[4] were integrated also, and the form drag coefficients are also shown in Fig. 6. As can be noted, they do not check with the accepted curves. The reason for this is that their test arrangement did not provide the effect of a cylinder in an infinite stream. A curve typical of their data at higher values of Reynolds Number is included in Fig. 4. This is the type of curve obtained previously by the author[1] and, when considered in the light of the experience of this investigation, indicates that even at the maximum Reynolds Number 426,000 obtained by Schmidt and Wenner, laminar separation without any turbulent boundary layer probably occurred.

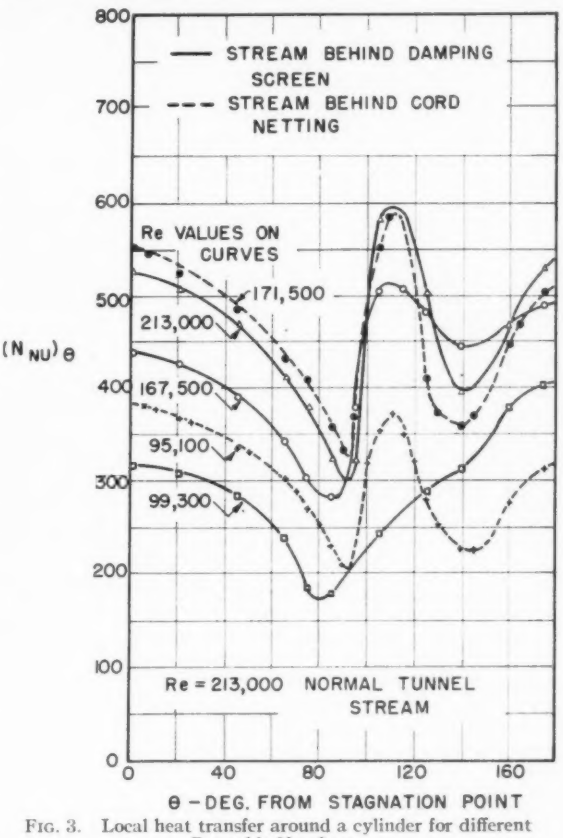

FIG. 3. Local heat transfer around a cylinder for different Reynolds Numbers.

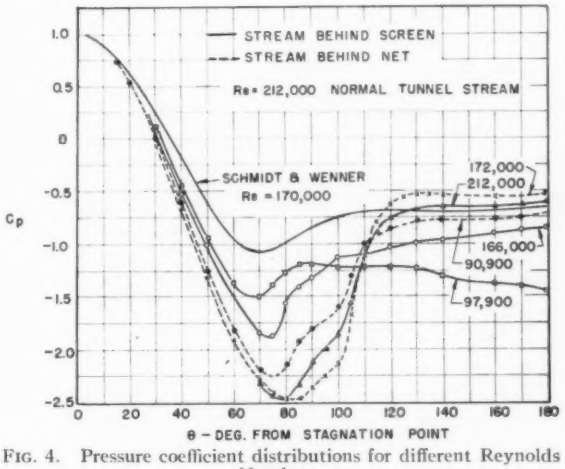

FIG. 4. Pressure coefficient distributions for different Reynolds Numbers.

Relative Effect of Free-Stream Turbulence

Comparison of the data taken in the stream behind the damping screen to that taken at comparable values of free-stream velocities in the stream behind the cord net shows that the general effect of the net is to produce results characteristic of velocities higher than those indicated by the free-stream velocity. This is in agreement with results obtained by previous investigators, particularly in regard to the marked reduction in form drag produced by the increase in free-stream turbu-

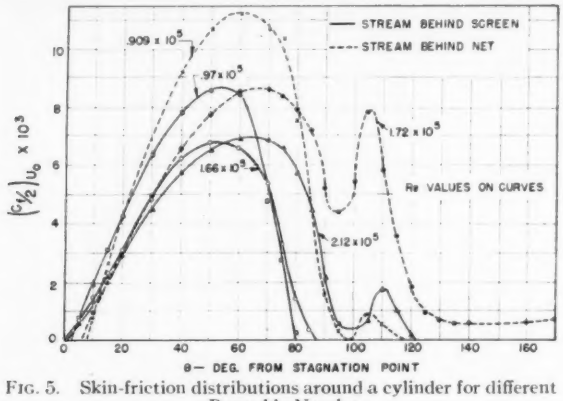

FIG. 5. Skin-friction distributions around a cylinder for different Reynolds Numbers.

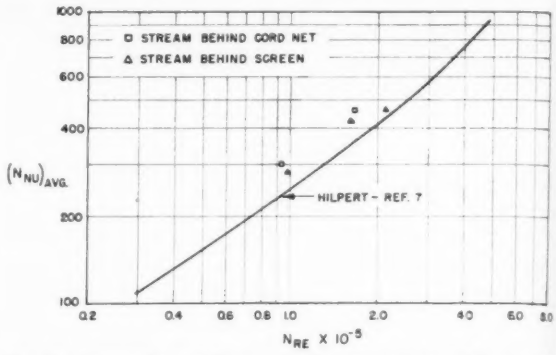

FIG. 7. Comparison of the average heat-transfer coefficient with Hilpert's experimentally determined curve.

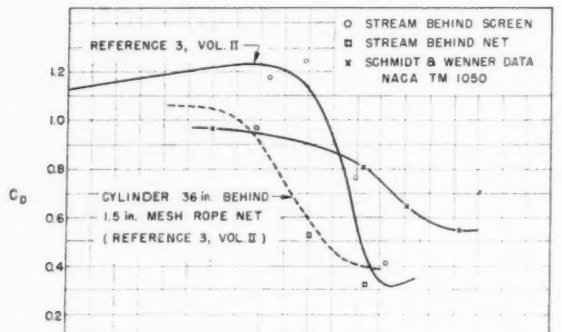
REFERENCE 3, VOL. II
STREAM BEHIND SCREEN
STREAM BEHIND NET
SCHMIDT & WENNER DATA NACA TM 1050
CYLINDER 36 in. BEHIND 1.5 in. MESH ROPE NET (REFERENCE 3, VOL. II)
C_D
LOG_10 Re

FIG. 6. Cylinder drag coefficient vs. Reynolds Number.

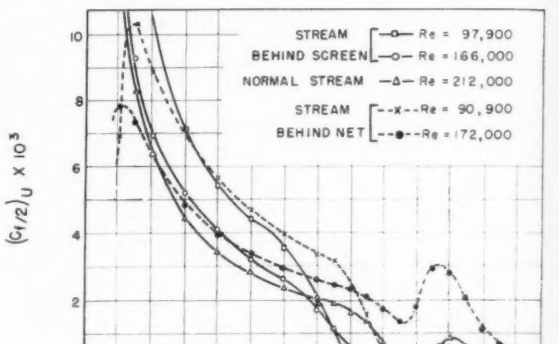

FIG. 8. Local skin-friction coefficient distribution based on velocity at edge of boundary layer.

lence. The average heat-transfer coefficient reveals a similar but not as significant a trend. Fig. 7 shows that the increased turbulence caused the average heat-transfer coefficient to increase between 10 and 20 per cent over the low turbulence level values.

The average heat-transfer coefficient does not indicate, however, the effect of the increased turbulence on the change in the relative amounts of heat transfer from the front and back halves of the cylinder. In the low turbulence level air stream, the ratio of front- to back-half heat transfer is approximately 0.85. In the stream behind the net, this increases to around 1.1. The change is due both to an increase of the heat transfer on the front half and to a decrease on the back half of the cylinder.

Heat-Transfer Coefficient at the Stagnation Point

Fig. 3 reveals that, for comparable values of free-stream velocities, the local heat-transfer coefficients at the stagnation point as obtained in the stream behind the cord net are approximately 25 per cent higher than those obtained in the stream behind the screen.

For the case of a heated cylinder normal to an air stream, where the velocity distribution at the edge of the boundary layer near the forward stagnation point is a linear function of the distance from that point, so that $U = \beta_1 x$, the value of the Nusselt Number at the stagnation point has been determined analytically by Squire[3] (p. 631) to be: $(N_{Nu})_{ST} = \alpha_3(N_{Pr})(\beta_1 D^2/\nu)^{1/2}$. β_1 is the slope of the velocity distribution at the edge of the boundary layer, D the cylinder diameter, ν the kinematic viscosity, and $\alpha_3(N_{Pr})$ a known function of the Prandtl Number, which is tabulated in reference 3. The velocity distributions at the edge of the boundary layer as determined from the experimental pressure data were linear with x. The slopes of these distributions were determined graphically and used to determine the theoretical value of the Nusselt Number at the stagnation point in accordance with the above equation. These values as well as the experimentally observed values of $(N_{Nu})_{ST}$ are listed in Table 1 and the per cent deviation noted.

The deviations from the theoretical predictions are larger for the case of the stream behind the rope netting, but a conclusive explanation for the effect is

TABLE 1

Comparison of Theoretical and Experimental Values of N_{Nu} at the Stagnation Point

[NOTE: $\alpha_3(N_{Pr}) = 0.499$]

Stream Condition	N_{Re}	β_1, (ft./sec.)/ft.	$(N_{Nu})_{ST}$, Theoretical (Squire)	$N(_{Nu})_{ST}$, Experimental	Per Cent Deviation
Damping screen	99,300	565	314	317	9.95
upstream	167,500	987	407	438	7.6
Stream behind net	95,100	530	307	384	25.1
	171,500	1,030	414	552	33.3
Normal stream	213,000	1,260	460	525	14.0

lacking at the present time. In this regard, the anomalous behavior of the shear stress at the wall as indicated by the surface tube is notable. At the stagnation point and up to approximately 8°, in the case of the stream behind the net, the reading of the surface tube was negative with reference to the local static pressure. This has been indicated in Fig. 5 by the omission of skin-friction magnitudes between θ equal to 0 and about 8°. Fage and Falkner[2] did not observe this phenomenon or neglected to mention it. A possible explanation of this occurrence consists in the hypothesis that the original rise in dynamic pressure in a turbulent air stream due to the turbulent velocity fluctuations was registered on the static pressure taps but not on the surface tube. As mentioned previously, the order of magnitude of the turbulent velocity fluctuations was probably about 4 per cent of the free-stream mean velocity, which corresponds to a maximum velocity of 4 ft. per sec. in these tests. Negative pressures were recorded, however, corresponding to velocities of 10 to 15 ft. per sec., indicating that some additional or separate effect was present.

The Laminar Boundary-Layer Region

The increase in local heat transfer, with about the same pressure distribution and free-stream velocity, produced by the more turbulent free stream in the tests made with the net, which has been noted for the stagnation point region, extended also over the entire reach of the laminar boundary-layer flow. Because a comparable effect is not revealed in the skin-friction results (Fig. 8), it may be possible that the turbulent flow in the region adjacent to the hydrodynamic boundary layer was sufficiently nonisotropic to augment the molecular conduction of heat in this external region, which occurs with fluids of Prandtl Number less than unity. Such an effect would, in part, account for the high heat-transfer coefficients observed. Also, it may be possible that the observed phenomenon was due to the action of the turbulent stream near the edge of the laminar boundary layer. However, if this were true, a slight increase in the skin friction should also

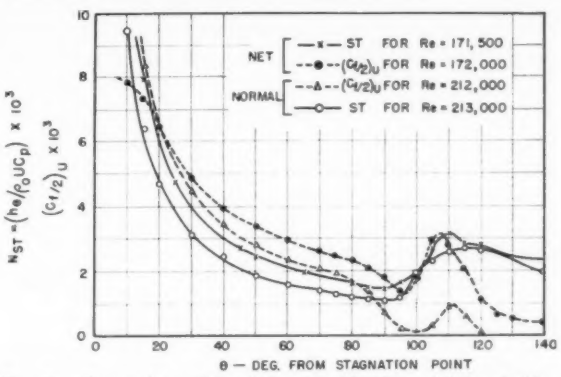

FIG. 9. Comparison of local Stanton Number with local skin-friction coefficient.

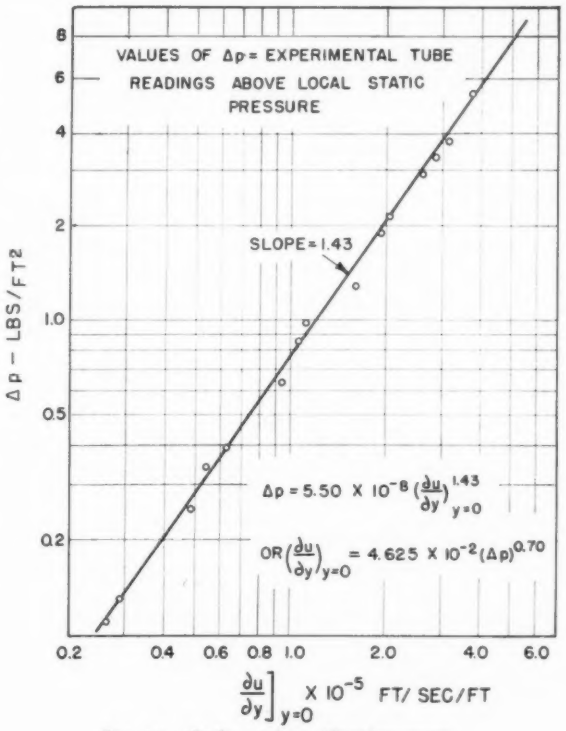
VALUES OF Δp = EXPERIMENTAL TUBE READINGS ABOVE LOCAL STATIC PRESSURE
SLOPE = 1.43
Δp = 5.50 X 10⁻⁸ (∂u/∂y)^1.43 y=0
OR (∂u/∂y)y=0 = 4.625 X 10⁻² (Δp)^0.70
Δp — LBS/FT²
∂u/∂y]y=0 X 10⁻⁵ FT/SEC/FT

FIG. 10. Surface tube calibration curve.

result. Referring to Fig. 8, which shows the distribution of the skin friction coefficients based on the local velocity at the edge of the boundary layer, it can be seen that the data for the tests behind the cord net are, in general, below or approximately equal to those for the stream behind the damping screen. This is felt to be inconsistent and could be properly explained only with further information about the boundary-layer characteristics in the turbulent stream.

The Turbulent Boundary-Layer Region

A comparison of the local heat transfer and skin friction in Figs. 3 and 8 also reveals effects inexplicable

in terms of available rationalizations. Fig. 3 shows, for the region from about 100° to 130°, substantially similar heat-transfer coefficients for the tests at values of Reynolds Numbers equal to 172,000 behind the net and 213,000 in the normal tunnel stream. The skin-friction magnitudes, however, are different. This comparison is shown in Fig. 9. Thus, for the turbulent flow region, a consistent relation between the local Stanton Number and the skin-friction coefficient, such as obtains for flat-plate flow, does not appear to exist in simple form for a cylinder.*

The Wake Region

In general, all the heat-transfer coefficients† in the wake region have a minimum value at the point of separation, whether it be laminar or turbulent, and increase rapidly to a maximum at the rear stagnation point. From the shapes of the curves, it seems possible that, due to reverse flow, a boundary layer is formed at the rear stagnation point and builds up in the direction of the point of separation. This possibility was examined by means of surface tube measurements taken with the cylinder reversed in the air stream, so that the surface tube faced the rear stagnation point. Because of the small response of the tube in this region, conclusive evidence was not obtainable. Some indications tended to confirm a backward flow in this region, while others indicated fluctuations of the velocity from the forward to the backward direction.

Bibliography

[1] Giedt, W. H., *Investigation of Variation of Point Unit Heat-Transfer Coefficient Around a Cylinder Normal to an Air Stream*, Transactions of A.S.M.E., Vol. 71, May, 1949.

[2] Fage, A., and Falkner, F. M., *Further Experiments on the Flow Around a Cylinder*, R&M No. 1369, Great Britain Aeronautical Research Committee, 1931.

[3] *Modern Developments in Fluid Mechanics*, by the Fluid Motion Panel of the Aeronautical Research Committee; Edited by S. Goldstein, Oxford University Press, London, 1938.

[4] Schmidt, E., and Wenner, K., *Heat Transfer Over the Circumference of a Heated Cylinder in Transverse Flow*, N.A.C.A. T.M. No. 1050, October, 1943.

[5] Dryden, H. L., and Schubauer, G. B., *The Use of Damping Screens for the Reduction of Wind Tunnel Turbulence*, Journal of the Aeronautical Sciences, Vol. 14, No. 4, pp. 221–228, 1947.

[6] Dryden, H. L., *A Review of the Statistical Theory of Turbulence*, Quarterly of Applied Mathematics, Vol. I, pp. 7–42, April, 1943.

[7] Hilpert, R., *Experimental Study of Heat Dissipation of Heated Wire and Pipe in an Air Current*, Forschung auf dem Gebiete des Ingenieurwesens, Vol. 4, pp. 215–224, 1933.

[8] Taylor, G. I., *Measurements with a Half-Pitot Tube*, Proceedings of the Royal Society, Series A, Vol. 166, pp. 476–481, 1938.

[9] Howarth, L., *Steady Flow in the Boundary Layer Near the Surface of a Cylinder in a Stream*, R&M No. 1632, July, 1934.

* It is recognized that differences in the pressure distributions which do exist may influence this relation.

† It is to be noted that the local heat-transfer coefficient is defined in terms of the free-stream temperature, presumed, because of the negligible compressibility, to exist at the outer edge of the boundary layer. This is not true in the wake region, and, in consequence, local heat-transfer coefficients as shown for this region are to some extent fictive.

Appendix

Measurement of Local Heat-Transfer Coefficients

The heat-transfer cylinder was constructed from 4-in. outside diameter and $^1/_8$-in. wall thickness Bakelite tubing. It was 21 in. overall in length and was mounted for testing between side plates 20 in. apart as shown in Fig. 1. The model was divided into three sections, of which the center $6^1/_2$ in. constituted the test section. Five separate, 1 by 0.002 in. in cross section, nichrome heating ribbons were fitted around this section, the center one being the test strip and the two on either side acting as guard heating strips. Measurement of current input to the ribbons and temperature variation along the ribbons by means of extremely fine thermocouples located immediately under the center ribbon enabled the calculation of the local heat-transfer coefficients, h_θ, due to the relationship

$$h_\theta = (q/A)/(t - t_0) \sim (i^2R)/(t - t_0)$$

The actual equation used, accounting for conduction and radiation losses, is derived and discussed in detail in reference 1. The final accuracy of h_θ is considered to be well within 10 per cent except possibly at the maximum and minimum points.

Skin-Friction Measurements with the Surface Tube

The surface tube located in the wall of the 4-in. lucite cylinder is shown in Fig. 2. The cylinder was mounted in the 3-ft. wind tunnel in the same manner as the heat-transfer cylinder shown in Fig. 1. The surface tube itself projected about 0.0035 in. above the cylinder surface and had an opening of approximately 0.08 by 0.003 in. A static pressure tap was located $1^1/_2$ in. on either side of the surface tube. Experimental measurements consisted of determining the difference in pressure between it and the average of the static pressure taps as the cylinder was rotated about its axis. Several types of micro-manometers were tried for this purpose. However, it was eventually found that due to the air-stream fluctuations, an ordinary inclined manometer with a scale having a least count of 0.01 in. of water provides sufficient accuracy and was easier to use. Readings were estimated to 0.002 in. of water, but an accuracy of greater than 0.01 in. cannot be justifiably claimed.

A considerable amount of time and effort was devoted to the calibration of the tube. Space does not permit describing this in detail, but, in general, results indicated that the accuracy claimed in previous work was open to question. In addition, the "effective distance" type of calibration[2,8] was considered misleading from a

(*Continued on page 766*)

On the Stability of Two-Dimensional Laminar Jet Flow of Gas

S. I. PAI†

Institute for Fluid Dynamics and Applied Mathematics, University of Maryland

SUMMARY

The stability of two-dimensional laminar jet-type flow of both an incompressible fluid and a compressible fluid has been investigated by the method of small perturbations. Both the symmetrical and the antisymmetrical disturbances are investigated separately.

In the case of incompressible fluid, the solutions of neutral stable disturbances in an inviscid fluid are first obtained. Then the case of viscous fluid is analyzed. Both the symmetrical and the antisymmetrical disturbances are unstable for large Reynolds Numbers, but the region of instability of symmetrical disturbances lies inside that of the antisymmetrical one. The general shape of the neutral stable wave number against Reynolds Number curve of the jet-type flow is different from that of the velocity profile of ordinary boundary-layer flow or Poiseuille flow. First, the effect of viscosity on the neutral stable disturbance in inviscid fluid is always stabilizing for jet-type flow. Second, when the wave number tends to zero and the Reynolds Number is large, the jet-type flow is always unstable. Hence, for the upper branch of the neutral stable wave number against Reynolds Number curve, wave number increases with Reynolds Number, and there is no lower branch of this neutral stable curve for the jet-type flow.

In the case of compressible fluid, the asymptotic behavior of the solutions at infinity is discussed. The stability of a two-dimensional jet of inviscid fluid is analyzed, and the cases of viscous fluid are indicated. There is some similarity in the solutions of the case of compressible fluid and of the case of incompressible fluid.

So far as laminar stability is concerned, an important difference exists between the case of supersonic and subsonic disturbances relative to the velocity of the surrounding stream of the jet. The amplitude of the subsonic disturbance dies out rapidly with the distance from the axis of the jet. The neutral supersonic disturbances are actually progressive sound waves whose wave length and phase velocity are completely arbitrary and that have no significance for stability of the jet flow.

When the Mach Number of the maximum velocity of the jet relative to the velocity of the surrounding stream is high enough, the jet-type flow tends to be stable with respect to small disturbances.

List of Symbols

The following symbols are used in both Part I and Part II.

a = velocity in the jet at $y = \pm\infty$

$^*A_n, B_n, E_n, D_n$ = functions in asymptotic expression of ϕ at large y

c = $c_R + ic_i$ complex velocity of propagation of disturbances

$^*F_1, F_2$ = determinantal equations for disturbance

$^*k_{2n}$ = functions in expansion of $\phi_1^{(0)}$

i = $\sqrt{-1}$

$^*k_{2n+1}$ = functions in expansion of $\phi_2^{(0)}$

L = characteristic length

$^*p_{2n}$ = functions in expansion of $\phi_1^{(1)}$

$^*q_{2n+1}$ = functions in expansion of $\phi_2^{(1)}$

R = UL/ν = Reynolds Number

t = nondimensional time

u' = nondimensional x-wise perturbation velocity

v' = nondimensional y-wise perturbation velocity

U = characteristic velocity (velocity at the axis of the jet)

w = nondimensional x-wise main velocity

x = nondimensional distance along axis of jet

X = dimensional x-wise distance

y = nondimensional distance perpendicular to axis of jet

α = wave number

ν = coefficient of kinematical viscosity

ρ = nondimensional density

ϕ = amplitude of disturbance function of ψ' in Part I; of v in Part II

$^*\Phi_{k\,\infty}^{(j)}$ = functions in asymptotic expression of ϕ at large y

* The exact expressions for these symbols for Part I and Part II are not the same but they are similar so that same symbols are used.

Subscripts

R = real part of the expression

i = imaginary part of the expression

The following symbols are used in Part II only:

C_p = specific heat at constant pressure

f = amplitude of x-wise perturbation velocity

M = Mach Number of the velocity at the axis of the jet

r = amplitude of perturbation density

p = nondimensional pressure

T = nondimensional temperature

Z_i = perturbation variable in general

z = Ωy

γ = ratio of specific heats

θ = amplitude of perturbation temperature

μ_1, μ_2 = 1st and 2nd coefficient of viscosity, respectively

π = amplitude of perturbation pressure

Ω = $(1 - \{[M^2(a-c)^2]/Ta\})^{1/4}$

All the nondimensional quantities are in terms of those values at the axis of the jet—i.e., $y = 0$.

Presented at the Aerodynamics Session, Nineteenth Annual Meeting, I.A.S., New York, January 29—February 1, 1951.

† Research Associate.

INTRODUCTION

ONE OF THE MOST INTERESTING PROBLEMS in fluid dynamics is the problem of hydrodynamic stability. It is concerned with the origin of turbulence. Extensive theoretical investigations of this problem were made by Tietjens,[1] Heisenberg,[2] and Tollmien[3, 4] in the 1920's.

In recent years much investigation,* both theoretical and experimental,[5] has been carried out for various types of laminar flow. However, most of these investigations deal with those classes of velocity profile that involves at least one solid boundary—e.g., boundary-layer flow, flow through a channel, etc., but little has been done for the class of velocity profile of jet type—i.e., the range of the velocity perpendicular to the main flow extending to both plus and minus infinity.

The stability of velocity distribution of jet-type flow of incompressible fluid was first treated by Hollingdale[6] and Savic.[7] Their results are limited to inviscid fluids and their assumption that symmetrical disturbances do not produce instability is not correct. Lessen[8] and Chiarulli[9] studied the stability of the half-jet-type flow. Chiarulli has developed a simplified method of calculation which is very useful in the study of stability of jet-type flow. But he did not carry out the calculations. Little has been done about two-dimensional laminar jet-type flow, including viscosity effect.

In the first part of the present paper, the stability of two-dimensional laminar jet-type flow of an incompressible fluid has been investigated by Heisenberg-Lin[10] method with the help of Chiarulli's simplified method of calculation.[9] Both the symmetrical and the antisymmetrical disturbances are investigated separately. The solutions of neutral stable disturbance in an inviscid fluid are first obtained. Then the cases of viscous fluid are analyzed. The eigen value equations are obtained in closed form and the calculation of the eigen values is reduced to straightforward evaluation of certain definite integrals. The neutral stable curve in the wave number α and Reynolds Number R plane can be thus calculated. The general shapes of the neutral curve are discussed. It is shown that the general shape of the neutral curve of the jet-type flow is quite different from that of the velocity profile of ordinary boundary-layer flow or Poiseuille flow.

The velocity profile of the main flow used in the calculation is that of the two-dimensional jet issuing from a small slit into fluid at rest. We assume that the fluid is incompressible and that the Reynolds Number is large; hence the velocity in the jet must be small and the distance from the nozzle must be large. As a result, the velocity profile of jet from small slit is justified to be used. However, the case for velocity profile of finite opening of the nozzle is discussed. The essential characteristics of the neutral curve will be the same for the finite opening case as that for the small slit but the numerical values of the neutral αR curve will be different in the two cases.

Because of the increasing importance of high speed flow from jet engine, it seems natural that the above investigation should be extended to cover the case of compressible fluid taking into account the effects of compressibility and heat transfer.

The interest in the problem of compressible fluid is further enhanced by the fact that the laminar flow of very high Mach Number tends to be completely stable with respect to small disturbances. Lees[11] has shown that for Mach Number greater than three, the laminar boundary-layer flow for thermal equilibrium is completely stable at all Reynolds Numbers under free-flight conditions if the free-stream velocity is uniform. Landau[12] and Hiroshi Hatanaka[13] both showed that if the relative Mach Number of a surface of discontinuity in an inviscid compressible fluid is large enough the vortex sheet will be stable with respect to small disturbances. Hence, it will be interesting to determine whether the jet-type flow will be stable at high Mach Number for all Reynolds Numbers. If so, what would be the approximate value of this critical Mach Number?

As in the incompressible fluid case, only small two-dimensional wavy disturbances will be considered for the compressible fluid case. Unfortunately, there is no rigorous proof in the compressible fluid case that these disturbances are more unstable than the three-dimensional ones. But the results of the incompressible fluid[14] together with some physical considerations seem to justify such a treatment that naturally simplifies the mathematical analysis to a large extent.

One essential difference in the case of compressible fluid from that of incompressible fluid is the presence of an appreciable interchange of mechanical and heat energies. Another is the fact that the flow velocity is of the same order of magnitude as the velocity of sound.

The method of analysis used for compressible fluid is very similar to that used in the incompressible fluid case. Special reference should be made to the work of Lees and Lin[15] who studied the stability equations of two-dimensional parallel flow of compressible fluid and their solutions in great details. Most of their results will be used in this paper. Here our emphasis is placed on the case of laminar jet flow.

A numerical integration method is devised to compute the velocity and the temperature distributions in the two-dimensional jet-type flow without any specific assumptions about the value of Prandtl Number and the law of variation of viscosity with temperature.

The method described in this paper may be also used to study the stability of two-dimensional wake.

Part (I) Jet Flow of Incompressible Fluid

Orr-Sommerfeld Equation and Its Solutions

The fundamental equation of stability of two-dimensional parallel flow and its solutions have been investigated extensively by Lin.[10] We are going to use this method to study the stability of the velocity profile of jet-type flow. First we will summarize some of Lin's results which are useful for present analysis as follows:

* For additional references see Lin's paper (reference 10) and also Dryden's paper, *Recent Advances in the Mechanics of Boundary Layer Flow*, Advances in Applied Mechanics, Vol. I, 1948.

Consider the stability of the velocity distribution $w = w(y)$, by superimposing upon the steady flow a small, hydrodynamically possible disturbance obtained from a disturbance stream function.

$$\psi' = \phi(y)e^{i\alpha(x - ct)} \tag{1.1}$$

where wave number α is a real and positive number and velocity of propagation of disturbance c is in general complex.

If we substitute the resulting disturbed flow into the equations of motion and linearize them, we obtain the stability differential equation that is known as Orr-Sommerfeld equation as follows:

$$(w - c)(\phi'' - \alpha^2\phi) - w''\phi = -(i/\alpha R) \times (\phi^{iv} - 2\alpha^2\phi'' + \alpha^4\phi) \tag{1.2}$$

In this equation all velocities are referred to a characteristic velocity U, all lengths to a characteristic length L; U and L may be functions of x. The Reynolds Number R is equal to UL/ν where ν is the coefficient of kinematic viscosity. Prime represents the derivative with respect to y.

The stability differential Eq. (1.2) has a fundamental system of four solutions that are analytic functions of y (wherever $w(y)$ is analytic) and are entire functions of α, c, and αR. Two of the solutions, called by Lin "viscous solutions," should be rejected in the study of flow of jet type because of the bound of the solution. The other two solutions, known as "inviscid solutions," can be obtained by developing the solution in powers of $(\alpha R)^{-1}$.

$$\phi(y) = \phi^{(0)}(y) + (\alpha R)^{-1}\phi^{(1)}(y) + (\alpha R)^{-2}\phi^{(2)}(y) + \ldots \tag{1.3}$$

Following Heisenberg's procedure, we develop $\phi^{(0)}(y)$ in power of α^2. In terms of Lin's notation, the resulting solutions for $\phi^{(0)}(y)$ are

$$\phi_1^{(0)} = (w - c)[h_0(y) + \alpha^2 h_2(y) + \alpha^4 h_4(y) + \ldots] \tag{1.4}$$

$$\phi_2^{(0)} = (w - c)[k_1(y) + \alpha^2 k_3(y) + \alpha^4 k_5(y) + \ldots] \tag{1.5}$$

where $h_0 = 0$, h_{2n+2}'s and k_{2n+1}'s are functions of y, w, and c which are given in reference 10.

For velocity distribution of jet-type flow, we must include the $\phi^{(1)}$ solutions in the eigen value problem in order to take the effect of viscosity into account.[16] Developing the solutions in powers of α^2, we obtain

$$\phi_1^{(1)} = (w - c)[p_0(y) + \alpha^2 p_2(y) + \alpha^4 p_4(y) + \ldots] \tag{1.6}$$

$$\phi_2^{(1)} = (w - c)[q_1(y) + \alpha^2 q_3(y) + \alpha^4 q_5(y) + \ldots] \tag{1.7}$$

where p_{2n}'s and q_{2n+1}'s are functions of y, w, and c. In reference 9, Chiarulli showed how to calculate these p_{2n} and q_{2n+1} but some of the formulas given in his report seem to be incorrect.

Eqs. (1.6) and (1.7) are not unique in that any linear combination of $\phi_1^{(0)}$ and $\phi_2^{(0)}$ can be added to them. But as shown by Chiarulli,[9] it is sufficient to use these expressions in the eigen value problem.

The solution of the stability differential equation for the velocity distribution of jet-type flow is

$$\phi = c_1\phi_1 + c_2\phi_2 \tag{1.8}$$

where c_1 and c_2 are arbitrary constants.

Asymptotic Behavior of the Solution at Infinity

In the boundary value problem, we have to know the value of $\phi_k^{(j)}$ for large values of y. By the method of Chiarulli,[9] we obtain the value of the $\phi_k^{(j)}$ for y approaches to $-\infty$ and w approaches to a as follows:

$$\phi_k^{(j)} = \Phi_{k+}^{(j)}e^{\alpha y} + \Phi_{k-}^{(j)}e^{-\alpha y} \tag{1.9}$$

where $j = 0$ and 1 and $k = 1$ and 2.

$$\Phi_{1\pm}^{(0)} = -\frac{c - a}{2}[A_0 \pm \alpha A_1 + \alpha^2 A_2 \pm \alpha^3 A_3 + \ldots] \tag{1.10}$$

$$\Phi_{2\pm}^{(0)} = -\frac{c - a}{2}\left[\pm\frac{B_0}{\alpha} + B_1 \pm \alpha B_2 + \ldots\right] \tag{1.11}$$

$$\Phi_{1\pm}^{(1)} = -\frac{c - a}{2}[E_0 \pm \alpha E_1 + \alpha^2 E_2 \pm \ldots] \tag{1.12}$$

$$\Phi_{2\pm}^{(1)} = -\frac{c - a}{2}[D_0 \pm \alpha D_1 + \alpha^2 D_2 \pm \ldots] \tag{1.13}$$

where $A_0 = 1$, A_n, B_n, E_n, and D_n are definite integrals from minus infinity to some reference point y_0 of the function of w, a, and c. Since the velocity distribution $w(y)$ which we are dealing with approaches to a constant value at infinity in an exponential manner,[17] all the infinite integrals converge.

Similar expressions for ϕ's can be obtained for $y \to +\infty$ and $w \to a$.

Boundary Value Problems

We are going to study the boundary value problem for the case of two-dimensional jet flow. The velocity distribution $w(y)$ of the main flow is symmetrical with respect to y. Any function $\phi(y)$ satisfying Orr-Sommerfeld equation may be separated into two parts, respectively odd or even in y, each of which separately must be a solution of the differential equation. The even solution corresponds to antisymmetric oscillation (an alternate vortex sheet), the odd solution, symmetric oscillation. We are going to consider these two types of disturbances separately. The symmetry condition allows us to consider only negative value of y.

(*i*) *Symmetrical Disturbance.*—If $\phi(y)$ is an odd function of y—i.e., symmetrical oscillation—the boundary conditions are

$$\phi(-\infty) = \phi(0) = 0 \tag{1.14}$$

The determinantal equation corresponding to these conditions is

$$F_1(\alpha,c,\alpha R) = \begin{vmatrix} \phi_1(-\infty) & \phi_2(-\infty) \\ \phi_1(0) & \phi_2(0) \end{vmatrix} = 0 \quad (1.15)$$

(*ii*) *Antisymmetrical Disturbances.*—If $\phi(y)$ is an even function of y, antisymmetrical oscillation, the boundary conditions are

$$\phi(-\infty) = \phi'(0) = 0 \quad (1.16)$$

The determinantal equation corresponding to these conditions is

$$F_2(\alpha, c, \alpha R) = \begin{vmatrix} \phi_1(-\infty) & \phi_2(-\infty) \\ \phi_1'(0) & \phi_2'(0) \end{vmatrix} = 0 \quad (1.17)$$

Velocity Distribution of the Main Flow

(*i*) *Small Slit.*—The problem of the jet going out from a long narrow slit in a wall and mixing with the surrounding fluid at rest is one of the rare cases where the differential equation of boundary layer may be integrated exactly. The calculations were performed by Schlichting[18] and Bickley.[19]

Let

U = characteristic velocity = $0.4543(M_0^2/\rho_0^2\nu X)^{1/3}$

L = characteristic length = $(M_0/\rho_0\nu^2X^2)^{-1/3}$

where

M_0 = rate of momentum across a section of the jet

$$= 2U^2\rho_0 L \int_0^\infty w^2 dy$$

ρ_0 is the density of the fluid.

The nondimensional velocity distribution in the jet from a small slit will be

$$w = \operatorname{sech}^2 by \quad (1.18)$$

where

$$b = \frac{1}{3}\left(\frac{9}{16}\right)^{1/2}$$

(*ii*) *Finite Opening.*—In case the jet discharges from a nozzle of finite opening into the surrounding fluid at rest or in uniform motion, the velocity distribution can be numerically integrated by the method given by the author in reference 17. It is noticed that when the distance is small from the exit of the nozzle, the velocity distributions at various sections are not similar. Hence in the study of stability of flow near the exit, it is necessary to find the whole series of distribution first and to make the stability calculations for each velocity distribution. However, the procedures of calculations for each velocity distribution are identical. The problem should not introduce any complications. In the present paper the stability calculations are based on the velocity distribution of small slit in order to bring out some essential features of stability of velocity distribution of jet type. The calculation for velocity profiles of finite opening will be carried out in the future in order to determine the influence of change of velocity profile from a uniform one to that at a large distance.

Neutral Stability in an Inviscid Fluid

The study of the stability problem in an inviscid fluid may be regarded as the limiting case where the Reynolds Number becomes indefinitely large. The stability differential Eq. (1.2) reduces to

$$(w - c)(\phi'' - \alpha^2\phi) - w''\phi = 0 \quad (1.19)$$

This equation has a singularity at $w = c$. It is well known that in an inviscid fluid, all velocity profiles with a point of inflection are unstable and tend to exhibit oscillation.[4] Both increased and neutral oscillation (c entirely real) exist and for the neutral ones the wave velocity is equal to the stream velocity at the point of inflection of the velocity profile. From Eq. (1.18) we have

$$w''(y_s) = w_s'' = 0, \qquad w(y_s) = w_s = 2/3 \quad (1.20)$$

Putting $c = w_s$ and Eq. (1.18) into Eq. (1.19) we have

$$\phi'' - \alpha^2\phi + 6b^2\phi \operatorname{sech}^2 by = 0 \quad (1.21)$$

For symmetrical oscillation, the solution of Eq. (1.21) is

$$\phi = k \operatorname{sech} by \tanh by \quad (1.22)$$

where k is an arbitrary constant and the eigenvalue α will be

$$\alpha = \alpha_s = b = 0.27516 \quad (1.23)$$

For antisymmetrical oscillation, the solution of Eq. (1.21) is

$$\phi = k \operatorname{sech}^2 by \quad (1.24)$$

with the eigenvalue

$$\alpha = \alpha_s = 2b = 0.55032 \quad (1.25)$$

Eq. (1.24) was first found by Savic in 1941.[7]

Stability in a Viscous Fluid

Now we are going to study the stability of jet-type flow in a viscous fluid—i.e., for finite Reynolds Number. Here we should deal with the boundary value problems formulated in Eqs. (1.15) and (1.17). We shall find the eigenvalues of α, c, and R. We take α as positive real number; c may be complex. R must be real and positive in order to have some physical significance. As shown before, we treat the symmetrical and the antisymmetrical oscillations separately. Furthermore, α is assumed to be small and αR is large so that all the terms of the order of $0(1/\alpha^2R^2)$ may be neglected.

(*i*) *Symmetrical Disturbance.*—After neglecting the higher order terms, the determinantal Eq. (1.15) becomes

$$F_1(\alpha,c,\alpha R) = \Phi_{2-}{}^{(0)} + \frac{1}{\alpha R}\left[\Phi_{2-}{}^{(1)} - i\left(\frac{w''(0)}{(1-c)^2} + \frac{\alpha^2}{1-c}\right)\Phi_{2-}{}^{(0)}\right] \quad (1.26)$$

If we put c to be real value, the eigenvalue α obtained from Eq. (1.26) in order to get positive real value of R gives the corresponding values for neutral αR curve. In the study of hydrodynamical stability, it is usual to plot the neutral αR curve to show the region of stability. It is interesting to examine the general shape of the neutral αR curves for jet-type flow and determine whether or not they are similar to those of ordinary boundary-layer flow or Poiseuille flow. For ordinary boundary-layer flow or Poiseuille flow, there are two branches of the neutral curve. For the lower branch, one has $\alpha \to 0$ and $R \to \infty$. Let us substitute the relations $\alpha \to 0$ and αR is finite but large in Eq. (1.26) we have

$$\alpha R = i\,\frac{w''(0)}{(1-c)^2} \quad (1.27)$$

Eq. (1.27) represents the characteristic of the flow as $\alpha \to 0$, and $R \to \infty$. Since $w''(0)$ is a real and negative value, for any real value of α and c, R will be purely imaginary. Therefore there will be no lower branch of neutral αR curve in the present case.* For real value of R, we must have complex c. Put

$$c = c_R + ic_i \quad (1.28)$$

into Eq. (1.27), and we have for real value of R

$$(1 - c_R)^2 - c_i^2 = 0 \quad (1.29)$$

$$\alpha R = -[w''(0)]/[2c_i(1 - c_R)] \quad (1.30)$$

If $c_R < 1$, $c_i > 0$, and if $c_R > 1$, $c_i < 0$. Hence for first approximation, the flow is unstable for symmetrical disturbance at very small α when the velocity of propagation of the disturbance is smaller than the maximum velocity in the jet but stable when the velocity of propagation of disturbance is larger than the maximum velocity in the jet. Ordinarily $c_R < 1$. We may conclude that there is no lower branch of neutral αR curve for symmetrical disturbance of jet-type flow and that, as α is sufficiently small and R is large, the jet-type flow is always unstable with respect to symmetrical disturbance.

Next we investigate the effect of viscosity on the neutral stable disturbance in inviscid fluid. If there is an inviscid neutral disturbance with $c = c_s$ and $\alpha = \alpha_s$, we have

$$F_1(\alpha_s, c_s, R = \infty) = 0 \quad (1.31)$$

When $\alpha = \alpha_s$, $c = c_s + \Delta c$, differing but slightly from c_s for finite but large R. We have from Eqs. (1.26) and (1.31) after neglecting the higher order terms

$$\Delta c = -\frac{\Phi_{2-}{}^{(1)}(c_s, \alpha)}{\alpha_s R[\partial\Phi_{2-}{}^{(0)}/\partial c]_{\alpha_s,c_s}} = \Delta c_R + i\Delta c_i \quad (1.32)$$

In Eq. (1.32), for first approximation, we have

$$\Delta c_i = \frac{1}{R}\left[\frac{D_{0i}(B_0' - \alpha_s B_{1R}') + B_{1i}' D_{0R}\alpha_s}{(B_0' - \alpha_s B_{1R}{}^1)^2 + B_{1i}'^2\alpha_s^2}\right]_{c_s} \quad (1.33)$$

$$\Delta c_R = \frac{1}{R}\left[\frac{D_{0R}(B_0' - \alpha_s B_{1R}') - D_{0i}B_{1i}'\alpha_s}{(B_0' - \alpha B_{1R}')^2 + B_{1i}'^2\alpha_s^2}\right]_{c_s} \quad (1.34)$$

From numerical calculations of mean velocity of jet from small slit, it is found that Δc_i is a negative quantity. Hence the viscosity effect is stabilizing. The change in c_R is rather small. It shows the difference of the upper branch of the neutral α_R curve of the jet-type flow from that of the ordinary boundary-layer flow. An inviscid neutral symmetrical disturbance with non-vanishing wave number and phase velocity will be stabilizing by the effect of viscosity in jet-type flow.

For the actual shape of the neutral αR curve we should calculate the eigenvalue α from Eq. (1.26) for various real values of c. First we should evaluate the integrals B_1, D_0, etc. Since there is a singularity at $w = c$, usually it is necessary to perform the integration in complex plane. Chiarulli[9] suggested a method in which the numerical integration along the complex contour may be avoided. We extend his method to perform these integrations.

(*ii*) *Antisymmetrical Disturbance.*—After neglecting the higher order terms, the determinantal Eq. (1.17) becomes

$$F_2(\alpha, c, \alpha R) = \Phi_{1-}{}^{(0)} + \frac{1}{\alpha R}\left[\Phi_{1-}{}^{(1)} - i\,\frac{(1-c)w''(0) + \alpha^2}{(1-c)^3}\,\Phi_{1-}{}^{(0)}\right] = 0 \quad (1.35)$$

First we examine the lower branch of the neutral αR curve and see whether or not it exists. Put $\alpha \to 0$, αR is finite in Eq. (1.35), and we have

$$\alpha R = i\,\{[w''(0)]/(1-c)^2\} - E_0 \quad (1.36)$$

For real values of c from 0 to 1, it is found that R is always complex if α is real. Hence there is no lower branch of this neutral αR curve.*

If we put Eq. (1.28) into Eq. (1.36), we have

$$E_0(c_R + ic_i) = -c_i E_{0R_1} + iE_{0i}$$

* Prof. C. C. Lin pointed out to the author that according to Synge's criteria,[20] the lower branch of the neutral stable curve might still exist for such a low value of αR that the asymptotic solution, Eq. (1.3), no longer holds true. This point should be clarified by further investigation. However, if it were true, then even for moderate Reynolds Number, α of the lower branch neutral curve is so small that it would practically coincide with the R-axis. Hence for first approximation, we may still consider that such a lower branch does not exist.

$$\alpha R = c_i\left[-\frac{2w''(0)\ (1-c_R)}{[(1-c_R)^2-c_i^2]^2+4c_i^2\ (1-c_R)^2}+E_{0R_1}\right]=c_iK \tag{1.37}$$

For $c_R < 1$, it was found that K is always positive. Hence if αR is real and positive, c_i must be positive. As a result the flow is unstable with respect to antisymmetrical disturbance for $\alpha \to 0$ and R is large.

Next we investigate the effect of viscosity on the neutral disturbance in inviscid fluid. If there is an inviscid neutral disturbance with $c = c_s$ and $\alpha = \alpha_s$, we have

$$F_2(c_s,\ \alpha_s,\ R=\infty)=0 \tag{1.38}$$

When $\alpha = \alpha_s$ and $c = c_s + \Delta c$ differing but slightly from c_s for finite but large R, we have from Eqs. (1.35) and (1.38) after nelgecting the higher order terms

$$\Delta c = -\frac{\Phi_{1^-}{}^{(1)}(c_s,\ \alpha_s)}{\alpha_s R[\partial\Phi_{1^-}{}^{(0)}/\partial c]_{\alpha_s,c_s}}=\Delta c_R+i\Delta c_i \tag{1.39}$$

In Eq. (1.39) for first approximation, we have

$$\Delta c_i=\frac{1}{\alpha_s R}\frac{E_{0i}-\alpha_s E_{1i}}{\alpha_s(\partial A_1/\partial c)_{c_s}} \tag{1.40}$$

$$\Delta c_R=\frac{1}{\alpha_s R}\frac{E_{0R}-\alpha_s E_{1R}}{\alpha_s(\partial A_1/\partial c)_{c_s}} \tag{1.41}$$

For mean velocity distribution of jet from small slit it is found that Δc_i is a negative quantity. Hence the effect of viscosity is stabilizing. An inviscid antisymmetrical disturbance with nonvanishing wave number and phase velocity will be also stabilizing by the effect of viscosity in jet-type flow.

Part (II) Jet Flow of Compressible Fluid

Lees-Lin Equations and Their Solutions

The general equations governing one normal mode of the small velocity and temperature disturbances of two-dimensional laminar flows of gas and their solutions are studied in details by Lees and Lin.[15] We are going to use their method to study the stability of the velocity profile of jet-type flow. First we summarize some of their results which are useful for the present analysis and then derive some equations from the general equations which are important for the problem of jet-type flow. In the present analysis, the effect of gravity is neglected, hence all the terms containing the Froude number in Lees-Lin equations are omitted.

The final dimensionless and linearized equations for the amplitudes of small disturbances in a parallel or nearly parallel main flow are as follows:

$$\rho[i(w-c)f+w'\phi]=-\frac{i\pi}{\gamma M^2}+\frac{1}{\alpha R}F_I(Z_i) \tag{2.1}$$

$$\rho[i(w-c)\phi]=-\frac{\pi'}{\gamma\alpha^2M^2}+\frac{1}{\alpha R}F_{II}(Z_i) \tag{2.2}$$

$$i(w-c)r+\rho(\phi'+if)+\rho'\phi=0 \tag{2.3}$$

$$\rho[i(w-c)\theta+T'\phi]=-(\gamma-1)\times$$

$$\rho T(\phi'+if)+(1/\alpha R)F_{III}(Z_i) \tag{2.4}$$

$$\pi/p=(r/\rho)+(\theta/T) \tag{2.5}$$

where the nondimensional disturbance variables are defined as follows:

u' = x-wise perturbation velocity component =

$$f(y)e^{i\alpha(x-ct)} \tag{2.6}$$

v' = y-wise perturbation velocity component =

$$\alpha\phi(y)e^{i\alpha(x-ct)} \tag{2.7}$$

$$\text{perturbation density} = r(y)e^{i\alpha(x-ct)} \tag{2.8}$$

$$\text{perturbation pressure} = \pi(y)e^{i\alpha(x-ct)} \tag{2.9}$$

$$\text{perturbation temperature} = \theta(y)e^{i\alpha(x-ct)} \tag{2.10}$$

$F_I(Z_i)$, $F_{II}(Z_i)$ and $F_{III}(Z_i)$ are linear combinations of the perturbation variables Z_i—i.e., f, ϕ, r, π, θ, and their first derivatives with respect to y.

The system of five equations, Eqs. (2.1) to (2.5), is actually equivalent to six homogeneous linear differential equations of the first order and there are six linearly independent solutions. The system of equations can be solved by the method of successive approximation by means of asymptotic series. Two asymptotic series are obtained by expanding the solution in powers of $(\alpha R)^{-1}$—i.e.,

$$Z_i=Z_i^{(0)}+(\alpha R)^{-1}Z_i^{(1)}+(\alpha R)^{-2}Z_i^{(2)}+\ldots \tag{2.11}$$

The system of Eq. (2.1) to (2.5) may be written as a differential equation for each of the independent variables. For example, the differential equation of the amplitude of velocity component v'—i.e., ϕ will be

$$\frac{d}{dy}\left[\frac{(w-c)\phi'-w'\phi}{T-M^2(w-c)^2}\right]-\frac{\alpha^2(w-c)\phi}{T}=\frac{1}{\alpha R}G(Z_i) \tag{2.12}$$

where $G(Z_i)$ is a linear combination of Z_i and their first derivatives.

Substituting Eq. (2.11) into Eq. (2.12) we have

$$\frac{d}{dy}\left[\frac{(w-c)\phi^{(0)\prime}-w'\phi^{(0)}}{T-M^2(w-c)^2}\right]=\frac{\alpha^2(w-c)\phi^{(0)}}{T} \tag{2.13}$$

$$\frac{d}{dy}\left[\frac{(w-c)\phi^{(n)}-w'\phi^{(n)}}{T-M^2(w-c)^2}\right]-\frac{\alpha^2(w-c)\phi^{(n)}}{T}=$$

$$G_0(Z_i^{(n-1)})+\alpha^2G_i(Z_1^{(n-1)})+\alpha^4G_2(Z_i^{(n-1)})\quad(n\geqq 1) \tag{2.14}$$

where G_i is independent of α and R, and is a linear combination of $Z_i^{(n-1)}$ and its first derivatives.

As soon as ϕ is obtained, the other perturbation variables can be calculated from the following equations:

$$f = -i\frac{M^2(w-c)w'\phi - T\phi'}{T - M^2(w-c)^2} + \frac{i}{\alpha R}\left[\frac{M^2(w-c)F_I}{\rho} - \frac{F_{III}}{\gamma p(w-c)}\right] \quad (2.15)$$

$$r = i[\rho(\phi' + if) + \rho'\phi]/(w-c) \quad (2.16)$$

$$\pi = i\gamma M^2\{\rho[i(w-c)f + w'\phi] - (1/\alpha R)F_I\} \quad (2.17)$$

$$\theta = T[(\pi/\rho) - (r/\rho)] \quad (2.18)$$

Similar to the incompressible case, Eq. (2.12) can be solved by developing $\phi^{(0)}$ in power of α^2—i.e.,

$$\phi_1^{(0)} = (w-c)[h_0(y) + \alpha^2 h_2(y) + \alpha^4 h_4(y) + \ldots] \quad (2.19)$$

$$\phi_2^{(0)} = (w-c)[k_1(y) + \alpha^2 k_3(y) + \alpha^4 k_5(y) + \ldots] \quad (2.20)$$

where $h_0 = 1$, h_{2n} and k_{2n+1} are functions of w, c, M^2, and T which are given in reference 15.

For the $\phi^{(1)}$ solutions we have

$$\phi_1^{(1)} = (w-c)[p_0(y) + \alpha^2 p_2(y) + \alpha^4 p_4(y) + \ldots] \quad (2.21)$$

$$\phi_2^{(1)} = (w-c)[q_1(y) + \alpha^2 q_3(y) + \alpha^4 q_5(y) + \ldots] \quad (2.22)$$

where p_{2n} and q_{2n+1} are functions of w, c, M^2, and T which are given in Appendix A.

Four other asymptotic solutions are obtained by putting

$$Z_i = f_i \exp\left[(\alpha R)^{1/2}\int g\, dy\right] \quad (2.23)$$

where g is independent of αR. For a similar reason as in the incompressible fluid case, these solutions should be rejected in the study of stability of jet type flow.

Finally we have

$$\phi = c_1\phi_1 + c_2\phi_2 \quad (2.24)$$

Asymptotic Behavior of the Solution at Infinity

We are going to investigate the behavior of $\phi^{(j)}$ for large values of y. By similar procedure as that for incompressible case, we find the following expressions of $\phi_k^{(0)}$ and $\phi_k^{(1)}$ for large negative y.

At $y \to -\infty$, we assume that

$$w(y = -\infty) = a, \quad T(y = -\infty) = T_a$$

Then for large y

$$\phi_k^{(j)} = \Phi_{k+}^{(j)}e^{\alpha z} + \Phi_{k-}^{(j)}e^{-\alpha z} \quad (2.25)$$

$$(j = 0, 1 \text{ and } k = 1, 2)$$

where

$$z = \Omega y = \{1 - [M^2(a-c)^2/T_a]\}^{1/2}y \quad (2.26)$$

and the expressions of $\Phi_{k\pm}^{(j)}$ may be written in the same form as those given in Eqs. (1.10) to (1.13) except that the expressions of A_n, B_n, E_n, and D_n are different. These expressions for compressible fluid are given in Appendix B.

Similar expressions for $\phi^{(j)}$ can be obtained for $y \to +\infty$ and $w \to a$, $T \to T_a$.

Subsonic, Sonic, and Supersonic Disturbances

It is convenient in the study of the stability of flow of compressible fluid to classify the disturbance as "subsonic," "sonic," and "supersonic" relative to certain local velocity u^* when the x-component of the phase velocity of the disturbance relative to the local velocity is less than, equal to, or greater than, the mean speed of sound at that point. The conditions for this classification are

$$T \begin{cases} < \\ = \\ > \end{cases} M^2(w - c_R)^2 \quad \begin{cases} \text{supersonic} \\ \text{sonic} \\ \text{subsonic} \end{cases} \quad (2.27)$$

If $w = a$, $T = T_a$, the subsonic disturbance relative to $w = a$ must satisfy the following inequality

$$a - (T_a/M^2)^{1/2} < c_R < a + (T_a/M^2)^{1/2} \quad (2.28)$$

For the case of no energy transfer—i.e., the relation between the temperature and velocity is given below

$$T_a + [(\gamma - 1)/2]M^2a^2 = 1 + [(\gamma - 1)/2]M^2 \quad (2.29)$$

Eq. (2.28) becomes

$$a - \left[\frac{1}{M^2} + \frac{\gamma - 1}{2}(1 - a^2)\right]^{1/2} < c_R < a + \left[\frac{1}{M^2} + \frac{\gamma - 1}{2}(1 - a^2)\right]^{1/2} \quad (2.30)$$

a may vary from 0 to 1. The limiting curves of Eq. (2.30) are plotted in Fig. 1, which shows the region of the classification of the disturbances relative to local velocity. It is interesting to see that no disturbance may be considered as subsonic relative to the entire flow field if the maximum Mach Number of the flow field is greater than 2.5 for the case of no energy transfer.

Ω^2 will be greater than, equal to, or less than zero according to whether the disturbance is subsonic, sonic, or supersonic with respect to the velocity a at infinity. Since the value of Ω^2 determines the nature of the solutions of the disturbance differential equation we must study its value in detail. For subsonic disturbance relative to the velocity at infinity, the amplitude of the disturbance will die out rapidly with distance from the axis of the jet and discrete eigenvalues may be found. The neutral subsonic disturbance is an "eigen-oscillation" in the jet. These disturbances are important in the study of stability of jet flow of compressible fluid and determine the limits of stability of the jet. For supersonic disturbance relative to velocity at infinity, Ω is imaginary, the eigenvalues are continuous and not discrete. For disturbances of this type the wave length and phase velocity are completely arbitrary because the boundary condition at infinity is missing here. These disturbances behave as progressive sound waves

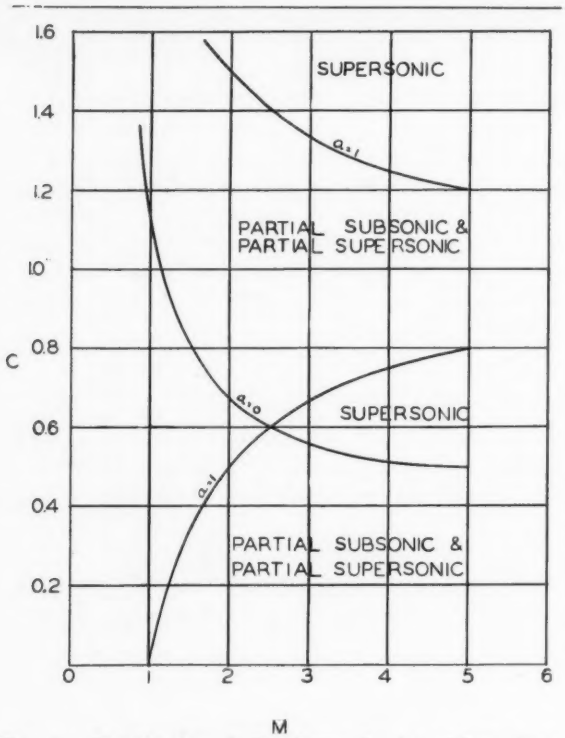

FIG. 1. Classification of disturbance for jet without heat transfer.

in the jet and they have no significance for the stability of the jet.

For jet with the surrounding stream at rest, i.e., $a = 0$, the line $a = 0$ in Fig. 1 separates the subsonic disturbance and the supersonic disturbance for the case without energy transfer. Any disturbance with

$$c_R > \{(1/M^2) + [(\gamma - 1)/2]\}^{1/2} \tag{2.31}$$

should be regarded as supersonic disturbance.

In this paper we are concerned with only the subsonic disturbance relative to the velocity at infinity. For the case with surrounding stream at rest, the physical condition for subsonic disturbance for the case of no energy transfer is

$$c_R < \{(1/M^2) + [(\gamma - 1)/2]\}^{1/2} \tag{2.32}$$

In general, only those disturbances satisfying the condition of Eq. (2.28) are considered in the present paper.

Boundary Value Problems

Similar to the incompressible fluid case, we treat the symmetrical and the antisymmetrical disturbances separately.

(*i*) *Symmetrical Disturbance.*—Here the boundary conditions are

$$\phi(-\infty) = \phi(0) = 0 \tag{2.33}$$

The determinantal equation is then

$$F_1(\alpha, c, R, M^2) = \begin{vmatrix} \phi_1(-\infty) & \phi_2(-\infty) \\ \phi_1(0) & \phi_2(0) \end{vmatrix} = 0 \tag{2.34}$$

(*ii*) *Antisymmetrical Disturbance.*—Here the boundary conditions are

$$\phi(-\infty) = \phi'(0) = 0 \tag{2.35}$$

The determinantal equation is then

$$F_2(\alpha, c, R, M^2) = \begin{vmatrix} \phi_1(-\infty) & \phi_2(-\infty) \\ \phi_1'(0) & \phi_2'(0) \end{vmatrix} = 0 \tag{2.36}$$

Velocity and Temperature Distribution of the Main Flow

The velocity and the temperature distributions of the main flow can be calculated either by the method given by the author in reference 17 with the assumption of Prandtl's Number to be unity or by the following stepwise numerical integration method.

In terms of stream function ψ and x-wise distance, the equations of motion without pressure gradient of the two-dimensional jet flow and the equations of continuity give the following nondimensional equation

$$\frac{\partial w_0}{\partial x_0} = \frac{\partial}{\partial \psi_0}\left(\rho_0 \mu_0 w_0 \frac{\partial w_0}{\partial \psi_0}\right) \tag{2.37}$$

The nondimensional energy equation will be

$$\frac{\partial c_p T_0}{\partial x_0} = \frac{\partial}{\partial \psi_0}\left(\lambda_0 \rho_0 w_0 \frac{\partial T}{\partial \psi_0}\right) + \mu_0 \rho_0 w_0 \left(\frac{\partial w_0}{\partial \psi_0}\right)^2 \tag{2.38}$$

and the initial conditions are

$$x_0 = 0, \quad T_0 = T_0(\psi_0), \quad w_0 = w_0(\psi_0) \tag{2.39}$$

The equation of state

$$\rho_0 = T_0 \tag{2.40}$$

and the law of variation of viscosity is

$$\mu_0 = \mu_0(T_0) \tag{2.41}$$

where the nondimensional quantities—i.e., temperature T_0, velocity w_0, etc., are in terms of certain *constant* quantities at $x_0 = 0$.

Eqs. (2.37) and (2.38) can be integrated numerically by stepwise finite difference method starting from the initial conditions, Eq. (2.39), with the help of Eqs. (2.40) and (2.41). Any law of variation of viscosity may be used in this integration without introducing any complication.

Stability in an Inviscid Fluid

(*i*) *The Differential Equation of Disturbances.*—In the limit of infinite Reynolds Number, the differential equation of ϕ becomes

$$\phi'' - \frac{T' - 2M^2(w-c)w'}{T - M^2(w-c)^2}\phi' + \left[\frac{\dfrac{T' - 2M^2(w-c)w'}{T - M^2(w-c)^2}w' - w''}{w-c} - \frac{\alpha^2}{T}\{T - M^2(w-c)^2\}\right] = 0 \quad (2.42)$$

In order to remove the singular point $w = c$ for neutral stable disturbance, we must have

$$T_{c_s}'w_{c_s}' = w_{c_s}''T_{c_s} \quad (2.43)$$

where $T_{c_s} = T(w = c_s)$, etc., and c_s is the velocity of propagation of the neutral stable disturbance in the inviscid fluid. For given velocity and temperature distributions of the main flow Eq. (2.43) determines the velocity of propagation of neutral stable disturbances, both symmetrical and antisymmetrical, in the inviscid fluid. In case of incompressible fluid $T_{c_s}' = 0$, $T_{c_s} =$ constant, hence the condition reduces to

$$w_{c_s}'' = 0 \quad (2.44)$$

It is interesting to note that if Eq. (2.43) is satisfied the imaginary parts of A_n's and B_n's are all equal to zero, provided that Ω is a real number—i.e., for subsonic disturbances relative to the surrounding stream.

For a given velocity distribution as Mach Number M increases, Ω^2 decreases. If M is large enough such that for $c = c_s$, $\Omega^2 < 0$, there will be no subsonic neutral stable disturbance relative to the surrounding stream possible in the jet flow. The flow is then stable with respect to small disturbance for such large Mach Number.

(*ii*) *Symmetrical Disturbance.*—The determinantal equation for this case reduces to

$$\Phi_{2-}{}^{(0)} = -(B_0/\alpha) + B_1 - B_2\alpha + \ldots = 0 \quad (2.45)$$

$B_0 = T_a\Omega/c_s^2$ is real for subsonic disturbance in the jet relative to the velocity of the surrounding stream. If we put $c = c_s$ determined by Eq. (2.43) into Eq. (2.45) all the imaginary parts of B_n are identical to zero; hence we have

$$B_0(c_s) - \alpha_s\beta_{1R}(c_s) + \alpha_s^2B_{2R}(c_s) - \ldots = 0 \quad (2.46)$$

Eq. (2.46) determines the wave number α_s for the neutral stable disturbance which can be solved by successive approximation.

We see that as Mach Number M increases both $\Omega(c_s)$ and α_s decrease. If M is equal to the critical value

$$M_{CR} = \sqrt{T_a/c_s^2} \quad (2.47)$$

$\alpha_s = 0$. As we shall show later $\alpha > \alpha_s$, the disturbance is stable. Hence $M > M_{CR}$, the jet-type flow will be stable with respect to all small symmetrical disturbances in the inviscid fluid.

For the case of no energy transfer, the critical number is about 2.5.

If we vary α slightly from α_s, in order to satisfy Eq. (2.45), c must be different slightly from c_s. Put

$$\alpha = \alpha_s + \Delta\alpha, \qquad c = c_s + \Delta c = c_s + \Delta c_R + i\Delta c_I \quad (2.48)$$

where $\Delta\alpha$ is a real number and Δc may be complex. Substituting Eq. (2.48) into Eq. (2.45) and neglecting the higher order terms we have

$$\Delta\alpha = \frac{\Delta c_I}{\alpha\,[\partial B_1(c_s)/\partial c]_I B_{1R}(c_s)} \times \left[\left(\frac{\partial B_0}{\partial c} - \alpha_s\frac{\partial B_{1R}}{\partial c}\right)^2 + \left(\alpha_s\frac{\partial B_{1I}}{\partial c}\right)^2\right]_{c_s} \quad (2.49)$$

where $B_{1R}(c_s)$ is a positive real number

$$[\partial B_1(c_s)/\partial c]_I = -\pi(T_{c_s}''/w_{c_s}'^3) \quad (2.50)$$

Both T_{c_s}'' and $w_c'^3$ are positive. Hence, $\{[\partial B_1(c_s)]/\partial c\}_I$ is a negative number. Hence, from Eq. (2.49) we see that $\Delta\alpha$ and Δc_I have opposite signs.

As we vary α from α_s if $\alpha < \alpha_s$, c_I being positive, the flow will be unstable with respect to such a disturbance; while $\alpha > \alpha_s$, c being negative, the flow will be stable with respect to such a disturbance. Hence when the Mach Number is large enough such that $\alpha_s = 0$, the jet flow will be stable with respect to all small symmetrical disturbances.

(*iii*) *Antisymmetrical Disturbances.*—The determinantal equation for this case reduces to

$$\Phi_{1-}{}^{(0)} = A_0 - \alpha A_1 + \alpha^2A_2 - \ldots = 0 \quad (2.51)$$

where $A_0 = 1$. For subsonic disturbance relative to the velocity of the surrounding stream, A_1 is a positive real number and

$$A_n = A_{nR} + iA_{nI} \qquad (n \geqq 2)$$

If we put $c = c_s$ given by Eq. (2.43), all the A_{nI} vanish, and we have

$$\Phi_{1-}{}^{(0)} = 1 - \alpha_sA_1(c_s) + \alpha_s^2A_{2R}(c_s) - \ldots = 0 \quad (2.52)$$

Eq. (2.52) determines the wave number α_s for the neutral stable antisymmetrical disturbance. For a low Mach Number case, A_1 is in general larger than A_{2R}; for first approximation

$$\alpha_s = \frac{1}{A_1(c_s)} = \frac{c_s^2}{\Omega T_a}\frac{1}{\displaystyle\int_{-\infty}^{0}\{(c_s^2/T_a) - [(w-c_s)^2/T]\}\,dy} \quad (2.53)$$

Here we find that for low subsonic main flow $M < 1$, α_s for antisymmetrical disturbance in general increases with the Mach Number if the effect of energy transfer is small. Hence, for low subsonic flow with small energy transfer, the increase of flow velocity has a destabilizing effect on the flow. As M increases near the critical value M_{cR}, A_1 approaches to zero, and Eq. (2.54) will no longer be a correct approximation for α_s. The most suitable approximation will then be

$$\alpha_s = (A_1 - \sqrt{A_1^2 - 4A_{2R}})/2A_{2R} \qquad (2.54)$$

and as $A_1 \to 0$

$$\alpha_s \to 1/\sqrt{-A_{2R}} \qquad (2.55)$$

As Mach Number M is larger than M_{cR} there will be no discrete eigenvalue α_s, and all neutral disturbances will be supersonic disturbance. The flow is believed to be stable though it is not possible to show this as clearly as in the case of symmetrical disturbance.

If we vary α slightly from α_s in order to satisfy Eq. (2.52), c must be different slightly from c_s. Put Eq. (2.48) into Eq. (2.52), and, neglecting the higher order terms, we have

$$\Delta\alpha = \Delta c_i \frac{\left[\alpha_s\left(\frac{\partial A_2}{\partial c}\right)_i - \frac{\partial A_1}{\partial c}\right]_{c_s}^2 + \left[\alpha_s\left(\frac{\partial A_2}{\partial c}\right)_R\right]_{c_s}^2}{\frac{1}{\alpha_s}\left(\frac{\partial A_2}{\partial c}\right)_i [\alpha_s^2 A_{2R}(c_s) - 1]} \qquad (2.56)$$

$(\partial A_2/\partial c)_i$ is in general positive, A_{2R} is a negative number. Hence, $\Delta\alpha$ and Δc have oppositive signs. Hence, the disturbance $\alpha > \alpha_s$ is damped, and $\alpha < \alpha_s$ is self-excited.

Stability in a Viscous Fluid

(*i*) *General Considerations.*—In the case of incompressible fluid, we found that the viscosity has a stabilizing effect on the disturbance in inviscid fluid. Since the solutions of stability equation of compressible fluid are similar to those of incompressible fluid, it is believed that the study of stability of inviscid fluid is sufficient for jet-type flow, and hence the computations for viscous fluid are not carried out. Of course it would be interesting if such computations were carried out. Such computations are much more complicated, for the stability calculations must be performed for each value of Mach Number and of each condition of heat transfer. In the following we summarize the determinantal equations for the viscous fluid. The results of numerical calculations will be reported later.

(*ii*) *Determinantal Equations.*—The determinantal equation for symmetrical disturbance is

$$\Phi_{2-}^{(0)} + (1/\alpha R)\Phi_{2-}^{(1)} = 0 \qquad (2.57)$$

The determinantal equation for antisymmetrical disturbance is

$$\Phi_{1-}^{(0)} + \frac{1}{\alpha R}(i\Phi_{1-}^{(0)}\{[1 + M^2(1-c)^2]F_A(0) + F_B(0)\} + \Phi_{1-}^{(1)}) = 0 \qquad (2.58)$$

where $F_A(0)$ and $F_B(0)$ are the values of F_A and F_B at $y = 0$, respectively.

$$F_A = \mu_1\left[\frac{w''T}{(1-c)^2} - w''M^2 + \frac{T''}{1-c}\right] - (\gamma - 1)M^2T\frac{d\mu_1}{dT}w''$$

$$F_B = (\gamma/\sigma_0)\,[-\mu_1(\gamma-1)M^2T'' + 2\mu_1(\rho''/\rho) \times \{[T/(1-c)^2] - M^2\} - (\gamma-1)M^2T(d\mu_1/dT)T''] \qquad (2.59)$$

Conclusions

From the method of small perturbation, the following conclusions may be drawn for the stability of two-dimensional laminar jet-type flow of gas:

(A) For incompressible fluid, we have that

(1) Both the symmetrical and the antisymmetrical disturbances are unstable for large Reynolds Numbers but the region of instability of symmetrical disturbances lies inside that of an antisymmetrical one.

(2) The effect of viscosity on the neutral stable disturbance in inviscid fluid is always stabilizing for jet-type flow.

(3) When the wave number is very small and Reynolds Number is large, the jet flow is always unstable.

(B) For compressible fluid we have that

(1) The solutions of compressible fluid are similar to those of incompressible fluid.

(2) So far as laminar stability is concerned an important difference exists between the case of supersonic and subsonic disturbances relative to the velocity of the surrounding stream of the jet. For subsonic disturbance, discrete eigenvalues may be found and the limit of stability can be determined. For supersonic disturbance the eigenvalues are continuous and not discrete; no limit of stability can be found. Usually it is assumed that supersonic disturbances have no significance for the stability problem. But further research must be made to clarify this point.

(3) For inviscid compressible fluid

(a) Increase of Mach Number has stabilizing effect on the symmetrical disturbances. When Mach Number reaches the critical value, the jet-type flow will be completely stable with respect to small symmetrical disturbances.

(b) When Mach Number is sufficiently small, increase of Mach Number has a destabilizing effect on the antisymmetrical disturbance. But as Mach Number is sufficiently high, the wave number of neutral stable antisymmetrical disturbance increases

with Mach Number toward a limit. If the Mach Number is larger than the critical value, no discrete value of wave number of neutral disturbance could be found.

Appendix A

Functions p_{2n} and q_{2n+1} for Compressible Fluid Case

The functions F_I, F_{II}, and F_{III} of Eqs. (2.1), (2.2), and (2.4) may be written as follows[15]

$$F_I = F_{11} + \alpha^2 F_{12} \tag{A.1}$$

$$F_{II} = \alpha F_{21} + \alpha^3 F_{22} \tag{A.2}$$

$$F_{III} = F_{31} + \alpha^2 F_{32} \tag{A.3}$$

where the expressions of F_{ij} are given in reference 15, pages 13–14 (except term $-(r/\rho)(\mu_1' w' + \mu_1 w'')$ in F_{11} is missing there, which should be added).

$$p_0 = -\int_y^{y_0} \left[\frac{T}{(w-c)^2} - M^2\right]\{[1 + M^2(w-c)^2]F_{110} + F_{310}\}\, dy \tag{A.4}$$

$$p_2 = -\int_y^{y_0} \left[\frac{T}{(w-c)^2} - M^2\right]\{[1 + M^2(w-c)^2]\,[F_{112} + F_{120}] + F_{320}\}\, dy + i\int_y^{y_0} \left[\frac{T}{(w-c)^2} - M^2\right]\times dy \int_y^{y_0} F_{210}\, dy + \int_y^{y_0} \left[\frac{T}{(w-c)^2} - M^2\right] dy \int_y^{y_0} \frac{(w-c)^2 p_0}{T}\, dy \tag{A.5}$$

$n \geqq 0$

$$p_{2n+4} = -\int_y^{y_0} \left[\frac{T}{(w-c)^2} - M^2\right]\{[1 + M^2(w-c)^2][F_{11(2n+4)} + F_{12(2n+2)}] + F_{31(2n+4)}\, F_{32(2n+2)}\}\, dy + i\int_y^{y_0}\left[\frac{T}{(w-c)^2} - M^2\right] dy \int_y^{y_0} [F_{21(2n+2)} + F_{22(2n)}]dy + \int_y^{y_0} \left[\frac{T}{(w-c)^2} - M^2\right]dy \int_y^{y_0} \frac{(w-c)^2}{T} p_{2n+2}\, dy \tag{A.6}$$

where $F_{ij(2n)} = F_{ij}$ with $\phi = (w-c)h_{2n}$ and f, r, π, θ calculated from this ϕ from Eqs. (2.15) to (2.18)

$$q_1 = -\int_y^{y_0} \left[\frac{T}{(w-c)^2} - M^2\right]\{[1 + M^2(w-c)^2]F_{111} + F_{311}\}\, dy \tag{A.7}$$

$$q_3 = -\int_y^{y_0} \left[\frac{T}{(w-c)^2} - M^2\right]\{[1 + M^2(w-c)^2]\,[F_{113} + F_{121}] + F_{313} + F_{321}\}\, dy + \int_y^{y_0} \left[\frac{T}{(w-c)^2} - M^2\right]\times dy \int_y^{y_0} F_{211}\, dy + \int_y^{y_0} \left[\frac{T}{(w-c)^2} - M^2\right] dy \int_y^{y_0} \frac{(w-c)^2 q_1}{T}\, dy \tag{A.8}$$

$n \geqq 0$

$$q_{2n+5} = -\int_y^{y_0} \left[\frac{T}{(w-c)^2} - M^2\right]\{[1 + M^2(w-c)^2][F_{11(2n+5)} + F_{12(2n+3)}] + F_{31(2n+5)} + F_{32(2n+3)}\}\, dy + i\int_y^{y_0} \left[\frac{T}{(w-c)^2} - M^2\right] dy \int_y^{y_0} [F_{21(2n+3)} + F_{22(2n+1)}]\, dy + \int_y^{y_0} \left[\frac{T}{(w-c)^2} - M^2\right]dy \int_y^{y_0} \frac{(w-c)^2}{T}\, q_{2n+3}\, dy \tag{A.9}$$

where $F_{ij(2n+1)} = F_{ij}$ with $\phi = (w-c)k_{2n+1}$ and corresponding values of f, r, π, θ obtained from this ϕ from eqs. (2.15) to (2.18).

Appendix B

Definite Integrals in Asymptotic Expressions of ϕ^j of Compressible Fluid Case

$$A_0 = 1 \tag{B.1}$$

$$A_1 = -\frac{\Omega T_a}{(a-c)^2}\int_{-\infty}^{y_0} \left\{\frac{(w-c)^2}{T} - \frac{(a-c)^2}{T_a}\right\} dy - z_0 \tag{B.2}$$

$$A_2 = \int_{-\infty}^{y_0} [T - M^2(w-c)^2]\left[\frac{1}{(w-c)^2} - \frac{1}{(a-c)^2}\right]dy \int_{y}^{y_0} \frac{(w-c)^2}{T}\,dy - \frac{1}{(a-c)^2} \times$$

$$\int_{-\infty}^{y_0} \{[T - M^2(w-c)^2] - [T_a - M^2(a-c)^2]\}\,dy \int_{y}^{y_0} \frac{(w-c)^2}{T}\,dy - \frac{\Omega^2 T_a}{(a-c)^2}\int_{-\infty}^{y_0} dy \times$$

$$\int_{-\infty}^{y} \left\{\frac{(w-c)^2}{T} - \frac{(a-c)^2}{T_a}\right\}dy - \left[A_0\frac{z_0^2}{2!} + A_1 z_0\right] \quad \text{(B.3)}$$

where

$$z_0 = \Omega y_0$$

$$B_0 = \frac{T_a \Omega}{(a-c)^2} \quad \text{(B.4)}$$

$$B_1 = -\int_{-\infty}^{y_0} [T - M^2(w-c)^2]\left[\frac{1}{(w-c)^2} - \frac{1}{(a-c)^2}\right]dy - \frac{1}{(a-c)^2}\int_{-\infty}^{y_0} \{[T - M^2(w-c)^2] -$$

$$[T_a - M^2(a-c)^2]\}\,dy - B_0 z_0 \quad \text{(B.5)}$$

$$E_0 = -\int_{-\infty}^{y_0}\left[\frac{T}{(w-c)^2} - M^2\right]\{[1 + M^2(w-c)^2]F_{110} + F_{310}\}\,dy \quad \text{(B.6)}$$

$$E_1 = -\frac{T_a\Omega}{(a-c)^2}\int_{-\infty}^{y_0} F_{210}\,dy - \frac{T_a\Omega}{(a-c)^2}\int_{-\infty}^{y_0} p_0\left[\frac{(w-c)^2}{T} - \frac{(a-c)^2}{T_a}\right]dy - \Omega^2 T_a \int_{-\infty}^{y_0} (p_0 - E_0)\,dy - E_0 t_0 \quad \text{(B.7)}$$

$$D_0 = -\int_{-\infty}^{y_0}\left[\frac{T}{(w-c)^2} - M^2\right]\{[1 + M^2(w-c)^2]F_{111} + F_{311}\}\,dy \quad \text{(B.8)}$$

References

[1] Tietjens, O., *Beitraege zum Turbulenzproblem*, Zeits. angew. Math. Mech., Vol. 5, pp. 200–217, 1925.

[2] Heisenberg, W., *Ueber Stabilitaet und Turbulenz von Fluessigkeitsstroemen*, Ann. Phys., Vol. 74, pp. 577–627, 1924.

[3] Tollmien, W., *Ueber die Entstehung der Turbulenz*, Nachr. Ges., Wiss., Goettingen, Math-Phys. Klasse, pp. 21–44 (1929). Translated by N.A.C.A., N.A.C.A. T.M. No. 609, March, 1931.

[4] Tollmien, W., *Ein allgemeines Kriterium der Instabilitaet laminarer Geschwindigkeitsverteilungen*, Nachr. Ges. Wiss., Goettingen, Math-Phys. Klasse, pp. 79–114, 1935. Translated by N.A.C.A., N.A.C.A. T.M. No. 792, April, 1936.

[5] Schubauer, G. B., and Skramstad, H. K., *Laminar Boundary-Layer Oscillations and Transition on a Flat Plate*, N.A.C.A. W-8, ACR, April, 1943.

[6] Hollingdale, S. H., *Stability and Configuration of the Wakes Produced by Solid Bodies Moving Through Fluids*, Phil. Mag., Vol. 7, No. 29, pp. 209–257, 1940.

[7] Savic, P., *On Acoustically Effective Vortex Motion in Gaseous Jets*, Phil. Mag., Vol. 7, No. 32, pp. 245–252, 1941.

[8] Lessen, M., *On the Stability of the Laminar Boundary Layer Between Parallel Streams*, N.A.C.A. T.N. No. 1929, 1949.

[9] Chiarulli, P., *Stability of Two-Dimensional Velocity Distribution of the Half Jet Type*, Monograph VI, Supplement 1, U.S. Air Force, Technical Report No. F-TS-1228-IA, 1949.

[10] Lin, C. C., *On the Stability of Two-Dimensional Parallel Flows*, Quarterly Appl. Math., Vol. 3, pp. 117–142, 218–234, 277–301, 1945–1946.

[11] Lees, L., *The Stability of the Laminar Boundary Layer in a Compressible Fluid*, N.A.C.A. T.N. No. 1360, July, 1947.

[12] Landau, L., *Stability of Tangential Discontinuities in Compressible Fluid*, Akademiia Nauk S.S.S.R., Comptes rendus (Doklady), Vol. 44, No. 4, pp. 139–141, 1944.

[13] Hiroshi, Hatanaka, *On the Stability of a Surface of Discontinuity in a Compressible Fluid*, Journal Soc. Sci. Culture, Japan, Vol. 2, pp. 3–7, 1947; Appl. Mech. Rev., July, 1949.

[14] Squire, H. B., *On the Stability for Three-Dimensional Disturbances of Viscous Fluid Flow Between Parallel Walls*, Proc. Roy. Soc. London, Series A, No. 142, pp. 621–628, 1933.

[15] Lees, L., and Lin, C. C., *Investigation of the Stability of the Laminar Boundary Layer in Compressible Fluid*, N.A.C.A. T.N. No. 1115, September, 1946.

[16] Foote, J. G., and Lin, C. C., *Some Recent Investigations in the Theory of Hydrodynamic Stability*, Quarterly of Applied Mathematics, Vol. VIII, pp. 265–280, October, 1950.

[17] Pai, S. I., *Two-Dimensional Jet Mixing of a Compressible Fluid*, Journal of the Aeronautical Sciences, Vol. 16, No. 8, pp. 463–469, August, 1949.

[18] Schlichting, H. *Laminar Strahlausbreitung*, ZAMM, Vol. 13, p. 260, 1933.

[19] Bickley, W., *The Plane Jet*, Phil. Mag., Vol. 7, No. 23, p. 156, p. 727 (1937).

[20] Synge, J. L., *Hydrodynamical Stability*, Semicentennial publications of the Amer. Math. Soc., Vol. 2, pp. 227–269, 1938.

Interrelationship Between Boundary Layer and Base Pressure

H. H. KURZWEG*

U.S. Naval Ordnance Laboratory

SUMMARY

Experiments conducted in supersonic wind tunnels during the past 3 years (N.A.C.A. and N.O.L.) show that the pressure at the base of bodies is essentially a function of parameters that govern the boundary layer. Hence, the base pressure is closely connected to surface friction and heat-transfer phenomena.

Experimental results obtained in the N.O.L. supersonic wind tunnels in a Mach range 1.5–5.0 on cylindrical bodies with and without boat-tails with conical heads under various systematic mechanical and thermodynamical variations of the boundary layer are presented and compared with theoretical results.

INTRODUCTION

THE INVESTIGATIONS CARRIED OUT during the past years in supersonic wind tunnels and in free flight concerning the under pressure at the blunt or flat base of missiles and projectiles led to the conclusion that base pressure and boundary layer are closely interrelated. The present importance and status of the base-pressure problem can best be explained by answering the following two questions: (a) What do we expect from base-pressure investigations, and (b) how far can available base-pressure data be used by missile and projectile designers?

The base drag caused by the base pressure is relatively small with respect to the total drag when the aerodynamic shape of the body is plump and its nose is blunt. It is, however, of the same order of magnitude as wave and friction drag when the bodies are sharp-pointed and slender. Long-range projectiles and missiles must have these last features. In spite of the favorable shape, the total drag of large guided missiles can amount to several thousand pounds, of which the contribution of the base drag is then of the order of 1,000 or 2,000 lbs.!

This is a heavy factor in the performance, trajectory, and power-supply calculations. It would be helpful, therefore, for the design engineer to have some formulas, or at least some reliable test data, relating to a number of basic bodies with the necessary directions for the application on a particular missile.

In order to get such information, the Naval Ordnance Laboratory (N.O.L.) carried out systematic base-pressure measurements on cone-cylinder bodies of 5-cm. diameter in the 40- by 40-cm. Aeroballistics Tunnel over a Mach Number range between 1.5 and 5.0 inclusive, as well as in its Pressurized Ballistics Range with 30-caliber projectiles up to Mach Number 3.5 over a pressure range between 3 and 120 in. Hg.

The various phases of these investigations are described in the following paragraphs.

THE BASE PRESSURE AS FUNCTION OF MACH NUMBER

In supersonic flow the dependence of the base pressure on Mach Number (M) seemed to be of principal interest. As a matter of fact, all early base-pressure studies were made with the Mach Number as the only variable.

If the available base-pressure data from Ames Aeronautical Laboratory, National Advisory Committee for Aeronautics (A.A.L.-N.A.C.A.),[1] N.O.L.,[2] Applied Physics Laboratory, The Johns Hopkins University (A.P.L.-J.H.U.),[3] and Ballistics Research Laboratories (B.R.L.)[4] are plotted versus Mach Number, the chart on Fig. 1 is obtained. It can be seen that for each Mach Number a

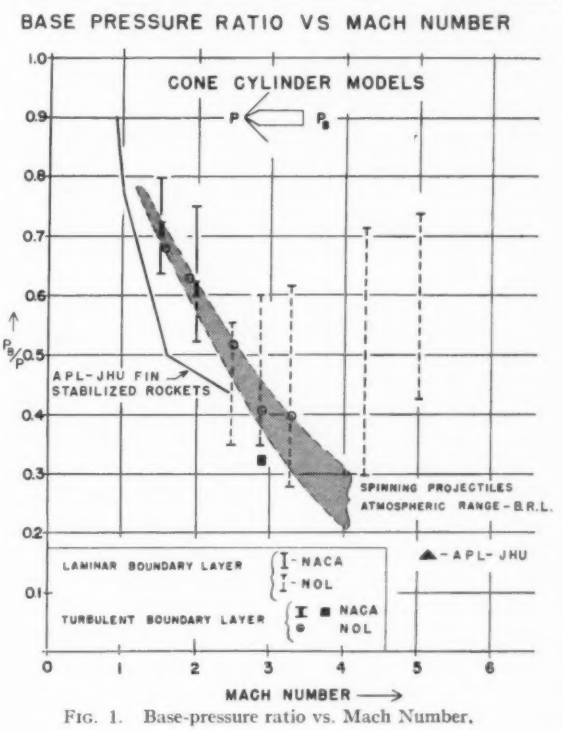

FIG. 1. Base-pressure ratio vs. Mach Number.

Presented at the Supersonic Aerodynamics Session, Nineteenth Annual Meeting, I.A.S., New York, January 29–February 1, 1951.

* Chief, Aeroballistics Division.

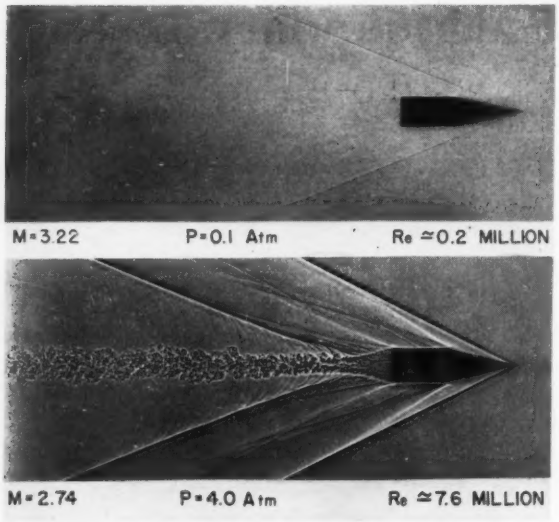

FIG. 2. Wake shapes of projectiles with laminar or turbulent boundary layer.

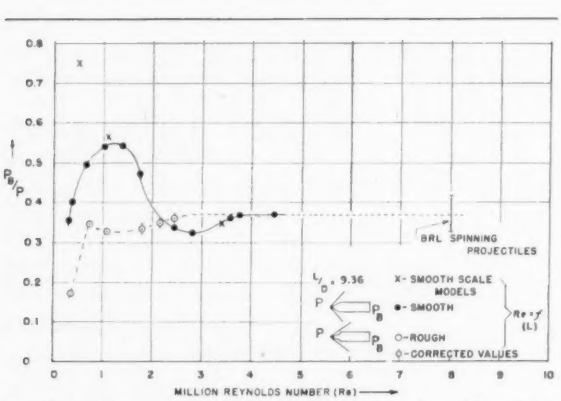

FIG. 3. Base-pressure ratio vs. Reynolds Number, $M = 3.24$.

wide region of measured values exists. In such a region the base drag obviously can vary more than 50 per cent.

Detailed investigations, however, soon showed that the test points could be separated into those points associated with laminar boundary layer on the bodies and those points associated with turbulent boundary layer. The turbulent data (circles and short black signs) are more or less restricted to the shaded area which represents the average scatter of the base-pressure ratio (ratio of base pressure to free-stream static pressure) obtained in the B.R.L. atmospheric range. The laminar values (long vertical lines) show much larger variation. A.P.L.'s tests with fin-stabilized rockets show especially low values in a Mach Number region between 1 and 2.5. Interference of body and fins might cause these low pressures. Furthermore, the character of the boundary layer on the fins in this region is not known.

This chart indicates clearly that the Mach Number is certainly not the only variable in the base-pressure function. Since the measurements and corresponding schlieren pictures (Fig. 2) indicate that the boundary layer is involved in the problem, the Reynolds Number must play an important part.

Base Pressure as Function of the Free-Stream Reynolds Number

The Mach Number was held constant and the base pressure resulting from variation of the Reynolds Number (Re) was measured. This variation was made in the N.O.L. wind-tunnel measurements by varying the lengths of the constant-diameter cylinders, as well as by reducing the diameter and length in proper scale. In the N.O.L. Pressurized Ballistics Range and in the A.A.L.[1] and Princeton University[5] wind tunnels, the Reynolds Number was varied there by changing the density of the air. One example of the wind-tunnel investigation at Mach 3.24 is presented in Fig. 3, where N.O.L. wind-tunnel data are plotted versus Reynolds Number.

It can be seen in this figure that in the low Reynolds Number range, where the boundary layer is fully or partly laminar, a large variation of the base pressure occurs. It was determined experimentally that, by simple modifications of the contour of the model nose (roughness has similar effect), the base pressure can be changed more than 50 per cent. In this case, at a Reynolds Number of approximately 3.5 million, a constant value seems to be reached. Here, the schlieren pictures show wake shapes as associated with turbulent boundary layer, as does the picture (Fig. 4 left below) of the model with disturbances at the nose already at 1.3 million. Large variations of the model surface in this constant region have relatively small effects on the base pressure. This apparent constant value is in agreement with B.R.L. firing-range data at the same Mach Number but at the much higher Reynolds Number, 8 million.

It is still debatable as to whether the turbulent value remains constant at extremely high Reynolds Number, as indicated by A.A.L.-N.A.C.A. measurements up to 16 million and by A.P.L. rocket tests up to 100 million ($M = 1.5$), or if a slight decrease takes place, as indicated in Princeton University's wind tunnel, Fig. 6.

Fig. 5 shows three more examples of Reynolds Number dependence, at Mach 1.5 and 2.0, reported by Chapman,[1] and at Mach 2.86 measured at N.O.L.[2] It can be seen in all three examples that the values become fairly constant as soon as turbulent boundary layer is developed whether or not this was initiated by artificial disturbance or by natural transition on the smooth models.

There has been insufficient time to obtain as much base-pressure data as desirable in the N.O.L. Pressurized Ballistics Range since its recent completion. On

Fig. 6, therefore, are plotted single data points obtained in a Mach Number range between 3.00 and 3.28 at pressures between 3 and 120 in. Hg with 30-caliber, 25° cone-cylinder bullets (length diameter ratio $L/D = 4$). Here, the laminar and transition range seems to be extended to larger Reynolds Number (5–7 million). For comparison, there are plotted the asymptote of the N.O.L. base-pressure curve for Mach 3.24 for fully developed turbulent boundary layer, which is reached already at a Reynolds Number of 2.5 million, and the curve obtained in the Princeton University pressurized wind tunnel at slightly lower Mach Number (between 2.95 and 2.98). Both wind-tunnel curves indicate a transition occurring at a much lower Reynolds Number than the free-flight data suggest. This might either be due to the larger cone angle (60° in the tunnel tests, 25° in the firing range tests) or to the degree of disturbance in the wind-tunnel air.

How much the shape of the body nose, the turbulence, and other irregularities of the air stream, such as shocks and pressure gradients, influence the transition quantitatively has not yet been sufficiently investigated. For short models ($L/D = 2$ and smaller) the variation of just the cylinder length, as well as the alteration of the nose shape, is accompanied by complicated changes of the boundary layer. Low base pressures are measured with extremely small L/D ratios. This fact can be seen on Fig. 3, where at the low Reynolds Numbers the scale model ($L/D = 9.36$) (denoted by x) has much higher base pressures than the short bodies.

Conclusions

From the described data it must be concluded that wind-tunnel base-pressure measurements on models with fully developed turbulent boundary layer and cylindrical bodies that are not too short give, in general, results that are in agreement with free-flight turbulent data within ±5 per cent.

To predict base pressures of bodies with laminar or partly turbulent boundary layer seems to be much more difficult, since the surface can hardly be imitated on the small models. In spite of the same Mach and Reynolds Number being maintained, the data for a model can deviate considerably from full-scale data when accidental disturbances cause some degree of turbulence in the boundary layer.

Uncertainty in base-pressure determination becomes still greater in compressible flow, at high Mach Numbers, where temperature plays an important part in the boundary-layer characteristics.

Influence of Model and Boundary-Layer Temperature on Base Pressure

So far it can be seen that the Mach Number and the free-stream Reynolds Number do not constitute all the base-pressure parameters. The change of the velocity profile causes base-pressure variations in spite of constant Mach and Reynolds Numbers. It should also be expected that temperature changes of the boundary layer and, in general, the temperature distribution in the boundary layer, characterized by Prandtl Number, alter the base pressure. The function $p_b/p = f(v, T, T_t)$ (p_b = base pressure, p = free-stream static pressure) (with v as the velocity profile, T as the temperature profile, and T_t as the profile of the total temperature of the boundary layer), therefore, was investigated with respect to the temperature profile.

Two cone-cylinder models [one with laminar ($L/D = 3$) the other one with turbulent ($L/D = 10$) boundary layer] were heated to approximately 400°F. and were cooled with dry ice to approximately −90°F. The results for Mach 3.24 and for $Re = 1.1$ million and 3.5 million, respectively, can be seen on Fig. 7a, where in both cases the base pressure is low at low model temperature (heat flowing from boundary layer to model) and increases with increase of model temperature. The effect is larger in the laminar than in the turbulent case, where the base pressure changes approximately 15 per cent in this temperature range. Fig. 7b shows the

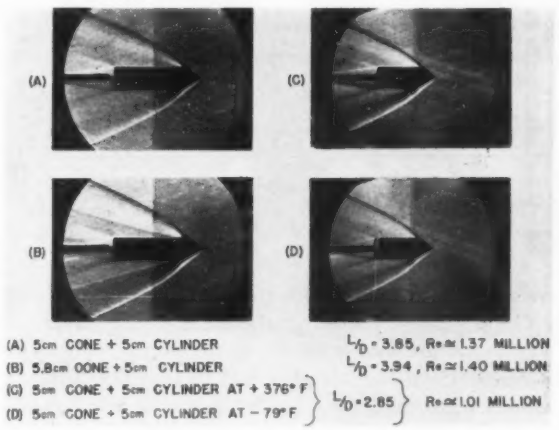
(A)
(C)
(B)
(D)
(A) 5cm CONE + 5cm CYLINDER
(B) 5.8cm CONE + 5cm CYLINDER
(C) 5cm CONE + 5cm CYLINDER AT + 376° F
(D) 5cm CONE + 5cm CYLINDER AT − 79° F
L/D = 3.85, Re ≃ 1.37 MILLION
L/D = 3.94, Re ≃ 1.40 MILLION
L/D = 2.85
Re ≃ 1.01 MILLION

Fig. 4. Wake changes due to boundary-layer variations. $M = 3.24$.

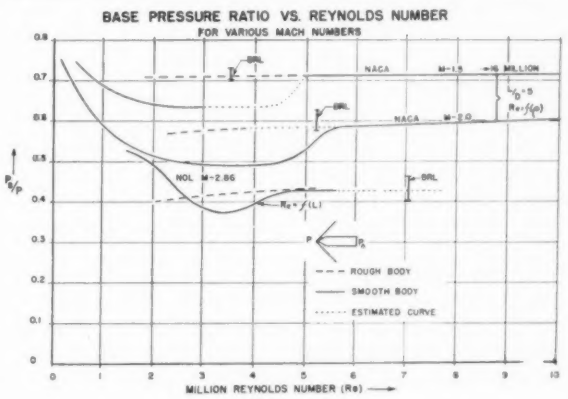

Fig. 5.

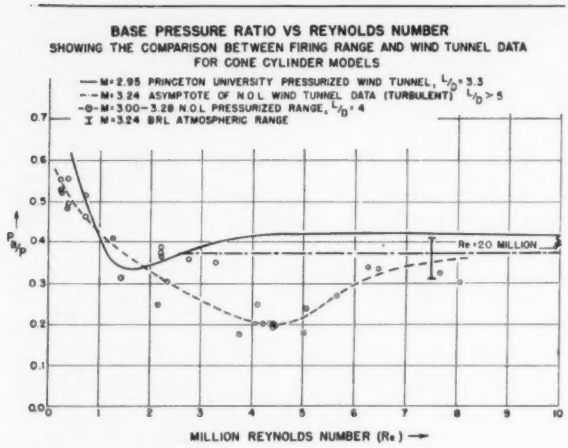
BASE PRESSURE RATIO VS REYNOLDS NUMBER
SHOWING THE COMPARISON BETWEEN FIRING RANGE AND WIND TUNNEL DATA
FOR CONE CYLINDER MODELS
M=2.95 PRINCETON UNIVERSITY PRESSURIZED WIND TUNNEL, L/D=3.3
M=3.24 ASYMPTOTE OF N.O.L. WIND TUNNEL DATA (TURBULENT) L/D>5
M=3.00-3.28 N.O.L. PRESSURIZED RANGE, L/D=4
M=3.24 BRL ATMOSPHERIC RANGE
Re=20 MILLION
MILLION REYNOLDS NUMBER (Re)

FIG. 6.

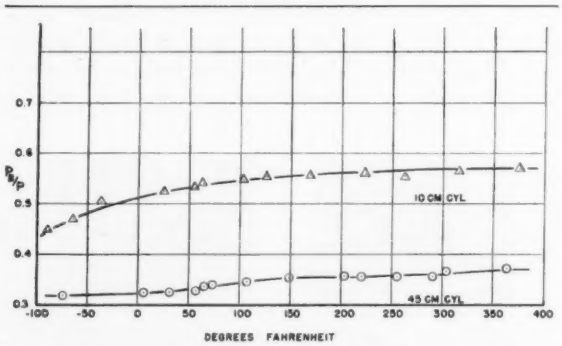

FIG. 7a. Base-pressure ratio vs. model-surface temperature, $M = 3.24$.

same effect at Mach Number 4.24. The 45-cm. model has in this case not a fully turbulent boundary layer.

In Fig. 4 are four schlieren pictures, which show, at constant Reynolds Number and Mach Number, the various wake shapes due to differences in the velocity and temperature profiles of the boundary layer.

Since in free flight at high Mach Numbers the hot boundary layer always loses heat by conduction to the missile from where part of it is radiated, we should expect that wind-tunnel measurements give higher base pressures than free-flight measurements at corresponding Mach Number. The temperature of the wind-tunnel models is approximately the same as that of the boundary layer.

Wind-tunnel measurements at Mach Numbers 4.24 and 5.0 seem to point in this direction.

THE EFFECT OF BOAT-TAILS ON THE BASE PRESSURE

So far, the possibilities of predetermination of base pressures for new missile designs have been discussed. In this connection also, the influence of the shape of the small L/D ratio bodies on the base pressure was briefly mentioned. Furthermore, it has been found that cylindrical models show a large variation of the base pressure when the tail is tapered and the boat-tail angle is varied.

Fig. 8 shows results from N.O.L. measurements at Mach 3.24 with two cone-cylinder models (one with laminar and the other with turbulent, or partly turbulent, boundary layer) and conical boat-tails. The boat-tail angle was varied between 0° and 15°, and the boat-tail length was 5 cm.

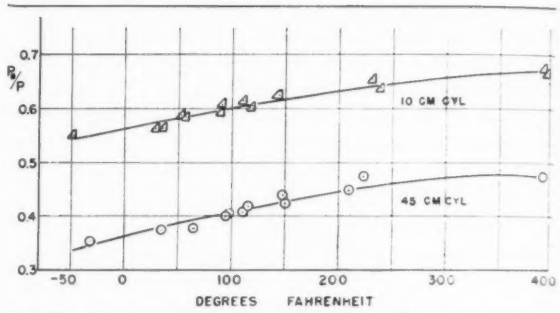

FIG. 7b. Base-pressure ratio vs. model-surface temperature, $M = 4.24$.

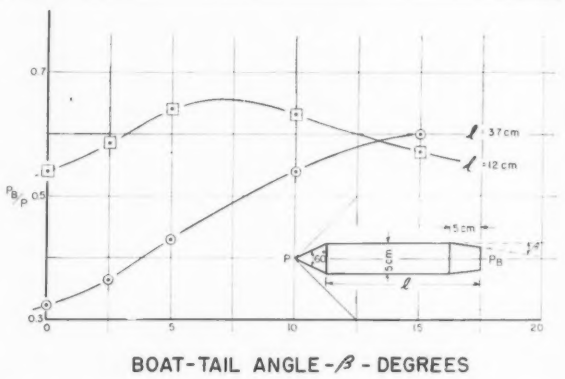

FIG. 8. Base-pressure ratio vs. boat-tail angle, $M = 3.24$.

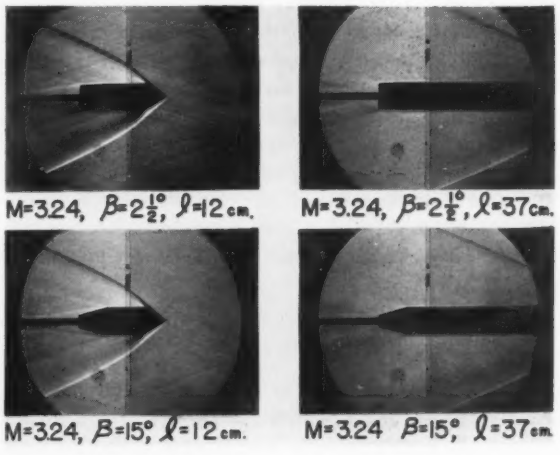

FIG. 9. Wake formation of boat-tailed bodies.

In both cases the base pressure increases with increasing boat-tail angle—in the laminar case to 7°, in the turbulent case to 15°. Fig. 9 shows that the laminar boundary layer is fully separated at 15°, whereas the turbulent boundary layer seems to be just detached at the same boat-tail angle. One would conclude, therefore, that bodies with turbulent boundary layer may be fitted out with larger boat-tail angles.

This advantage, unfortunately, is partly compensated by the increasing under pressure of the annular ring on the boat-tail, which gets larger and larger with increasing boat-tail angle. The net effect is the sum of base pressure times base area and of rim pressure times annular-ring area. This pressure distribution on the tail constitutes the total tail drag. Fig. 10 shows the resulting total tail-drag coefficient. It can be seen that in the turbulent case, as well as in the laminar case, an increase of boat-tail angle above 7° is useless in this example.

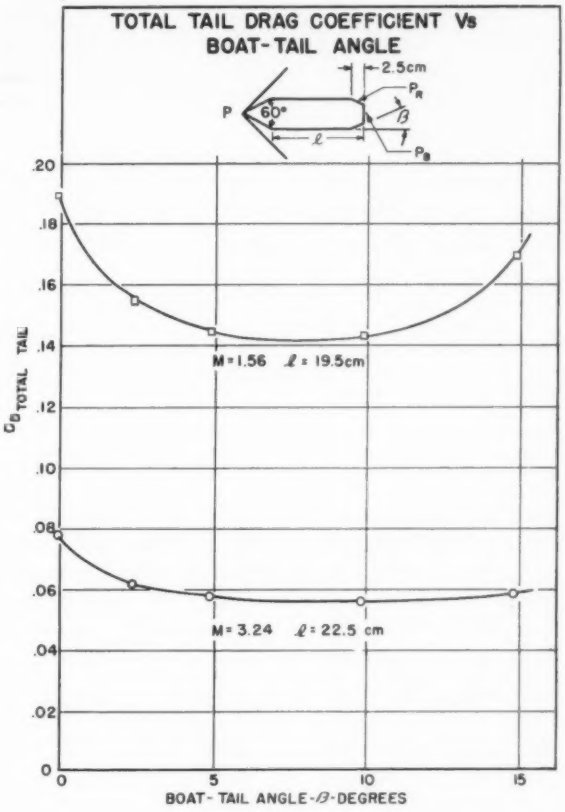

FIG. 10.

A HEURISTIC CONCEPT OF BASE PRESSURE

The described phenomena suggest a theoretical concept that should help the better understanding of the base-pressure mechanism and should make future calculations of the base drag possible.

It can be concluded from the experimental facts that the base-pressure problem is closely connected with boundary-layer characteristics, with surface friction, and with heat transfer. Therefore, theoretical calculations must take in account not only Mach Number and free-stream Reynolds Number but also the parameters of the boundary layer.

If one makes, as a first approximation, the crude assumption that the velocity of the air which is reduced in the boundary layer has to be restored after the boundary layer has separated from the body, the pressure at the end of the necessary expansion process can be calculated. The calculation, which requires the knowledge of the velocity and temperature profile and the stagnation-temperature distribution in the boundary layer, is based on the following function:

$$\frac{p_b}{p} = \frac{\int_{y=r}^{y=\delta} \frac{v_y}{v}\frac{\rho_y}{\rho}\frac{p_{\bar{y}}}{p}\, y\, dy}{\int_{y=r}^{y=\delta} \frac{v_y}{v}\frac{\rho_y}{\rho}\, y\, dy}$$

where v_y is the velocity and ρ_y is the density in the boundary layer at a distance y from the model surface; the boundary-layer thickness is δ, and the body diameter is $2r$. (The letters without subscript denote free-stream conditions.) The pressure $p_{\bar{y}}$ would be that of the layer y after the expansion if the air of the layer y could expand independent of the other layers y

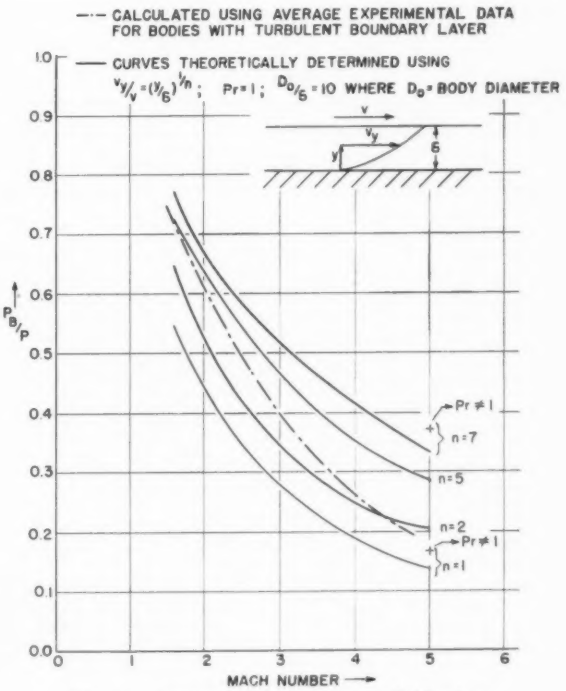

FIG. 11. Base-pressure ratio vs. Mach Number.

from the stagnation pressure p_{y0} and regain its original velocity v. Schlieren pictures indicate that this velocity is almost regained at approximately 2 or 3 diameters behind the base.

The pressures $p_{\bar{y}}$ have to be connected with the various masses of the layers y. The integrated products of pressure and mass have to be divided by the total amount of air contained in the boundary layer.

Replacing the density profile ρ_y/ρ by the temperature profile T_y/T and expressing $p_{\bar{y}}/p$ by the velocity term (given by adiabatic expansion),

$$\frac{v^2}{2} = \frac{a_{y0}^2}{\gamma - 1}\left[1 - \left(\frac{p_{\bar{y}}}{p_{y0}}\right)^{(\gamma-1)/\gamma}\right]$$

where a_{y0} = sonic speed at the stagnation temperature of layer y and p_{y0} = total pressure of the layer y, we obtain

$$\frac{p_b}{p} = \frac{\int_0^\delta \frac{v_y}{v}\frac{T}{T_y}\left\{\frac{1 + [(\gamma-1)/2]M^2\,[1 - (T_0/T_{y0})]}{1 + [(\gamma-1)/2]M^2[1 - (T_0/T_{y0})\,(v_y^2/v^2)]}\right\}^{\gamma/(\gamma-1)} y\,dy}{\int^\delta \frac{v_y}{v}\frac{T}{T_y}\,y\,dy}$$

Fully realizing that this concept can give only approximately correct values, especially since the boundary-layer profiles are not sufficiently known (in particular at higher Mach Numbers), we calculate this quantity. Fig. 11, for example, shows the evaluation for the base pressure of a cylindrical body with a boundary-layer thickness $\delta/r = 0.2$ and a Prandtl Number $Pr = 1$. The velocity profile is approximated by an exponential function $v_y/v = (y/\delta)^{1/n}$, with n taken for several values between 1 and 7.

The average experimental data, represented by the dashed curve, are located between the calculated curves. The effect of Prandtl Number not equal to 1 is estimated at Mach 5, resulting in higher base pressures.

Results

The results of base-pressure measurements in wind tunnels and firing ranges show that the base pressure is not only a function of the Mach Number and free-stream Reynolds Number but is also dependent on the specific boundary-layer conditions of the body as given by surface friction and heat transfer. Velocity and temperature profiles must be known before correct predictions of the base drag can be expected. Experimental data of boundary-layer profiles, especially at the higher Mach Numbers, are still missing. At present, only base-pressure data obtained by measurements with fully developed turbulent boundary layer can be used for full-scale base-drag estimations with reasonable accuracy.

References

[1] Chapman, Dean R., *An Analysis of Base Pressure at Supersonic Velocities and Comparison with Experiment*, N.A.C.A. T.N. No. 2137, 1950.

[2] Kurzweg, H. H., *New Experimental Investigations on Base Pressure in the NOL Supersonic Wind Tunnels at Mach Numbers 1.2 to 4.24*, N.O.L.M.-10113, 1950.

[3] *Faro, T. D. V., Experimental Determinations of Base Pressures at Supersonic Velocities*, Bumblebee Series Report No. 106, 1949.

[4] Charters, A. C., and Turetsky, R. A., *Determination of Base Pressures from Free-Flight Data*, B.R.L. Report 653, 1948.

[5] Bogdonoff, S. M., Report being published.

Shear Center for Thin-Walled Open Sections Beyond the Elastic Limit

G. H. HANDELMAN†

Carnegie Institute of Technology

SUMMARY

The location of the shear center of a thin-walled open section stressed beyond the elastic limit is determined by methods similar to those used in the elastic case. Through an analysis of the stress and strain components, the problem is reduced to determining one constant in the case of symmetric sections. This can be found from the magnitude of the applied force. The location of the shear center can then be found. Calculations for channel sections are carried out in detail, and the influence of the load and stress-strain law is shown in a numerical example. Formulas are also given for nonsymmetrical sections. The shear center, in the nonelastic case, is not a property of the section alone but depends on the stress-strain law and the applied force.

INTRODUCTION

THE PROBLEM OF DETERMINING the shear center for a thin-walled open section has been thoroughly treated for those cases in which the stresses remain below the elastic limit.[1] The present discussion is an attempt to extend this analysis beyond the elastic limit. The question will be considered as one of "technical plasticity" rather than a problem in the exact theory of metals stressed beyond the elastic limit. Various simplifying assumptions, of the order of those appearing in the theory of elasticity used in studying strength of materials, reduce the complexity of the mathematical analysis considerably. It is hoped that these results will give at least a good first approximation to the phenomena under study. In particular, a thin-walled open section with one axis of symmetry, clamped at one end and loaded with force F at the free end acting perpendicularly to the symmetry axis will be considered first (see Fig. 1). This beam can be conveniently described in terms of a right-handed rectangular system of axes (x, y, z) with the origin 0 located in the cross section at the free end. The z-axis will be directed along the axis of symmetry of the cross section, the x-axis is taken parallel to the axis of the beam, and the y-axis is perpendicular to both the x and z axes. The *shear center* s:$(0, 0, e)$ is the point at which F must be applied such that the torques produced by the shear flow, on one hand, and the force F, on the other, will be in equilibrium. In the elastic case, the coordinate e is independent of F and the elastic constants of the material; the present paper will consider the change in e with F when the material is stressed beyond the elastic limit.

A second system of coordinates, consisting of a reference line C in the cross section, the normals to C, and the x-axis, will be found useful. In this system, a point is given by the arc length s along C measured from a fixed point O, the normal distance n from C, and the coordinate x. The wall thickness $t(s)$ is measured along the normals to C and is not a function of x. Precise statements as to the assumption that the wall thickness is small will be given in later sections.

THE EQUATIONS OF EQUILIBRIUM

Only two stresses are assumed to act in the beam—an axial stress σ in the x-direction and a shear-stress τ parallel to the reference line C. This stress distribution will not fulfill the boundary condition of vanishing stress on the surface of the beam unless the inner and outer walls are also parallel to C. If the thickness is small, however, and the walls are almost parallel, the normal component will be small compared to the tangential component. Furthermore, τ and σ may be as-

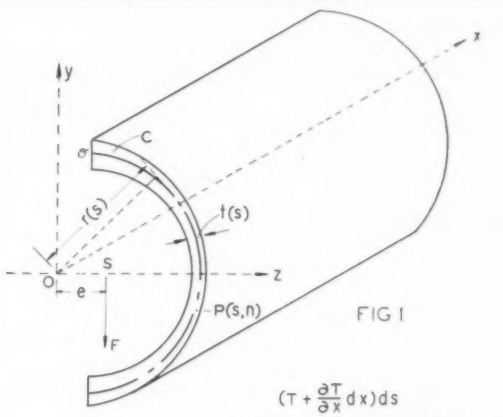

FIG 1

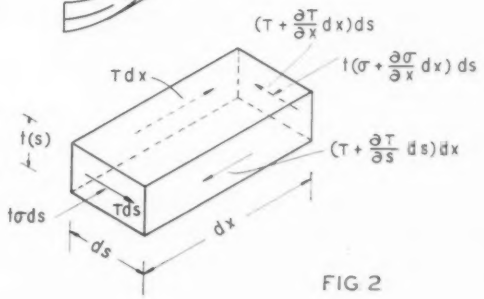

FIG 2

Received August 9, 1950.

† Assistant Professor of Mathematics.

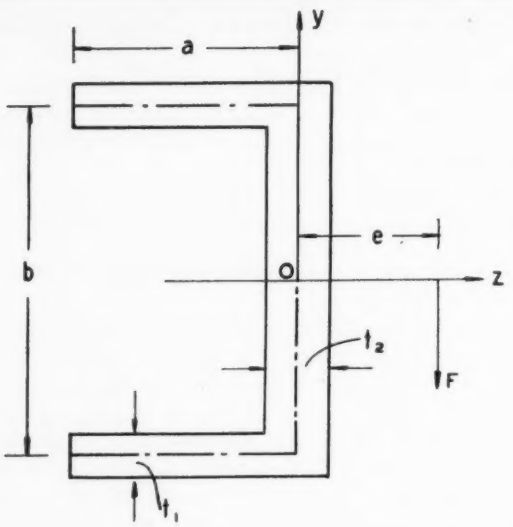

FIG. 3

sumed to be uniformly distributed across a normal to C if $t(s)$ is small. Under these conditions,

$$\tau = \tau(s, x), \qquad \sigma = \sigma(s, x)$$

The *shear flow*, $T(s, x)$, is defined by the relation

$$T(s, x) = t(s)\tau(s, x)$$

The equations of equilibrium can be obtained by considering the stresses acting on an element of a beam with sides ds, dx, $t(s)$ as shown in Fig. 2. For equilibrium in the x-direction,

$$T\,dx + t\sigma\,ds - t[\sigma + (\partial\sigma/\partial x)\,dx]\,ds - [T + (\partial T/\partial s)\,ds]\,dx = 0$$

or

$$(\partial T/\partial s) + [t(\partial\sigma/\partial x)] = 0 \tag{1}$$

In the s-direction,

$$T\,ds - [T + (\partial T/\partial x)\,dx]\,ds = 0$$

or

$$\partial T/\partial x = 0 \tag{2}$$

Eqs. (1) and (2) constitute the equations of equilibrium which must be fulfilled by the stresses T and σ. In particular, Eq. (2) implies that the shear flow is a function of s alone.

Introduction of the Stress-Strain Law

It has been found experimentally that when a prismatic beam is loaded in the direction of one of the principal axes of inertia of the cross section, the cross section will remain plane during bending.[2] Under this hypothesis, the axial strain ϵ will be a linear function of y—that is,

$$\epsilon = y\varphi(x) \tag{3}$$

where the function $\varphi(x)$ is still to be determined. If the dimensions of the cross section are small compared with the length of the beam, it is well known in the elastic case that the shear strain is small when compared with the axial strain.[3] The same assumption will be preserved in the case treated here, in the sense that the axial stress σ is supposed to be only a function of the axial strain ϵ—that is,

$$\sigma = \sigma(s, x) = E(\epsilon) = E[\epsilon(s, x)] \tag{4}$$

The function E can be evaluated from a tensile test. In the elastic case,

$$E(\epsilon) = E_0\epsilon$$

where E_0 is Young's modulus. Since most materials behave almost the same in compression and tension, $E(\epsilon)$ will be considered as an odd function of ϵ.

Eq. (2) can be integrated directly with the result

$$T(s, x) = -\int_0^s t(s)\,\frac{\partial\sigma(s, x)}{\partial x}\,ds + f(x)$$

where $f(x)$ must be determined from the boundary conditions. Since the edges of the section are free of stress, $T(0, x) = 0$. Consequently $f(x)$ must vanish also, and

$$T(s, x) = -\int_0^s t(s)\,\frac{\partial\sigma(s, x)}{\partial x}\,ds = -\int_0^s t(s)\,\frac{\partial E}{\partial x}\,ds \tag{5}$$

According to Eq. (2), $T(s, x)$ is a function of s alone; from Eq. (1) then

$$\partial^2\sigma/\partial x^2 = 0$$

Consequently, $\sigma(s, x)$ must be a linear function of x; or in other terms,

$$\sigma(s, x) = E[\epsilon(s, x)] = E[y\varphi(x)] = A_1(s)x + A_2(s) \tag{6}$$

The two functions, $A_1(s)$ and $A_2(s)$, can be found from the condition of equilibrium for the whole beam. Let $M = M(x)$ be the bending moment at any section x and l the total length of the reference line C. Now $M = -Fx$, but

$$M = -\int_0^l y(s)t(s)\sigma(s, x)\,ds$$

Thus,

$$Fx = \int_0^l y(s)t(s)\sigma(s, x)\,ds \tag{7}$$

and differentiation with respect to x yields

$$F = \int_0^l y(s)t(s)\,\frac{\partial\sigma(s,\,x)}{\partial x}\,ds = \int_0^l y(s)t(s)A_1(s)\,ds$$

Now for $x = 0$

$$A_2(s) = E[y(s)\varphi(0)]$$

and for $x = 1$

$$A_1(s) + A_2(s) = E[y(s)\varphi(1)]$$

or

$$A_1(s) = E[y(s)\varphi(1)] - E[y(s)\varphi(0)]$$

Eq. (7) can thus be rewritten in the form

$$Fx = x\int_0^l y(s)t(s)\,\{E[y(s)\varphi(1)] - E[y(s)\varphi(0)]\}\,ds + \int_0^l y(s)t(s)E[y(s)\varphi(0)]\,ds$$

In other terms, the functions $A_1(s)$ and $A_2(s)$ can be determined if two constants $\varphi(0)$ and $\varphi(1)$ are found such that

$$\int_0^l y(s)t(s)E[y(s)\varphi(1)]\,ds = F$$

$$\int_0^l y(s)t(s)E[y(s)\varphi(0)]\,ds = 0$$

The function $y(s)$ must be antisymmetric and $t(s)$ symmetric about $s = l/2$ from the assumed symmetry of the cross section. Since $E[y(s)\varphi(x)]$ is an odd function

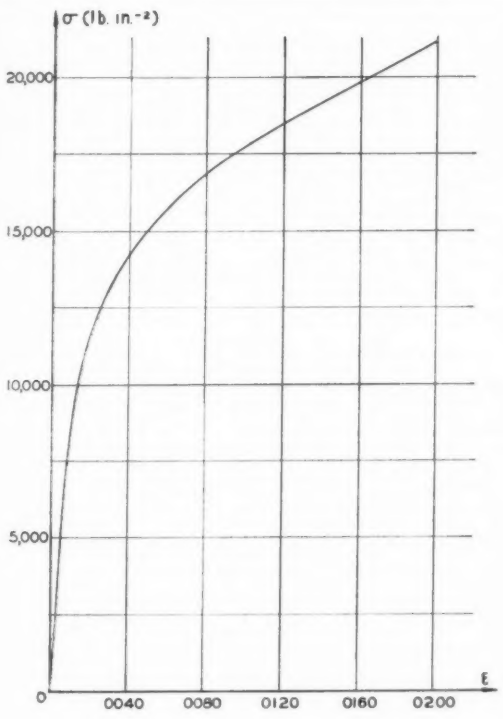

FIG 4

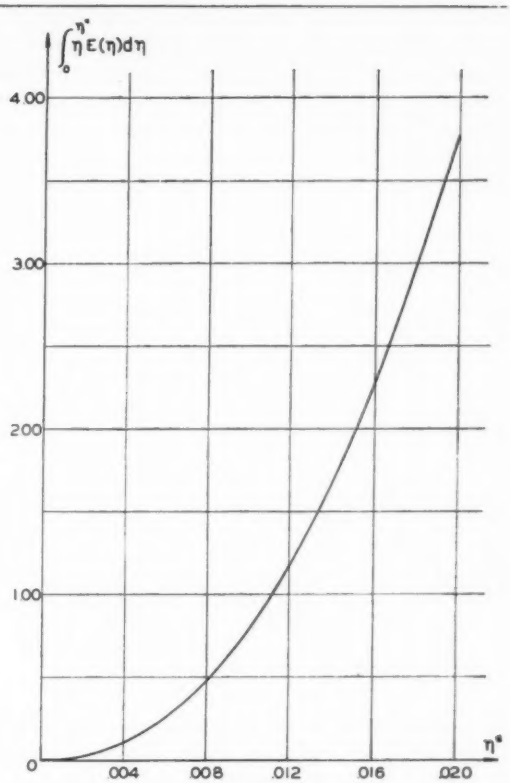

FIG 5

of ϵ, it will also be antisymmetric about $s = l/2$. Furthermore, $t(s) \geqq 0$; therefore,

$$\int_0^l y(s)t(s)E[y(s)\varphi(0)]\,ds$$

is strictly positive or strictly negative according to whether $\varphi(0) > 0$ or $\varphi(0) < 0$. It will vanish only if $\varphi(0) = 0$; thus, $\varphi(0) = 0$ and $A_2(s) = 0$, $A_1(s) = E[y(s)\varphi(1)]$. The stress distribution can be completely determined then by finding one constant $\varphi(1)$ such that

$$\int_0^l y(s)t(s)E[y(s)\varphi(1)]\,ds = F \qquad (8)$$

In practice, it is somewhat simpler to assume various values for $\varphi(1)$ and compute F rather than apply the direct method. Since

$$\partial E/\partial x = A_1(s) = E[y(s)\varphi(1)]$$

the shear flow T can be found from Eq. (5)—namely,

$$T = -\int_0^s t(s)E[y(s)\varphi(1)]\,ds$$

Location of the Shear Center

The shear center e can now be determined by computing the torque generated by the shear flow T. This torque must be equal in magnitude and oppositely

directed to the torque Fe produced by the force F applied at the shear center. Since the shear force is assumed to be uniformly distributed along the normal to the reference line, the torque due to the shear forces can be found by replacing these shear forces by the shear flow concentrated on the reference line. The torque Q is given by

$$Q = \int_0^l r(s)T(s)\ ds,$$

where $r(s)$ has been defined in the first section. Therefore,

$$Fe = -\int_0^l r(s)T(s)\ ds$$

or

$$e = -\frac{1}{F}\int_0^l r(s)T(s)\ ds = \frac{\displaystyle\int_0^l r(s)\left\{\int_0^s t(\xi)E[y(\xi)\varphi(1)]\ d\xi\right\} ds}{\displaystyle\int_0^l y(s)t(s)E[y(s)\varphi(1)]\ ds} \quad (9)$$

Consequently, when the constant $\varphi(1)$ has been determined for a given value of F according to Eq. (8), the shear center corresponding to this value of the applied force can be found from Eq. (9).

In the elastic case, $E[y(\xi)\varphi(1)] = E_0 y(\xi)\varphi(1)$, and Eq. (9) becomes

$$e = \frac{\displaystyle\int_0^l r(s)\left[\int_0^s y(\xi)t(\xi)\ d\xi\right] ds}{\displaystyle\int_0^l y^2(s)t(s)\ ds} = \frac{1}{I_z}\int_0^l r(s)\left[\int_0^s y(\xi)t(\xi)\ d\xi\right] ds \quad (10)$$

where I_z is the polar moment of inertia of the cross section about the z-axis. Eq. (10) contains the known result that, in the elastic region, the shear center is independent of the material—i.e., independent of E_0—and the applied force; it is only a function of the geometry of the cross section.[4]

Application to Channel Sections

The computation of the shear center as a function of the applied force, Eq. (9), is relatively simple in the important case of a channel section. Consider, for example, the section shown in Fig. 3 with the dimensions as indicated there. The origin of coordinates can be taken most conveniently at the center of the web. The constant $\varphi(1)$ can be found from Eq. (8) in the following way. Since $y(s) = b$ for $0 \leqq s \leqq a$ and the section is symmetric about the z-axis, Eq. (8) becomes

$$F = 2abt_1E[b\varphi(1)] + 2t_2\int_a^{a+b}(a + b - s)E[(a + b - s)\varphi(1)]\ ds \quad (11)$$

Now the integral appearing in Eq. (11) can be simplified, for

$$\int_a^{a+b}(a + b - s)E[(a + b - s)\varphi(1)]\ ds = \int_0^b \xi E[\xi\varphi(1)]\ d\xi$$

where $\xi = a + b - s$. By definition $\xi\varphi(1)$ has the dimensions of strain; it is convenient to set $\eta = \xi\varphi(1)$ Then

$$\int_0^b \xi E[\xi\varphi(1)]\ d\xi = \frac{1}{\varphi(1)^2}\int_0^{b\varphi(1)} \eta E(\eta)\ d\eta$$

Furthermore, let $\eta^* = b\varphi(1)$; Eq. (11) then becomes

$$F = 2abt_1\ E(\eta^*) + \frac{2b^2t_2}{\eta^{*2}}\int_0^{\eta^*} \eta E(\eta)\ d\eta \quad (12)$$

The integral appearing in Eq. (12) has the property that it is independent of the dimensions of the channel section. It can be evaluated as a function of the upper limit, η^*, once for all channel sections made of the same material provided that the stress-strain curve in tension is known. This integral has been evaluated for the stress-strain curve of Fig. 4, and the results are plotted in Fig. 5. For a section of given dimensions, a and b, it is more convenient to compute F as a function of η^* from Eq. (12) rather than find the value of η^* which corresponds to a given value of F. The quantity η^* is a useful parameter in this connection as well as in the subsequent evaluation of the position of the shear center, e, as a function of F.

The equation defining the shear center, Eq. (9), is also somewhat simplified in the case of channel sections since $r(s) = b$ for $0 \leqq s \leqq a$ and $r(s) = 0$ for $a < s \leqq a + b$. Since the integrand is symmetric about $s = a + b$,

$$e = \frac{2}{F}\int_0^a b\left[\int_0^s t_1E(\eta^*)\ d\xi\right] ds = \frac{a^2bt_1E(\eta^*)}{F} \quad (13)$$

Eq. (13) can be most readily evaluated by considering e as a function of η^* and using the corresponding values of F found from Eq. (12). The only difficulty in the computation occurs when $F = 0$; then η^* vanishes also and the expression for e is indeterminate. This problem is only superficial, however, since the material is elastic for small values of F and $E(\eta) = E_0\eta$. In this case,

$$F = 2abt_1E_0\eta^* + (2/3)b^2t_2E_0\eta^*$$

and

$$e = (a^2bt_1)/[2abt_1 + (2/3)b^2t_2] \quad (14)$$

As previously remarked this equation is independent of F and E_0; it can be used to find the position of the shear center for small values of the applied force.

These results have been applied to the case of a section with dimensions $a = b = 1.8$ in., $t_1 = t_2 = 0.15$ in. The final curve of e vs. F for this example is shown in Fig. 6. It is interesting to note that the change in the position of the shear center is less than 10 per cent of the minimum distance of the shear center from the center of the web. For small values of F, the function e is practically constant; this result arises from the fact that within this range of F the material behaves elastically and the shear center can be found essentially from Eq. (14). As the applied force is increased beyond this range, the position of the shear center shifts toward 0, reaches a minimum distance, and then starts to increase. This increase is caused by strain hardening in the material in the sense that the stress-strain curve (Fig. 4) is almost linear for strains larger than 0.01. If the material could be strained indefinitely without failure and if the basic assumptions were valid for such strains, the shear center would return to the position given by the elastic theory. Roughly speaking, for large strain values the nonlinear portion of the stress-strain curve has little influence, and the material behaves as an elastic body with a different Young's modulus. For an elastic body, however, the position of the shear center is independent of Young's modulus; consequently, the limiting value of the shear center will be independent of the tangent modulus in the strain-hardened range. This result can be found analytically by replacing $E(\eta)$ by $E_1\eta + k$ for $\eta > \eta_1$ in Eqs. (12) and (13). If η^* is then allowed to increase indefinitely, Eq. (14) will arise as a limiting case. This limiting case should not be taken too seriously since it exceeds the working range of the material and the original assumption of small deflections. On the other hand, such considerations explain the final increase in the distance of the shear center from 0.

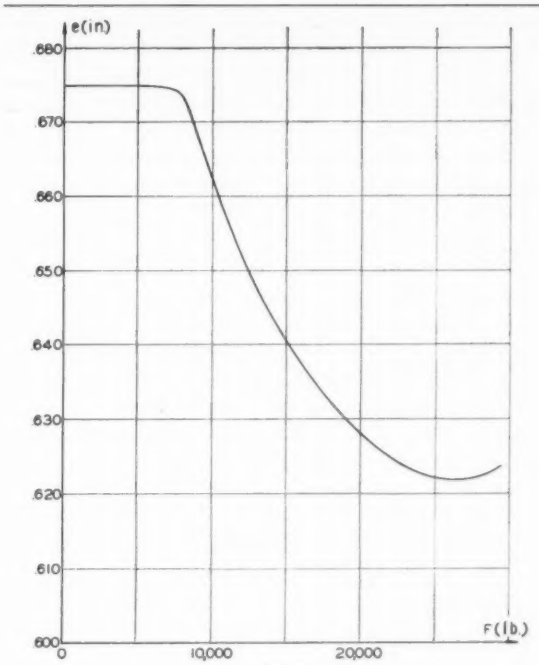

FIG 6

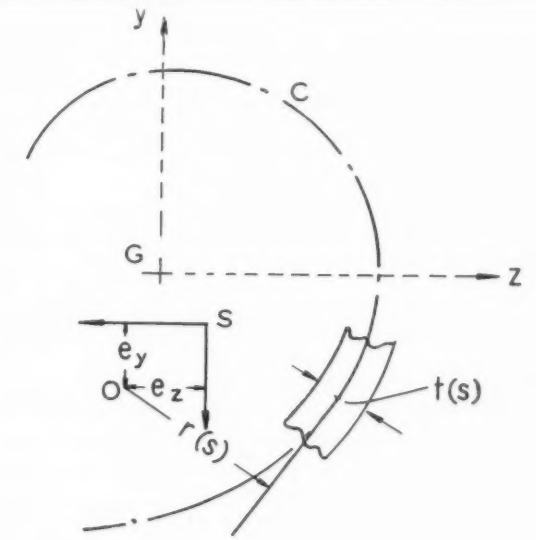

FIG. 7

Extension to Nonsymmetrical Sections

The previous analysis can be extended to the problem of determining the shear center of a nonsymmetric thin-walled section. Unfortunately, the resulting numerical calculations for a special case are not nearly so simple as those of the preceding discussion or the equivalent elastic problem. This difficulty is caused by the essential nonlinearity of the problem. If the applied force has components F_z and F_y, the problem for the elastic state is solved roughly in the following way.[5] The shear flow T_z corresponding to the force F_z alone can be found by a technique similar to that used in Section 4 specialized to an elastic stress-strain law. The requirement that the torque produced by F_z be in equilibrium with the torque produced by the shear flow T_z will determine a line $y = \text{const.}$ along which F_z must act. Similarly, the shear flow T_y can be found corresponding to F_y; and a similar line, $z = \text{const.}$, along which F_y must act, can be determined. Since the shear flow T which is produced by the force with components F_z and F_y is given by $T = T_z + T_y$, the intersection of these two lines will determine the shear center. In the nonelastic case, however, the shear flows can no longer be linearly superposed; the effects of both components F_z and F_y must be studied simultaneously. As will be

seen presently, the resulting numerical work is much heavier than that encountered in the previous section.

Consider an open thin-walled prismatic beam as shown in Fig. 7. Coordinate systems similar to those used in the preceding section will be used. Let G, the centroid of the undeformed cross section, be taken as the origin of a rectangular Cartesian coordinate system with the y and z axis lying in the plane of the cross section and the x axis parallel to the generators of the cylinder. Again $r(s)$ will denote the distance from a fixed point 0 to a tangent to the reference line C at the point s where, as usual, s denotes the arc length measured along C. As is customary in the theory of strength of materials, the parallel to the generators passing through G will be assumed to be the neutral fiber. In addition, the cross sections are supposed to remain plane. Consequently, the axial strain ϵ must be of the form

$$\epsilon = y\varphi(x) + z\psi(x)$$

where the functions $\varphi(x)$ and $\psi(x)$ are still to be determined. According to the stress-strain law, the axial stress σ can be written as

$$\sigma = E(\epsilon) = E[y\varphi(x) + z\psi(x)]$$

Now the equilibrium equations, Eqs. (1) and (2), are independent of whether or not the section is symmetric. Consequently,

$$\partial^2\sigma/\partial x^2 = 0$$

or

$$\sigma = xA_1(s) + A_2(s) \tag{15}$$

The functions $A_1(s)$ and $A_2(s)$ are still to be found. Since $\sigma = E[y\varphi(x) + z\psi(x)]$,

$$A_2(s) = E[y\varphi(0) + z\psi(0)]$$
$$A_1(s) = E[y\varphi(1) + z\psi(1)] - E[y\varphi(0) + z\psi(0)]$$

On the other hand, the beam is loaded only in the plane of the cross section at $x = 0$; consequently, the axial stress σ must vanish for $x = 0$. Therefore, $A_2(s) = E[y\varphi(0) + z\psi(0)] = 0$ for all values of y and z. Since the function E vanishes only when the argument is zero, this implies that $\varphi(0) = \psi(0) = 0$ and

$$A_1(s) = E[y\varphi(1) + z\psi(1)]$$

The bending moment with axis in the z-direction is given by

$$-F_y x = -\int_0^l y(s)t(s)\sigma(s, x)\,ds = -\int_0^l y(s)t(s)xA_1(s)\,ds$$

where l is the total length of the reference line. Similarly for the moment in the y-direction,

$$F_z x = \int_0^l z(s)t(s)\sigma(s, x)ds = \int_0^l z(s)t(s)xA_1(s)\,ds$$

Consequently,

$$F_y = \int_0^l y(s)t(s)A_1(s)\,ds$$
$$F_z = \int_0^l z(s)t(s)A_1(s)\,ds$$

or

$$\left.\begin{aligned} F_y &= \int_0^l y(s)t(s)E[y\varphi(1) + z\psi(1)]\,ds \\ F_z &= \int_0^l z(s)t(s)E[y\varphi(1) + z\psi(1)]\,ds \end{aligned}\right\} \tag{16}$$

Given values of F_y and F_z, the constants $\varphi(1)$ and $\psi(1)$ can be found by solving Eqs. (16). The problem of determining $\varphi(1)$ and $\psi(1)$ is thus reduced to solving two simultaneous equations that, in general, are not linear in $\varphi(1)$ and $\psi(1)$. This is one of the basic numerical differences between the nonsymmetric and the symmetric problem in which only one constant must be found [see Eq. (9)]. Should it be desirable to find the shear center for a continuous range of F_y matched with all values of a continuous range of F_z, the computation can be reversed by picking a suitable set of values of $\varphi(1)$ and $\psi(1)$ and determining the corresponding F_y and F_z by means of Eq. (16).

Assuming that the constants $\varphi(1)$ and $\psi(1)$ have been found, the position of the shear center can be determined by a procedure analogous to that used in the symmetric case. According to Eqs. (1) and (15), the shear flow $T(s, x)$ is given by

$$T(s, x) = -\int_0^s t(s)\frac{\partial\sigma(s, x)}{\partial x}\,ds = -\int_0^s t(s)A_1(s)\,ds$$
$$= -\int_0^s t(s)E[y\varphi(1) + z\psi(1)]\,ds$$

Let e_y and e_z, respectively, be the y and z coordinates of the shear center with respect to a fixed point 0 in the plane of the cross section. Then the torque Q produced about 0 by the forces F_y and F_z is

$$Q = -F_y e_z + F_z e_y$$

On the other hand,

$$Q = \int_0^l r(s)T(s)\,ds$$

therefore,

$$F_y e_z - F_z e_y = \int_0^l r(s)\left\{\int_0^s t(\xi)E[y(\xi)\varphi(1) + z(\xi)\psi(1)]\,d\xi\right\}ds \tag{17}$$

Eq. (17) then determines the line of action of the force.

(*Continued on page 766*)

The Effect of Flight and Configuration Variables on Thermal Stresses in Diamond-Shaped Supersonic Wings*

FRANKLIN P. DURHAM†
University of Colorado

SUMMARY

For aircraft traveling at high supersonic speeds, approximate stagnation temperatures exist in the boundary layer surrounding the aircraft. If the aircraft has accelerated rapidly to a high supersonic speed, large transient temperature gradients will be introduced, which may, in turn, cause high thermal stresses.

Methods for the determination of the transient temperatures and the stresses resulting from these temperatures are presented for solid diamond-shaped airfoils. Numerical results are given, showing the effects of several flight and configuration variables based on a wing of given specifications.

It is shown that the maximum thermal stresses occurring in the chosen wing are compressive stresses at the leading edge. It is further shown for the severe flight conditions assumed that these stresses are of large magnitude.

SYMBOLS

Following is a list of the principal notations used:

a = thermal diffusivity, k/wc_t
c = chord length, ft.
c_t = specific heat of wing material, B.t.u. per lb.°F.
c_p = specific heat of air, B.t.u. per lb.°F.
E = modulus of elasticity, lbs. per sq.in.
g = acceleration due to gravity, 32.2 ft. per sec.²
h = convective heat-transfer coefficient for air, B.t.u. per ft.² sec.°F.
J = mechanical equivalent of heat, 778 ft.lb. per B.t.u.
k = thermal conductivity of wing material, B.t.u. per ft. sec.°F.
k_a = thermal conductivity of air, B.t.u. per ft. sec.°F.
l = beamwise thickness of wing at any chordwise station, ft.
M = Mach Number
p = air pressure, lbs. per sq.ft.
r = recovery factor, dimensionless
t = maximum beamwise thickness, ft.
T = average beamwise temperature at any chordwise station, °R.
T_a = initial temperature of wing, °R.
T_{aw} = adiabatic wall temperature, °R.
T_m = mean linear chordwise temperature variation that would produce deflection but no stress, °R.
T_n = mean linear beamwise temperature variation that would produce deflection but no stress, °R.
T_0 = free-stream temperature, °R.
T_s = stagnation temperature, °R.
T_z = temperature at any beamwise point, °R.
u = speed, ft. per sec.
w = specific weight of wing material, lb. per ft.³
x = distance along chord, measured from leading edge, ft.
y = distance along span, ft.
z = distance in beamwise direction, ft.
Nu = Nusselt Number
Pr = Prandtl Number
Re = Reynolds Number
α = linear coefficient of thermal expansion, ft. per ft.°F.
θ = time, sec.
μ = viscosity
ν = Poisson's ratio, ft. per ft.
σ_y = thermal stress due to combined chordwise and beamwise temperature variation, lbs. per sq.in.
σ_{yb} = thermal stress due to beamwise temperature variation
σ_{yc} = thermal stress due to chordwise variation of average beamwise temperature
τ = $(T_{aw} - T)/(T_{aw} - T_a)$

Received May 10, 1951.

* This paper represents a portion of the work carried out for the U.S. Air Force under Contract No. W33-038-ac-17240 and is an advance release of a portion of U.S.A.F. Technical Report No. 6351. The project was directed by Prof. H. W. Sibert. Members of the University of Colorado Engineering Experiment Station staff, who assisted in the work, are listed in references 3 to 16.

† Assistant Professor of Aeronautical Engineering.

INTRODUCTION

FOR AIRCRAFT TRAVELING at high supersonic speeds, approximate stagnation temperatures exist in the boundary layer surrounding the aircraft. For example, the boundary-layer temperature at a Mach Number of 4 at sea level is approximately 2,000°F. The effect of this high temperature boundary layer is to heat the material that it surrounds, primarily by forced convection.

If the aircraft has accelerated rapidly to a high supersonic speed, large transient temperature gradients will be introduced, which may, in turn, cause high thermal stresses. If the acceleration is slow, the aircraft will heat more or less uniformly, causing thermal expansion but only small thermal stresses.

The problem of thermal stresses due to aerodynamic heating is particularly important in supersonic wings, which are thin and thus subject to being heated quickly and, moreover, are highly stressed due to the aerodynamic loading without the addition of thermal stresses.

Before thermal stresses can be found, the temperature distribution in the wing under consideration must be obtained. The determination of the temperature distribution, in general, involves the solution of three-dimensional heat flow in the transient state.

This report contains the results of an investigation of temperature distributions and thermal stresses in a

wing in supersonic flight. The program undertaken was composed of two parts, analytical and experimental. Analytical studies of the various problems involved were made. These studies were followed as far as possible by experimental tests to verify the theoretical work.

In order to reduce the number of variables, a solid, thin, diamond-shaped wing was taken as the basis of study. This basic wing was considered to be initially at uniform temperature and then instantaneously subjected to a steady supersonic flight Mach Number. The instantaneous attainment of the flight Mach Number would impose the most severe thermal stresses possible for the given flight Mach Number and is thus the limiting condition approached by rapid acceleration of an aircraft or missile.

The importance of the various types of heat flow—chordwise, beamwise, spanwise, and the combinations of chordwise and beamwise and chordwise and spanwise—were investigated in order to obtain the simplest solution of reasonable accuracy. Investigations were also made of the effects of flight and wing-configuration conditions on thermal stresses.

Experimental tests were conducted to verify the results of the analytical investigations insofar as possible. The experimental program consisted of simulating the conditions of heat input to model wings and determining temperature distributions and thermal stresses.

The description and results of these individual analytical and experimental investigations are listed as references 3 to 16 inclusive.

Basic Conditions and Assumptions

Wing

The basic wing used in these studies had the following characteristics.

(1) *Configuration*
- (a) Solid, diamond-shape with $^1/_{16}$-in. leading and trailing edges
- (b) Chord, 4 ft.
- (c) Span, 16 ft.
- (d) Maximum thickness, 5 per cent of chord (0.2 ft.)
- (e) Taper, none

(2) *Material—mild steel*
- (a) Specific weight, 492 lbs. per ft.^{3}
- (b) Specific heat, 0.122 B.t.u. per lb.°F.
- (c) Thermal conductivity, 0.0072 B.t.u. per ft. sec.°F.
- (d) Coefficient of thermal expansion, 6.5×10^{-6} in. per in.°F.
- (e) Young's modulus, modulus of elasticity in tension or compression, 28,000,000 lbs. per sq.in.

Flight Conditions

Although the method adopted for the determination of temperature distribution and thermal stresses is a step-by-step process and applies equally well to flight with finite acceleration, the most severe flight conditions were chosen for all problems analyzed. That is, the wing under consideration was assumed to be initially at a low uniform temperature and then instantaneously subjected to a steady supersonic Mach Number.

Simplifying Assumptions

The following assumptions apply to all solutions obtained. Additional assumptions were made with regard to particular problems and will be listed in the sections where the problems are described.

(1) Heat transfer by radiation to or from the wing surface is negligible.

(2) The specific heat, specific weight, thermal conductivity, coefficient of thermal expansion, and the modulus of elasticity of the wing material are constant.

(3) The wing does not buckle and is not restrained.

Heat-Transfer Coefficient

Considerable uncertainty exists in the evaluation of convective heat-transfer coefficients in supersonic flows. The following relations have been widely used for predicting supersonic heat-transfer coefficients: For laminar boundary layers

$$Nu = hx/k = 0.33 Re_x^{1/2} Pr^{1/3} \tag{1}$$

and for turbulent boundary layers

$$Nu = hx/k = 0.030 Re_x^{0.8} Pr^{1/3} \tag{2}$$

in which the Reynolds and Nusselt Numbers are evaluated in terms of the distance x from the leading edge.

The choice of the air temperature in evaluating Eqs. (1) and (2) is subject to considerable question for supersonic flows and has been the subject of numerous investigations. The air temperature at the wing surface has been used as well as the temperature in the free stream just outside the boundary layer.

References 1 and 2 recommend the use of the surface temperature. In the transient state, the surface temperature varies with time, consequently the heat-transfer coefficient based on the surface temperature would vary with time. In order to simplify the problem, it was felt desirable to use a heat-transfer coefficient that was constant with time. For this reason, the so-called "adiabatic wall" temperature, which all surface temperatures approach with increasing time, has been used throughout this report. This temperature will be referred to as the adiabatic wall temperature.

In the early time of the transient state near the leading and trailing edges, the surface temperature approaches the adiabatic wall temperature while the surface temperature near the mid-chord is much lower than the adiabatic wall temperature. Consequently, the re-

sult of using the adiabatic wall temperature instead of the surface temperature is that values of heat-transfer coefficient near the leading and trailing edges will be approximately the same as those based on the surface temperature, while, in the region near the mid-chord, the values will be appreciably lower than those based on the surface temperature.

On the other hand, the use of the free-stream temperature just outside the boundary layer will result in values of heat-transfer coefficient near the leading and trailing edges which are much greater than those based on the surface temperature, while, in the region of the mid-chord, the values will also be somewhat greater than those based on the surface temperatures.

These variations are due to the fact that the adiabatic wall temperature is approximately the stagnation temperature, while the free-stream temperature outside the wing boundary layer is not greatly different from the ambient temperature in front of the wing (even though oblique shock waves are attached at the leading edge).

The value of heat-transfer coefficient is important in the determination of transient-state temperature distributions and thermal stresses, and, in light of this discussion, the numerical results presented here may be subject to change when more is known about the determination of supersonic heat-transfer coefficients.

The transition from laminar to turbulent boundary layers for supersonic flows is believed to occur at a Reynolds Number of about 500,000.[1] For all problems considered in this investigation, the transition would then occur within a few inches of the leading edge of the wing, where the wing is extremely thin. In order to simplify the calculations, the flow over the entire wing was considered turbulent, even though the methods of solutions used apply equally well when both laminar and turbulent boundary layers exist on the wing.

Recovery Factor

The temperature in the boundary layer near the wing surface has a maximum value of approximately the stagnation temperature but varies with distance from the surface depending on the rate of heat transfer. In the correlation of heat-transfer data, the adiabatic wall temperature is defined as the temperature that would exist at the surface if the surface were perfectly insulated rather than the temperature that actually exists at the surface. The recovery factor relates the adiabatic wall temperature to the free-stream temperature ahead of the airfoil and the stagnation temperature in the following manner:

$$r = (T_{aw} - T_0)/(T_s - T_0) \tag{3}$$

Recovery factors have been determined experimentally and appear to be more dependent on the type of boundary layer (laminar or turbulent) than on the free-stream speed. The values of recovery factors which have been reported range from 0.8 for laminar to 0.95 for turbulent boundary layers. For all numerical solutions presented in this report a turbulent boundary layer was assumed, and a recovery factor of 0.92 was used even though there is experimental evidence that the recovery factor increases with increasing Mach Number. One result of the use of a constant recovery factor is that the calculated boundary-layer temperature is the same for both upper and lower surfaces of the wing regardless of the angle of attack.

Investigation of Heat Flow

The analytical determination of thermal stresses depends upon the knowledge of the internal temperatures of the wing under consideration. The determination of these temperatures is, in general, a three-dimensional, transient-state, heat-transfer problem whose solution is extremely complex.

In order to obtain an engineering solution combining reasonable simplicity and accuracy, an investigation was undertaken to determine the importance of the three possible types of heat flow—chordwise, beamwise, and spanwise. The following specific problems were studied:

(a) Chordwise and beamwise heat flow assuming no temperature gradients in the beamwise direction. This method is presented in references 12 and 13 and verified experimentally in reference 16.

(b) Chordwise, beamwise, and spanwise heat flow assuming no temperature gradients in the beamwise direction. This method is presented in reference 4.

(c) Beamwise heat flow only assuming symmetrical boundary conditions. This method is presented in reference 7 and verified experimentally in reference 14.

(d) Beamwise heat flow only assuming unsymmetrical boundary conditions. This method is presented in reference 5 and verified experimentally in reference 14.

(e) Chordwise and beamwise heat flow assuming symmetrical beamwise boundary conditions. This method is presented in reference 8.

(f) Chordwise and beamwise heat flow assuming unsymmetrical beamwise boundary conditions. This method is presented in reference 10.

The results of these investigations showed that the chordwise variation in temperature was always greater than the variation in any other direction, indicating that the thermal stresses of greatest magnitude would be produced by chordwise temperature gradients.

The investigation also showed that the chordwise variation in temperature could most easily be obtained with a high degree of accuracy from the method listed as (a) above. The simplifying assumptions made for this method reduce it to a one-dimensional numerical step-by-step process that is easily solved. All the above methods were developed in terms of a dimensionless temperature parameter τ such that

$$\tau = (T_{aw} - T)/(T_{aw} - T_a) \tag{4}$$

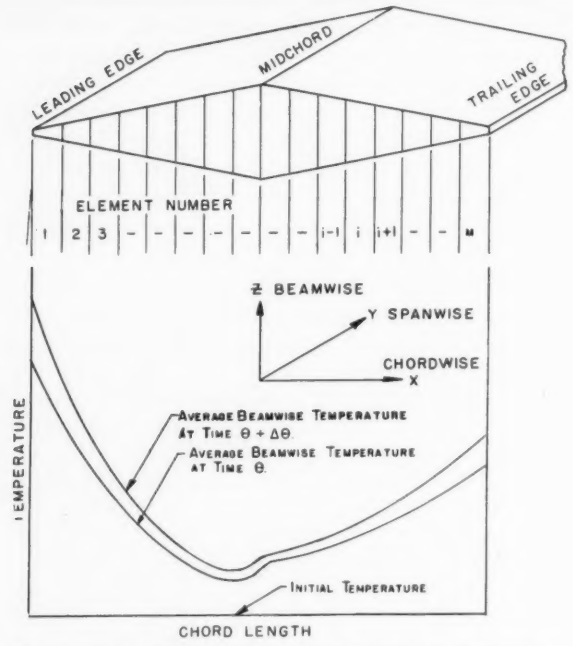

FIG. 1. Wing layout showing typical chordwise variation of average beamwise temperatures.

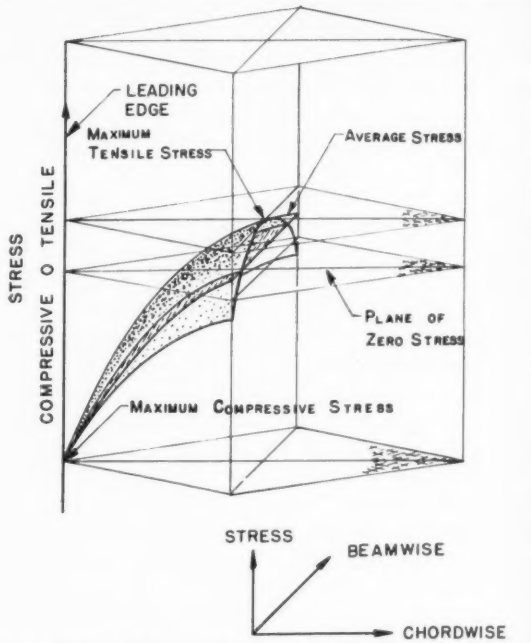

FIG. 2. Schematic diagram of typical stress distribution in front half of a diamond-shaped wing.

Chordwise Temperature Distribution

The method adopted for the determination of the chordwise temperature distribution consists of dividing the wing cross section into a number of elements m of equal chordwise length, Δx, as shown in Fig. 1, and choosing a small time interval, $\Delta\theta$, where the temperatures are obtained at the end of successive time intervals. The dimensionless temperatures of any element i are then given by the following equation:

$$\tau_i = a_i\tau_{i-1} + b_i\tau_{i-1}^{\circ} + d_i\tau_i^{\circ} + e_i\tau_{i+1}^{\circ}, \qquad i \leq i \leq m \quad (5)$$

where

$$\left.\begin{aligned} a_i &= (\lambda_i - 1)f_i \\ b_i &= (\lambda_i + 1)f_i \\ d_i &= (A_i - 3 - \lambda_i - D_i)f_i \\ e_i &= 2f_i \\ f_i &= 1/(A_i - 1 + \lambda_i + D_i) \end{aligned}\right\} \qquad 1 < i < m \quad (6)$$

$$\left.\begin{aligned} a_1 &= b_1 = 0 \\ d_1 &= (A_1 - 2 - \beta_0 D_1)f_1 \\ e_1 &= 2f_1 \\ f_1 &= 1/(A_1 + \beta_0 D_1) \end{aligned}\right\} \qquad i = 1 \quad (7)$$

$$\left.\begin{aligned} a_m &= b_m = \lambda_m f_m \\ d_m &= (A_m - \lambda_m - \beta_m D_m)f_m \\ e_m &= 0 \\ f_m &= 1/(A_m + \lambda_m + \beta_m D_m) \end{aligned}\right\} \qquad i = m \quad (8)$$

and

$\lambda_i = z_{i-1}/z_i$ (where z_i = beamwise height of right face of element i (9)

$$A_i = c_i w(\Delta x)^2(1 + \lambda_i)/(k_i\Delta\theta) \quad (10)$$

$$D_i = (h_{ui} + h_{li})(\Delta x)^2/(k_i z_i) \quad (11)$$

$$\beta_0 = 1 + z_0/2\Delta x \quad (12)$$

$$\beta_m = 1 + z_m/2\Delta x \quad (13)$$

The superscript $^{\circ}$ with a temperature indicates the temperature at the end of the time interval immediately preceding the time interval under consideration. Thus all τ°'s in Eq. (5) are known. Temperatures are determined successively from left to right so that τ_{i-1}, which refers to the element preceding element i, will also be known for the determination of τ_i in Eq. (5).

Fig. 1 shows the wing cross-section layout for this method, as well as typical chordwise temperature distributions. A sample calculation illustrating the use of this method is given in reference 12.

It was found that this method yielded results of comparable accuracy to those of the more complicated methods (b), (e), and (f) previously described, and, for the region near the leading and trailing edge, the results of this method were much more accurate than those of methods (c) and (d). A discussion of the limitations of beamwise solutions for the determination of chordwise temperatures is given in reference 5.

Another advantage of this method of solution is that it is applicable in the case where heat-transfer coefficients and adiabatic wall temperatures vary with time as well as chordwise station. Thus, it can be used

for any prescribed flight plan including take-off, acceleration, steady flight, deceleration, and landing.

An experimental program was undertaken to verify the accuracy of this method for determining chordwise temperature distributions. A mild-steel, diamond-shaped wing model with thermocouples installed internally along the chord and connected through a galvanometer to a recording oscillograph was suddenly immersed in a water bath that was at the boiling point. Transient temperatures were measured, and, based on calculated heat-transfer coefficients for the water bath, good agreement with the theoretical solution was obtained. The details of this program are given in reference 16.

Investigation of Thermal Stresses

The determination of thermal stresses requires that the internal and surface temperatures throughout the wing be known at any time for which the stresses are to be found. Due to the wing configuration and the manner in which the temperature gradients occur, the primary thermal stresses act in the spanwise or y direction. The stresses over a cross section at any spanwise station may be thought of as composed of two parts: (a) a stress produced by the chordwise variation of the average beamwise temperature which will be referred to as the average stress; (b) a stress produced by a beamwise temperature variation at the point in question. Since both of these stresses act in the spanwise direction, they may be added algebraically, yielding the resultant stress at any point.

Stresses Due To Chordwise Temperature Variations

Numerical methods of solution for the stresses due to the chordwise temperature variation are presented in references 3 and 6. The chordwise temperatures considered are the values of the average beamwise temperatures at any location along the chord. The argument for the solution of reference 6, which is based on the assumption of plane stress in the plane of the wing cross section shown in Fig. 1 resulting from chordwise temperature variation and is limited to symmetrical diamond-shaped wings with blunt leading and trailing edges, may be summarized as follows:*

If the chordwise temperature variation is nonlinear and is not symmetrical about the mid-chord, in addition to thermal stresses, a deflection of the wing will occur along the span in the direction of the chord. This same deflection could result from a mean linear chordwise temperature variation that would cause no stress, with the amount of the deflection roughly proportional to the slope. The difference between the actual chordwise temperature and this mean linear temperature at a point causes thermal stress.

In the case of temperature variations that are symmetrical about the midchord, no deflection results and the slope of the mean linear temperature variation that would cause deflection but no stress is zero. Thus, the

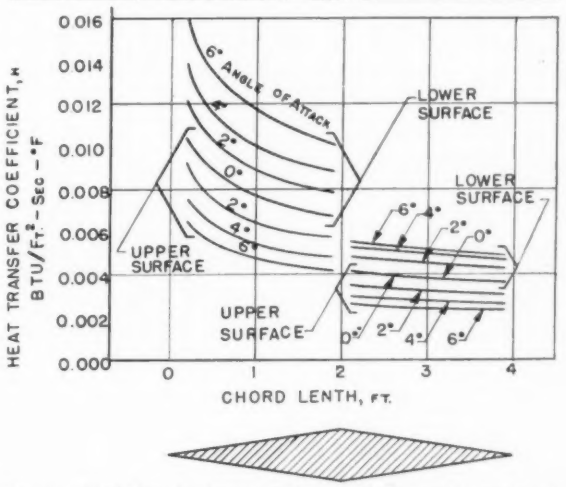

FIG. 3. Variation in heat-transfer coefficient with angle of attack; $M = 4$; 60,000 ft. altitude.

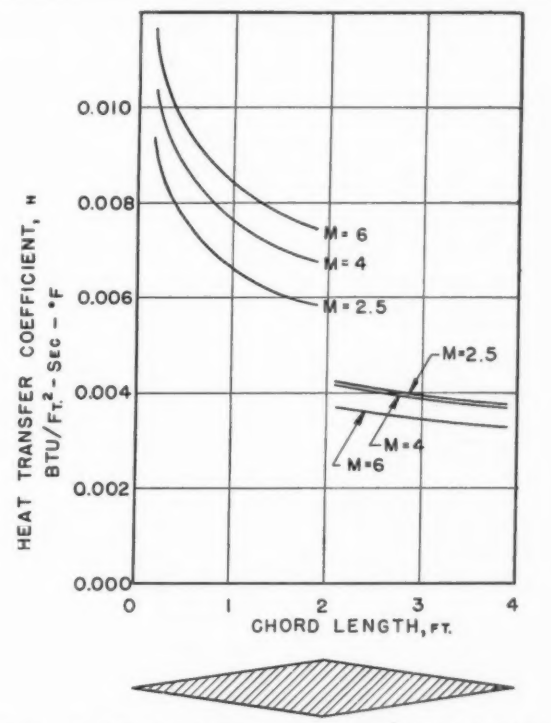

FIG. 4. Variation in heat-transfer coefficient with Mach Number; zero angle of attack; 60,000 ft. altitude.

* For wings having cross sections other than a symmetrical diamond shape, the method of reference 3 should be used, since it is not limited to any particular cross-section configuration. Both the methods yield identical results for diamond-shaped wings. The method of reference 6 is presented here since the concept of the mean linear temperature variation is helpful in visualizing thermal stresses.

temperature difference causing a stress at a point is simply the difference between the actual temperature and the average chordwise temperature.

The resulting solution for stresses due to chordwise temperature variations is

$$\sigma_{yc} = -\alpha E(T - T_m) \qquad \text{(positive when tensile)} \quad (14)$$

where

T = the average beamwise temperature at the chordwise station in question

$T_m = a + bx$ = the mean linear chordwise temperature variation that would cause deflection but no stress, evaluated at the chordwise station in question (15)

The constants a and b above are evaluated as follows:

$$a = [2mcI_1 + 4(m - n)(I_2 - I_3)]/[c^2(m + n)] \quad (16)$$

$$b = [48mcJ_1 + 96(m - n)(J_2 - J_3)]/[c^4(m + 3n)] \quad (17)$$

where

c = chord length

m = ($^1/_2$ maximum thickness of wing cross section) ÷ (chord length)

n = ($^1/_2$ leading-edge thickness of wing cross section)/(chord length)

$$I_1 = \int_{-c/2}^{c/2} T\,dx \quad (18)$$

$$I_2 = \int_{-c/2}^{0} T\,x\,dx \quad (19)$$

$$I_3 = \int_{0}^{c/2} T\,x\,dx \quad (20)$$

$$J_1 = \int_{-c/2}^{c/2} T\,x\,dx = I_2 + I_3 \quad (21)$$

$$J_2 = \int_{-c/2}^{0} T\,x^2\,dx \quad (22)$$

$$J_3 = \int_{0}^{c/2} T\,x^2\,dx \quad (23)$$

The temperatures T may be determined from the solution for combined chordwise and beamwise heat flow outlined in the preceding section, and the integrals Eqs. (18)–(23) may be evaluated by Simpson's rule or some other method of mechanical integration.

An experimental program was undertaken to verify the accuracy of this method for determining stresses in a solid diamond-shaped wing. A mild steel model wing with surface strain gages and thermocouples installed along the chord at the mid-span was used for the experiment. A nonsymmetrical chordwise temperature distribution was obtained by passing boiling water through a channel surrounding the leading edge, with cold water passing through channels at the mid-chord on the top and bottom of the wing and water at an intermediate temperature passing through a channel surrounding the trailing edge. Based on the measured temperature distribution and strain-gage readings corrected for temperature variation, excellent agreement between the stresses measured experimentally and those calculated from the theoretical solution was obtained. The details of this program, including the strain-gage calibration, are described in reference 15.

Thermal Stresses at a Sharp Leading or Trailing Edge

In the case of a wing having a sharp leading or trailing edge, the maximum stress at the leading or trailing edge may be easily calculated from Eq. (14), where T_m is equal to the initial metal temperature. This is due to the fact that the leading or trailing edge would instantly attain the adiabatic wall temperature while the rest of the wing remained at the initial wing temperature. This would be the most severe thermal stress condition possible, and the effect of leading-edge thickness on stress will be discussed in a later section of the report.

Stresses Due to Beamwise Temperature Variations

A numerical method of solution for the stresses at any point due to the beamwise temperature variations is presented in reference 6. This solution, which is based on the assumption of plane strain in elements normal to the chord shown in Fig. 1, is

$$\sigma_{yb} = -[\alpha E/(1 - \nu)](\bar{T} - \bar{T}_m) \qquad \text{(positive when tensile)} \quad (24)$$

where

$\bar{T}$ = the temperature at the point in question

$\bar{T}_m = \beta + \gamma z$ = the mean linear beamwise temperature variation that would cause deflection but no stress, evaluated at the point in question (25)

The constants β and γ have the following values:

$$\beta = \frac{1}{l}\int_{-l/2}^{l/2} \tau\,dz \quad (26)$$

$$\gamma = \frac{12}{l^3}\int_{-l/2}^{l/2} T\,z\,dz \quad (27)$$

where

l = beamwise thickness at the point in question

The temperatures $\bar{T}$ may be determined from the solution for unsymmetrical beamwise heat flow[5] and the integrals, Eqs. (30) and (31), may be evaluated by Simpson's rule or some other method of mechanical integration.

In the case when the beamwise temperatures are symmetrical about half the beamwise thickness, the temperature $\bar{T}_m$ becomes the average beamwise temperature and may be evaluated analytically.[7]

The resulting thermal stress due to both chordwise and beamwise temperature variations is the algebraic sum of Eqs. (14) and (24)—that is,

$$\sigma_{y} = \sigma_{yc} + \sigma_{yb} \tag{28}$$

Fig. 2 shows a typical stress distribution for the front half of a wing. The "average stress" shown in Fig. 2 is the stress due to the chordwise temperature variation described in the preceding section. The stress distribution for the rear half of the wing would be similar to that shown.

Discussion

The results of a number of calculations have shown that the maximum stress in the wing is a compressive stress occurring at the leading edge. At or near the leading edge, the beamwise temperature variation is so small as to be insignificant in the determination of thermal stress, indicating that Eq. (14) is sufficient for the determination of the maximum stress. This is shown graphically in Fig. 2.

In the thickest portion of the wing—that is, near the mid-chord—the beamwise temperature variation may cause appreciable stress but the magnitude of this stress is always much less than the stress at the leading edge. Further, the stresses due to the chordwise variation of the average beamwise temperatures result in a tensile stress in the region near the mid-chord, while the beamwise temperature variation itself produces compressive stresses at or near the wing surfaces and tensile stresses in the region of the center of the beamwise thickness. The algebraic sum of these two stresses as given by Eq. (28) reduces the magnitude of the surface stresses while increasing the magnitude of the stresses near the center of the beamwise thickness. This effect is also shown in Fig. 2. Due to the nature of the temperature gradients, the compressive stresses are always greater than the tensile stresses, and it is felt that the determination of stresses based on the chordwise variation of the average beamwise temperatures, Eq. (14), is adequate for the overall determination of thermal stresses from the standpoint of design. These stresses are shown as the average stresses of Fig. 2.

Due to the fact that the heat-transfer coefficient at the leading edge is greater than that at the trailing edge, for wings having finite leading- and trailing-edge thicknesses, the maximum transient stress will occur at the leading edge. At some later time, however, the trailing-edge stress may be greater than the leading-edge stress at the same time. The effect of sharp leading or trailing edges has been previously discussed.

Investigation of the Effect of Flight Conditions on Thermal Stresses

The methods of calculating temperature distributions and thermal stresses previously discussed were used in an investigation to determine the effect of variation in important flight conditions on thermal stresses.

The stress magnitudes presented in the following sections are extremely high, and, in general, buckling of the leading edge would occur before the stresses were attained. It should be remembered, however, that the stress conditions investigated resulted from an assumed infinite acceleration to the given flight condition and thus represent the most severe thermal stress condition possible.

The stress magnitudes are significant in that they represent the values that the stresses would tend to approach if the wing material did not buckle. It is believed that the variations in stress presented are representative in showing the general trends caused by variation in the various flight and configuration conditions.

The Effect of Angle of Attack

To determine the effect of angle of attack on thermal stresses, the wing was assumed to be at a Mach Number of 4 at 60,000 ft. standard altitude having an initial uniform temperature of 393°R. The chordwise variation in heat-transfer coefficients for the upper and lower wing surfaces as calculated by Eq. (2) for angles of attack of 0°, 2°, 4°, and 6° are shown in Fig. 3. The chordwise temperature distributions for the various angles of attack were determined over a sufficient time period for the maximum stress to occur. These calcula-

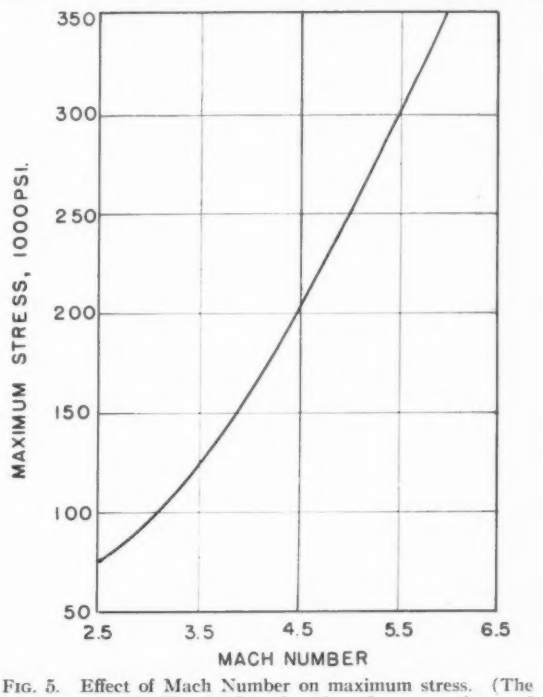

FIG. 5. Effect of Mach Number on maximum stress. (The results presented in Figs. 5–12 are based on the assumptions and flight conditions given in the section on Basic Conditions and Assumptions.)

tions showed the maximum stresses to be unaffected by a variation in angle of attack. Calculations also showed that the average beamwise stress at any chordwise station was independent of angle of attack.

In Fig. 3 the heat-transfer coefficient is seen to vary by a factor of approximately 2 for an angle of attack variation of 0°–6°. The reason this variation in heat-transfer coefficient has no appreciable effect on the maximum stress at the leading edge may be explained briefly as follows:

For wings with finite leading-edge thickness, with the passage of time the leading-edge stress will first increase, pass through a maximum, and later decrease as thermal equilibrium is approached. The greater the heat-transfer coefficient, the sooner will the maximum stress occur. However, in the case of a sharp leading edge, the heat-transfer coefficient does not enter into the equation for maximum stress in any way. Thus for a leading edge that is extremely thin, it is not surprising that the heat-transfer coefficient has no appreciable effect on the value of the maximum stress, although it does affect the time at which the maximum stress occurs. Further effects of time on maximum stress are discussed in a later section.

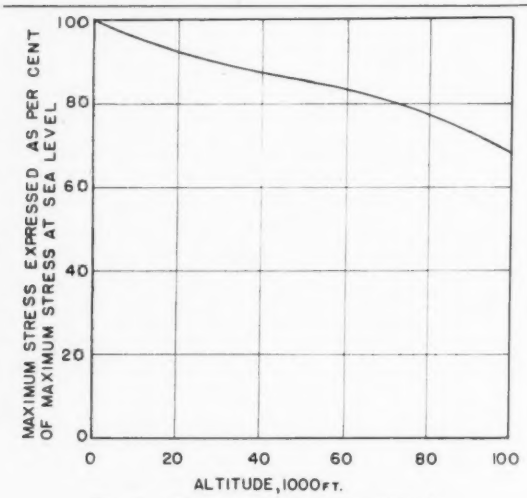

FIG. 6. Maximum stress versus altitude.

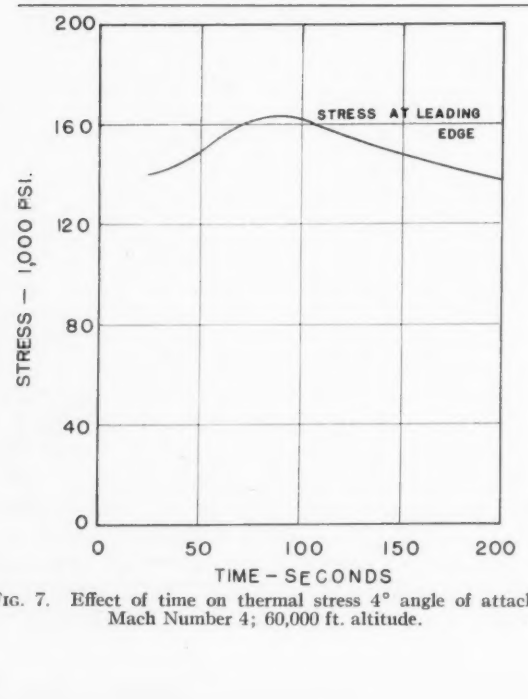

FIG. 7. Effect of time on thermal stress 4° angle of attack, Mach Number 4; 60,000 ft. altitude.

The Effect of Mach Number and Velocity

To determine the effect of Mach Number on thermal stresses, the wing was assumed to be at zero angle of attack having an initial uniform temperature of 393°R. at 60,000 ft. altitude. The chordwise variations in heat-transfer coefficient for this condition are shown in Fig. 4 for Mach Numbers of 2.5, 4, and 6, corresponding to velocities of 1,658, 2,650, and 3,970 m.p.h.

The chordwise temperature distributions for the various Mach Numbers were determined over a sufficient time period for the maximum stresses to occur. The resulting variation in maximum stresses occurring at the leading edge plotted versus Mach Number and velocity are shown in Fig. 5.

As shown in Fig. 5, the maximum stress increases rapidly with Mach Number and velocity, being 4.78 times as great at $M = 6$ as at $M = 2.5$.

The Effect of Altitude

To determine the effect of altitude on thermal stresses, the wing was assumed to be at zero angle of attack having an initial temperature of 530°R. and suddenly subjected to a Mach Number of 4. In order to simplify the calculations, an average value of heat-transfer coefficient as calculated from Eq. (2) was used at each altitude. The chordwise temperature distributions for altitudes of 0, 20,000, 40,000, 60,000, and 100,000 ft. were calculated over a sufficient time for the maximum stress to occur. The resulting variation in maximum stress occurring at the leading edge plotted versus altitude is shown in Fig. 6.

As shown in Fig. 6, the maximum stress decreases somewhat with an increase in altitude, being 1.47 times as great at sea level as at 100,000 ft., again indicating that the magnitude of the heat-transfer coefficient has little effect on the maximum thermal stress. The magnitude of the heat-transfer coefficient does have a great effect on the time at which the maximum thermal stress occurs, as will be discussed in the following section.

The Effect of Time

Since all problems investigated in this study are based on transient-state heat transfer, time is an important variable. In general, the effect of time on the stresses at any point in the wing is that the stress increases with time to some maximum value and then de-

creases approaching zero at infinite time. A typical variation of stress with time is shown in Fig. 7. The conditions chosen for this figure are for a Mach Number of 4 at 60,000 ft. at 4° angle of attack. The stresses plotted are the leading-edge stresses.

Variation in the flight conditions or wing configuration also affects the time at which the maximum stress occurs. As an example, Fig. 8 shows the time required to attain the maximum stress for various altitudes based on the conditions of the preceding section. As shown in Fig. 8, the maximum stress at sea level occurred 46.7 sec. after the wing was subjected to the flight Mach Number, while the time required at 100,000 ft. was 1,480.1 sec. This effect is due primarily to the large reduction in heat-transfer coefficient with increasing altitude.

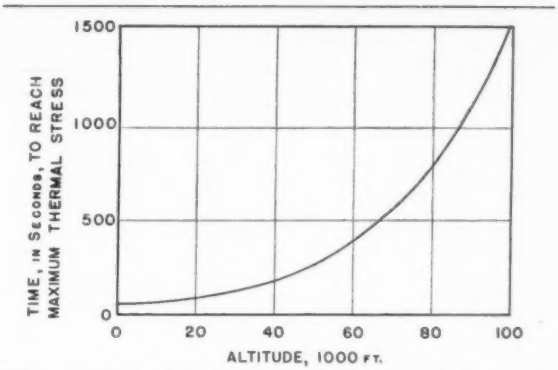

FIG. 8. Time required to attain maximum thermal stress as a function of altitude.

INVESTIGATION OF THE EFFECT OF CONFIGURATION CONDITIONS ON THERMAL STRESSES

The methods of calculating temperature distributions and thermal stresses previously discussed were used in an investigation to determine the effect of variation in important wing configuration conditions on thermal stresses. The purpose of this investigation was to compare the effects of certain conditions and not to establish accurate stress magnitudes. For this reason, an average value of heat-transfer coefficient was used for all calculations except those for the effects of solidity on stress.

The Effect of Leading-Edge Thickness

To determine the effect of leading-edge thickness, the airfoil was assumed to be a Mach Number of 4 at 20,000 ft. with 530°R. initial temperature. The temperatures were calculated over a time range sufficient to determine the maximum stress for an average value of heat-transfer coefficient based on Eq. (2).

The leading-edge thickness was considered as a variable, and maximum stresses were determined as a function of leading-edge thickness for values of leading-edge thickness from 0–0.1 ft., corresponding to leading-edge-to-maximum thickness ratios of 0–50 per cent. The results of this investigation are shown in Fig. 9.

As shown by Fig. 9, the maximum stress is greatly affected by leading-edge thickness. With a leading edge 20 per cent of the maximum thickness, the maximum stress is only 38 per cent of that for a sharp leading edge. With a leading-edge thickness 5 per cent of the maximum thickness, the maximum stress is 68 per cent of that for a sharp leading edge.

It should be remembered that this curve is based on a specific wing having a 4-ft. chord and 0.2-ft. maximum thickness. The results should be considered to represent a trend rather than as a guide to absolute values. Subsequent investigations showed that the leading-edge thickness has a much greater effect on stress than do the chord length, thickness ratio, or span, as will be discussed in the following sections.

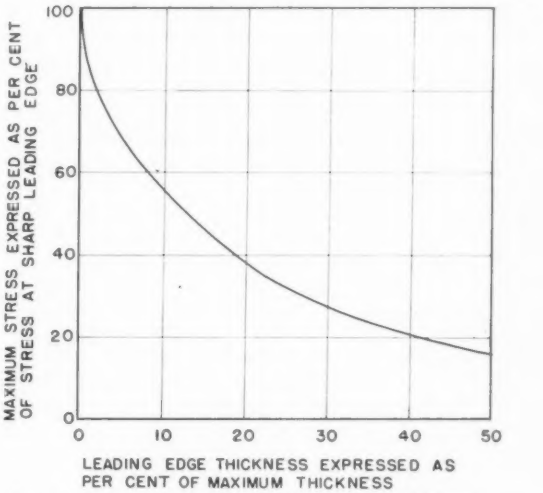

FIG. 9. Maximum stress versus leading-edge thickness.

The Effect of Chord Length

To determine the effect of chord length, the airfoil was assumed to be at a Mach Number of 4 at 20,000 ft. altitude with 530°R. initial temperature. The temperatures were calculated over a sufficient time range to determine the maximum stress with an average value of heat-transfer coefficient based on Eq. (2).

The chord length was considered as a variable with a constant leading-edge thickness-to-maximum thickness ratio and maximum thickness-to-chord ratio. That is, cross sections remained geometrically similar. Maximum stresses were determined as a function of chord length for values of chord length from 3 to 7 ft. The results of this investigation showed the maximum stress to be unaffected by a variation in chord length based on the above conditions. The time at which the maximum

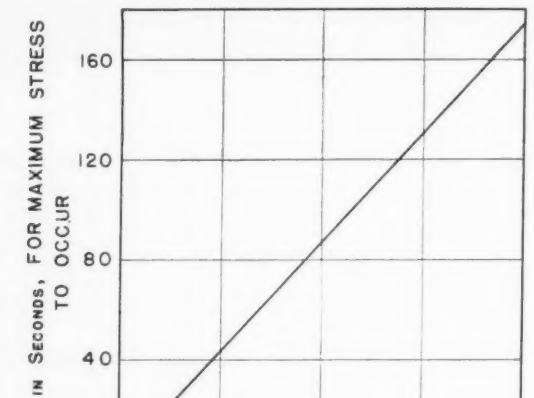

FIG. 10. Time required to attain maximum stress as a function of chord length.

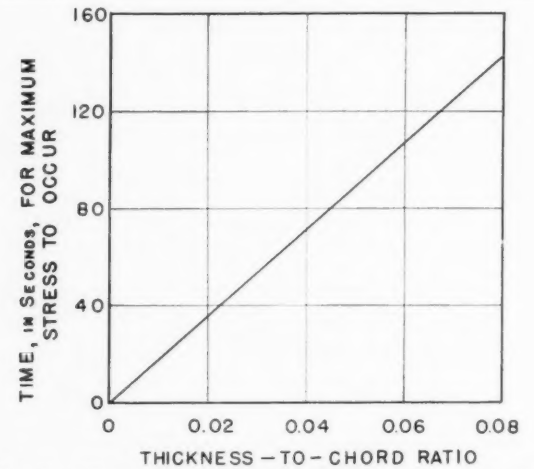

FIG. 11. Time required to attain maximum stress as a function of thickness-to-chord ratio.

stress occurs, however, increases with increasing chord length as shown in Fig. 10.

The Effect of Thickness-Chord Ratio

To determine the effect of the thickness-to-chord ratio, the airfoil was assumed to be at a Mach Number of 4 at 20,000 ft. altitude with 530°R. initial temperature. The temperatures were calculated over a sufficient time range to determine the maximum stress with an average value of heat-transfer coefficient based on Eq. (2).

The maximum thickness-to-chord ratio was considered as a variable with a constant leading-edge thickness-to-maximum thickness ratio and chord length. Maximum stresses were determined as a function of thickness-to-chord ratio for values of 1, 4, 5, 6, and 8 per cent. The results of this investigation showed the maximum stress to be unaffected by a variation in thickness-to-chord ratio in the range of values investigated. As in the case of variable chord length, the time at which the maximum stress occurs increases with increasing thickness-to-chord ratio as shown in Fig. 11.

The Effect of Span and Taper

An investigation of combined chordwise, beamwise, and spanwise heat flow given in reference 4 showed that spanwise heat flow had a negligible effect on the chordwise variation of the average beamwise temperature, even in the case of a wing having a two-to-one taper. Later, calculations for a wing with three-to-one taper also showed that spanwise heat flow had a negligible effect on the chordwise variation of the average beamwise temperature.

As a result, it was found that the maximum thermal stress was unaffected by span or taper for wings in the taper range of one-to-one to three-to-one. For the tapered wings, the time required to attain maximum stress was less in the region near the tip than that for the region near the root. It should be remembered, however, that the method for solution of thermal stresses was limited to the region of the wing one chord length or more from the wing tip, since St. Venant's principle was applied in the development of the stress calculation methods.

The Effect of Sweep

All the solutions presented for stress are based on the simplifying assumption that the wing is unrestrained. Therefore, by choosing the spanwise or y direction parallel to the mean angle of sweep and the chordwise or x direction normal to the spanwise direction, the methods of solution may be applied directly to swept-back wings.

It was felt unnecessary, however, to perform calculations to determine the effect of sweep in view of the results of the preceding sections on the variation of chord length, thickness-to-chord ratio, and span. The effect of sweep is to change the chord length, thickness-to-chord ratio, and span slightly, and small changes in these parameters have been shown to have negligible effects on maximum thermal stresses.

The Effect of Solidity

To determine the effect of solidity, the basic wing was assumed to be at a Mach Number of 4 at 60,000 ft. altitude with zero angle of attack. The solidity was varied by considering wings having sections removed from the center of the cross section which were geometrically similar to the wing cross section as shown in Fig. 12. A solidity ratio was defined as the maximum thickness of the cross section minus the maximum thickness of the section removed, all divided by the maximum thickness of the cross section. That is

$$\text{Solidity ratio} = (t - t')/t \qquad (29)$$

where

t = the maximum thickness of the cross section
t' = the maximum thickness of the section removed

The solidity ratio was varied from unity (solid wing) down to 0.125. The temperatures were determined based on the assumption that the air inside the wing would instantaneously attain the inner surface temperature at any chordwise station. A sufficient time range was covered to obtain the maximum stress at the leading edge. Thermal stresses were calculated by the method of reference 3, since the method of reference 6 previously presented applies only to a solid, diamond-shaped wing. Fig. 12 shows the variation in maximum stress with increasing solidity ratio.

As shown in Fig. 12, the maximum stress is greatly reduced for wings of low solidity ratio, being only 48 per cent as great for a solidity ratio of 0.125 as for a solid wing. Calculations also showed that the maximum tensile stress in the region of the mid-chord was appreciably reduced with decreasing solidity ratio.

The results of this investigation indicate that a hollow wing of low solidity would be greatly superior to a solid wing from the standpoint of thermal stresses.

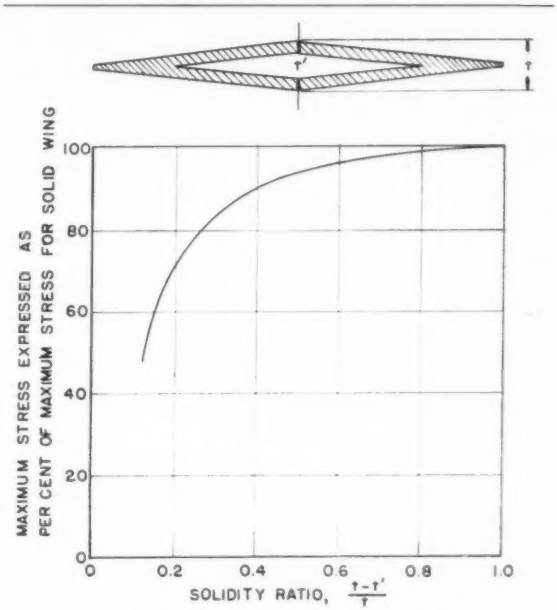

FIG. 12. Effect of solidity on maximum stress.

CONCLUSIONS

(1) The maximum thermal stress, which is compressive, occurs at the leading or trailing edge of the wing and can be determined from a one-dimensional solution for the chordwise variation of the average beamwise temperature.

(2) For the limiting case of infinite acceleration to a steady flight Mach Number greater than two, the leading-edge stresses for the chosen configuration would be prohibitive from the standpoint of exceeding the critical buckling stress.

(3) The tensile stresses of greatest magnitude occur in the region of the wing near the beamwise center of the mid-chord. These stresses are much smaller than the compressive stresses at the leading or trailing edge.

(4) Thermal stresses increase rapidly with increasing Mach Number (see Fig. 5).

(5) Thermal stresses may be reduced appreciably by increasing the leading-edge (and trailing-edge) thickness (see Fig. 7).

(6) A hollow wing of low solidity is greatly superior to a solid wing from the standpoint of thermal stress (see Fig. 12).

(7) Thermal stresses decrease somewhat with increasing altitude (see Fig. 6).

(8) The following variables have no appreciable effect on maximum thermal stresses: angle of attack, chord length, thickness-to-chord ratio, length of span, taper, and sweep.

REFERENCES

[1] Johnson, H. A., Rubesin, M. W., Sauer, F. M., Slack, E. G., and Possner, L., *A Design Manual for Determining the Thermal Characteristics of High Speed Aircraft*, AAF-TR5632, U.S.A.F., Air Materiel Command, September, 1947.

[2] Humble, L. V., Lowdermilk, W. H., and Grele, M., *Heat Transfer from High Temperature Surfaces to Fluids—Part I*, N.A.C.A. R.M. No. E7L31, May 21, 1948.

(*References 3–16 inclusive comprise a portion of the U.S.A.F. Technical Report No. 6351—Part II, to be published*)

[3] Brull, M. A., *Thermal Stresses in a Solid Supersonic Wing*, Report I, Contract W33-038-ac-17240 (17767), Engineering Experiment Station, University of Colorado.

[4] Brull, M. A., *Determination of the Temperature Distribution in a Solid Diamond-Shaped Wing in Supersonic Flight, Considering Chordwise and Spanwise Heat Flow Only*, Report IV, Contract W33-038-ac-17240 (17767), Engineering Experiment Station, University of Colorado.

[5] Brull, M. A., *Determination of the Temperature Distribution in a Solid Diamond-Shaped Wing in Supersonic Flight, Considering Beamwise Heat Flow Only, With Unsymmetrical Conditions at the Boundaries*, Report VIII, Contract W33-038-ac-17240 (17767), Engineering Experiment Station, University of Colorado.

[6] Brull, M. A., *A Method for the Determination of Thermal Stresses in a Solid Supersonic Wing, Considering Chordwise and Beamwise Temperature Gradient*, Report XI, Contract W33-038-ac-17240 (17767), Engineering Experiment Station, University of Colorado.

[7] Durham, F. P., *Determination of Temperature Distribution in a Solid Diamond-Shaped Wing in Supersonic Flight, Beamwise Heat Flow Only*, Report V, Contract W33-038-ac-17240 (17767), Engineering Experiment Station, University of Colorado.

[8] Durham, F. P., *Determination of Temperature Distribution in a Solid Diamond-Shaped Wing in Supersonic Flight, Combined Chordwise and Beamwise Heat Flow (Symmetrical Beamwise)*, Report VI, Contract W33-038-ac-17240 (17767), Engineering Experiment Station, University of Colorado.

[9] Durham, F. P., *Correlation of Temperature Distribution in a Solid Diamond-Shaped Wing in Supersonic Flight As Calculated by*

One-Dimensional Beamwise Method and As Calculated by Two-Dimensional Chordwise and Beamwise Method, Report VII, Contract W33-038-ac-17240 (17767), Engineering Experiment Station, University of Colorado.

[10] Durham, F. P., *Determination of Temperature Distribution in a Solid Diamond-Shaped Wing in Supersonic Flight, When Both Chordwise and Beamwise Heat Flow Are Unsymmetrical*, Report IX, Contract W33-038-ac-17240 (17767), Engineering Experiment Station, University of Colorado.

[11] Maydew, R. C., and Durham, F. P., *The Effect of Significant Parameters on Thermal Stresses in a Solid Diamond-Shaped Supersonic Wing*, Report II, Contract W33-038-ac-17240 (17767), Engineering Experiment Station, University of Colorado.

[12] Maydew, R. C., *Determination of Temperature Distribution in a Solid Diamond-Shaped Wing in Supersonic Flight, Chordwise Heat Flow Only (Skretting Method)*, Report III-a, Contract W33-038-ac-17240 (17767), Engineering Experiment Station, University of Colorado.

[13] Maydew, R. C., *Determination of Temperature Distribution in a Solid Diamond-Shaped Wing in Supersonic Flight, Chordwise Heat Flow Only (Sibert Method)*, Report III-b, Contract W33-038-ac-17240 (17767), Engineering Experiment Station, University of Colorado.

[14] Stephenson, F. A., and Arnberg, B. T., *Experimental Determination of Temperature As a Function of Time in a Solid Rectangular Block, Beamwise Heat Flow Only*, Report E-III, Contract W33-038-ac-17240 (17767), Engineering Experiment Station, University of Colorado.

[15] Stephenson, F. A., and Arnberg, B. T., *Experimental Determination of Thermal Stresses in Rectangular Plates and Diamond-Shaped Wings As a Function of Chordwise Temperature Distribution*, Report E-VI, Contract W33-038-ac-17240 (17767), Engineering Experiment Station, University of Colorado.

[16] Stephenson, F. A., and Arnberg, B. T., *Experimental Determination of Temperature Distribution in a Solid Diamond-Shaped Wing*, Report E-VII, Contract W33-038-ac-17240 (17767), Engineering Experiment Station, University of Colorado.

Effect of Turbulence Level of Incident Air Stream on Local Heat Transfer and Skin Friction on a Cylinder

(*Continued from page 730*)

physical point of view, so the curve of Fig. 10 was used instead. This type of a plot brings out the fact that the pressure reading of a surface tube is due to combined viscous and inertia forces, the relative contributions of each depending on the fluid flowing and on the physical dimensions of the tube.

The points on Fig. 10 used to establish the calibration curve were determined from pressure measurements made in the laminar boundary-layer region and using the Blasius-Hiemenz boundary-layer solution. Agreement between the skin friction in the laminar boundary-layer region calculated from this curve and that determined from the Blasius-Hiemenz method was within 12 per cent for most of the data taken, and it is felt that this is about the best accuracy that should be claimed for the skin-friction curves in general.

Shear Center for Thin-Walled Open Sections Beyond the Elastic Limit

(*Continued from page 754*)

Conclusion

The methods outlined above can be used to find the position of the shear center for thin-walled sections. It should be emphasized that the shear center is no longer a section property but depends for its location on the load and the stress-strain curve. Furthermore, while it has been shown that in the *elastic* case[6] a load acting on such a section can be replaced by a shear load at the shear center and a torque with reasonable accuracy, it still remains to be studied whether this is true *beyond the elastic limit*. Consequently, it is still an open question whether the results given in this paper can be used for such a purpose.

References

[1] Timoshenko, S. P., *Strength of Materials*, Part II, 2nd Ed., p. 52; D. Van Nostrand Company, Inc., 1941; also Sechler, E. E., and Dunn, L. G., *Airplane Structural Analysis and Design*, p. 109; John Wiley & Sons, New York, 1942.

[2] Nadai, A., *Plasticity, a Mechanics of the Plastic State of Matter*, p. 160; McGraw-Hill Book Company, Inc., New York and London, 1931.

[3] Timoshenko, S. P., *loc. cit.*, Part I, p. 170.

[4] Timoshenko, S. P., *Theory of Bending, Torsion and Buckling of Thin-Walled Members of Open Cross Section*, Journal of the Franklin Institute, Vol. 239, p. 206, 1945.

[5] Timoshenko, S. P., *loc. cit.*, p. 209.

[6] Hadji-Argyris, J., and Dunne, P. C., *The General Theory of Cylindrical Tubes Under Torsion and Bending Loads*, Jour. Roy. Aero. Soc., Vol. 51, pp. 199–269, 1946.

Readers' Forum

BRIEF REPORTS of investigations in the aeronautical sciences and discussions of papers published in the JOURNAL are presented in this special department. Publication will be completed approximately 8 to 10 weeks after receipt of the material. The Editorial Committee does not hold itself responsible for the opinions expressed by the correspondents. Contributions should not exceed 800 words in length.

A Simple Graphical Method for Constructing Families of Nyquist Diagrams*

Robert M. Stewart†
Jet Propulsion Laboratory, California Institute of Technology
July 20, 1951

(I) Introduction

In reference 1, an outline is given of the widely used frequency-response method of analysis of aircraft-autopilot stability. By means of this method, it is possible to determine the stability of an automatically controlled aircraft from measured autopilot characteristics and calculated aircraft characteristics. The criterion used in interpreting frequency-response data is the Nyquist criterion or variations of it. It is sometimes necessary to make a comprehensive survey of aircraft stability over widely varying conditions of operation, with possible variations in aircraft configuration and with various combinations of control-system parameters. It is the purpose of this note to describe a simple graphical aid to constructing such families of diagrams. An example is given concerning a system whose control-system response is a function of two parameters. It is assumed that these parameters correspond to physical characteristics of the equipment which are accessible for change and adjustment. It is then shown that, with other conditions remaining unchanged, Nyquist diagrams corresponding to *any* combination of values of these two parameters can be constructed using only a straightedge and dividers after four Nyquist diagrams have been determined in the usual manner corresponding to four combinations of the two parameters.

(II) Form of Basic Stability Equations

Following reference 1, let

$$\theta = (\theta/\delta)_A(p)\cdot\delta \tag{1}$$

define the calculated aircraft transfer function and

$$\delta = (\delta/\theta)_C(p)\cdot\theta \tag{2}$$

define the measured control-system transfer function. The characteristic equation of the system, whose roots indicate the stability and transient response of the system, is given by the simultaneous solution of Eqs. (1) and (2)

$$(\theta/\delta)_A(p)\cdot(\delta/\theta)_C(p) = 1 \tag{3}$$

Hence, stability is determined by the relationship of the contour

$$G(j\omega) = -(\theta/\delta)_A(j\omega)\cdot(\delta/\theta)_C(j\omega) \tag{4}$$

to the point $(-1, j0)$. Many common types of control systems are so arranged that it is known that their transfer function is of the form

$$(\delta/\theta)_C(j\omega) = [g_0(j\omega) + K_1g_1(j\omega) + K_2g_2(j\omega) + K_1K_2g_{12}(j\omega)] \tag{5}$$

where K_1 and K_2 are pertinent control-system parameters. Thus, the function that is mapped is of the form

$$G(j\omega) = -(\theta/\delta)_A(j\omega)\cdot[g_0(j\omega) + K_1g_1(j\omega) + K_2g_2(j\omega) + K_1K_2g_{12}(j\omega)] \tag{6}$$

(III) Properties of $G(K_1, K_2)$

Now consider G as a function of K_1 and K_2. If ω and K_2 are constants and if we let

$$\left.\begin{aligned} x &= [G(j\omega)]_{\text{real}} \\ y &= [G(j\omega)]_{\text{imaginary}} \end{aligned}\right\} \tag{7}$$

then

$$\left.\begin{aligned} x &= a_1 + b_1K_1 \\ y &= a_2 + b_2K_1 \end{aligned}\right\} \tag{8}$$

where a_1, a_2, b_1, and b_2 are real constants, or

$$y = c + dx \tag{9}$$

where c and d are real constants. Thus, if K_2 is a constant and if we vary K_1, lines of constant ω are straight lines. Furthermore, from Eq. (8),

$$\Delta x/\Delta K_1 = b_1, \qquad \Delta y/\Delta K_1 = b_2 \tag{10}$$

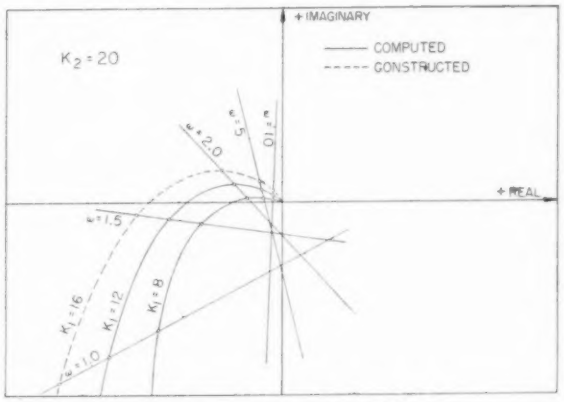

FIG. 1. $G(j\omega)$ for $K_2 = 20$.

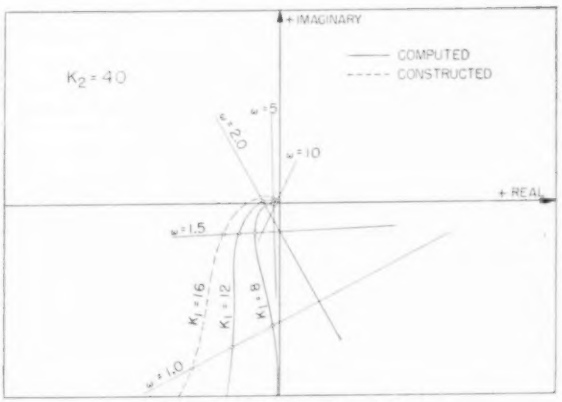

FIG. 2. $G(j\omega)$ for $K_2 = 40$.

* This paper presents the results of one phase of research carried out at the Jet Propulsion Laboratory, California Institute of Technology, under Contract DA-94-495-ORD 18, sponsored by the Department of the Army, Ordnance Corps.

† Research Engineer, Systems Analysis Group, Guidance and Control Section.

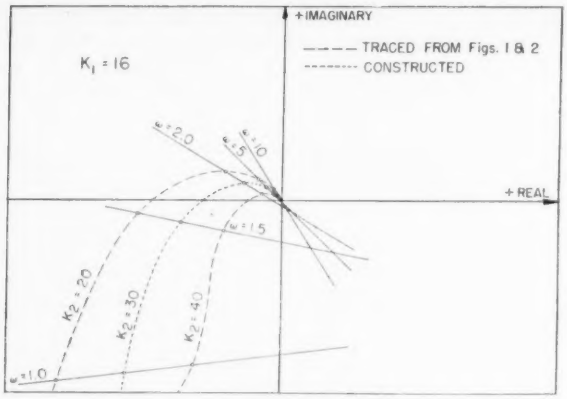

FIG. 3. $G(j\omega)$ for $K_1 = 16$.

or if

$$\Delta s = (\Delta x^2 + \Delta y^2)^{1/2} \tag{11}$$

then

$$\Delta s = (b_1^2 + b_2^2)^{1/2} \cdot \Delta K_1 \tag{12}$$

or

$$\Delta s = (\text{constant}) \cdot \Delta K_1 \tag{13}$$

which means that along these lines of constant ω the displacement of the locus of $j\omega$ is proportional to the change in gain. Similar results are obtained if we let K_1 be constant and vary K_2.

It is now possible by simple construction to obtain the stability diagram for any combination of K_1 and K_2 after we have computed and plotted four loci. This construction is illustrated in Figs. 1, 2, and 3.

In Fig. 1, we have mapped the locus of $j\omega$ for

$$K_2 = 20, \quad K_1 = 8$$
$$K_2 = 20, \quad K_1 = 12$$

From these two curves we can readily obtain the plot corresponding to $K_2 = 20$ and any desired value of K_1. The plot corresponding to $K_1 = 16$ is shown as an illustration. In Fig. 2, we have mapped the locus of $j\omega$ for

$$K_2 = 40, \quad K_1 = 8$$
$$K_2 = 40, \quad K_1 = 12$$

From these two curves we can readily obtain the plot corresponding to $K_2 = 40$ and any desired value of K_1.

Suppose that the plot for $K_2 = 30$ and $K_1 = 16$ is desired. First, the plot for $K_2 = 40$ and $K_1 = 16$ was constructed as shown in Fig. 2. Then the two plots (from Figs. 1 and 2) corresponding to $K_1 = 16$ were traced on Fig. 3. Now by the same procedure as before, we obtain the plot for $K_1 = 16$ and any desired value of K_2. The construction of the curve corresponding to $K_1 = 16$ and $K_2 = 30$ is shown.

(IV) Conclusion

In general, if it is desired to apply this procedure to the effect of n variable parameters, it is necessary first to compute and map 2^n fundamental contours. The procedure is obviously applicable to electronic and other systems that are susceptible to analysis by means of the Nyquist criterion and to the analysis of the effect on stability in aircraft of inertial and aerodynamic parameters. Some manipulation is required in certain cases in order to obtain a function that will determine stability and at the same time be of the form of Eq. (6) with respect to the lumped parameters that are to be varied. Typical cases of aircraft control to which the method is particularly adaptable are (a) combination rate and position gyro control and (b) combination ground station and internal control.

Reference

[1] Seacord, Charles L., *Application of Frequency-Response Analysis to Aircraft-Autopilot Stability*, Journal of the Aeronautical Sciences, Vol. 17, No. 8, pp. 481–498, August, 1950.

Strength of Reflected Shock in Mach Reflection*

H. S. Tan
Cornell University
July 13, 1951

When a propagating plane shock is diffracted by a corner, Mach reflection is set up, the situation after passage of the wave being as sketched in Fig. 1. The reflected front R is an acoustic wave, according to first-order theory.[1–3] However, results of first-order theory can be used to determine more accurately the strength of this wave, and it will be shown here that this is in fact a shock of second-order strength. The case of extremely weak incident shock was studied by Bargmann,[1] where vorticity in region OTP was neglected. The present investigation, however, is not limited in incident shock strength. Lighthill's first-order pressure solution[3] and his technique[4] for finding the shock strength have been used. The latter is essentially a process of pushing away the apparent singularity appearing in the differential equation of motion due to its linearization.

Since for small ϑ the flow behind straight shock DT and slip stream S is irrotational [vorticity $\Omega < O(\vartheta^3)$], we can introduce a velocity potential Φ which, because of its conical property in time-space, further reduces to the form

$$\Phi(\bar{r}, \theta, t) = a_1^2 t f(r, \theta) \tag{1}$$

in a coordinate system fixed to flow 1, with origin at the disturbance center O, and $a_1 = \gamma p_1/\rho_1$, $r = \bar{r}/a_1 t$.

Denoting partial derivatives by subscripts and the radial and tangential velocity components by u, v we have

$$u = \Phi_{\bar{r}} = a_1 f_r$$
$$u_t = -(a_1 r/t) f_{rr}$$
$$v = (1/r)\,\Phi_\theta = (a_1/r)\, f_\theta$$
$$v_t = -(a_1 r/t)\,[-(f_\theta/r^2) + (1/r) f_{r\theta}]$$

and

$$\Phi_t = a_1^2 (f - r f_r)$$
$$\nabla_r^2 \Phi = (1/t) \nabla_r^2 f$$
$$\Phi_{tt} = (a_1^2 r^2/t) f_{rr}$$

On introducing these relations into the equations of motion,

$$\Phi_t + \frac{1}{2}(u^2 + v^2) + \frac{a^2}{\gamma - 1} = \frac{a_1^2}{\gamma - 1} \tag{2}$$

$$a^2 \nabla_r^2 \Phi = \Phi_{tt} + 2u_i \frac{\partial u_i}{\partial t} + u_i u_j \frac{\partial u_i}{\partial x_j} \tag{3}$$

and eliminating a/a_1, the following result is obtained:

$$\left[1 - r^2 - (\gamma - 1)\left(f + \frac{1}{2}\frac{1}{r^2} f_\theta^2\right) + (\gamma + 1) \times \left(r f_r - \frac{1}{2} f_r^2\right)\right] f_{rr} + (\text{additional terms in } f_{r\theta} \text{ and } f_{\theta\theta}) = 0 \tag{4}$$

* This investigation has been part of a research project sponsored by the U.S. Air Force, Office of Air Research, at the Graduate School of Aeronautical Engineering, Cornell University. A more detailed account has been submitted to that Office for publication as an Air Force report.

where additional terms, not explicitly required here, have not been written out.

Referring to coordinates fixed to the shock, the Rankine-Hugoniot conditions can be written

$$\left.\begin{array}{ll} \text{(a)} & q^{(t)} \text{ continuous} \\ \text{(b)} & \Delta q^{(n)} = [2/(\gamma+1)]\,[(a^2/q^{(n)}) - q^{(n)}] \end{array}\right\} \quad (5)$$

where $q^{(t)}$ and $q^{(n)}$ denote velocity components tangential and normal to the shock, respectively, and $\Delta(\ )$ denotes the increase of a quantity across the shock front. Now, since Φ exists and the flow is stationary in the (r, θ) plane, let the reflected shock front be $r = \eta(\theta)$; then

$$q^{(t)} = \frac{f_\theta + \eta'(\theta)\,(f_r - \eta)}{r\sqrt{1 + r^{-2}\eta'^2}}\,a_1$$

$$q^{(n)} = \frac{-(f_r - \eta) + r^{-2}\eta' f_\theta}{\sqrt{1 + r^{-2}\eta'^2}}\,a_1$$

$$\Delta\,[f_\theta + \eta'(\theta)\,(f_r - \eta)] = 0$$

So

$$\Delta q^{(n)} = \frac{-\Delta f_r - r^{-2}\eta'^2\,\Delta f_r}{\sqrt{1 + r^{-2}\eta'^2}}\,a_1 = -\sqrt{1 + r^{-2}\eta'^2}\,a_1\,\Delta f_r$$

and we have, finally,

$$\Delta f_r = \frac{2}{\gamma+1}\,[(\gamma-1)(f - rf_r) - 2f_r + 2(\eta - 1)],$$

$$\Delta f = 0 \quad (6)$$

Following Lighthill,[4] we imagine both r and f expanded in series of terms of ascending order:

$$\left.\begin{array}{l} r = R + r(\theta) = R + r_1(\theta) + r_2(\theta) + \ldots \\ f = f_1(R, \theta) + f_2(R, \theta) + \ldots \end{array}\right\} \quad (7)$$

Then f_1 is the familiar linearized result. The process of successive calculation of $r_1, r_2, \ldots$ should be thought of as a process of successive pushing away of the apparent singularity that appears at $R = 1$ in the approximate equations. Lighthill has pointed out that, physically, the process amounts to applying the results of linearized theory at an improved location in the field. Since $f_1 = f_{1R} = 0$ on $R = 1$, $f_{1R} \sim A(\theta)\sqrt{1 - R}$ as $R \to 1$ in linearized theory, and

$$\frac{p - p_1}{\rho_1 U^2} = -\frac{\Phi_t}{U^2} = \frac{-f + rf_r}{M_1^2} = A(\theta)\sqrt{1 - R},$$

$$R \to 1 \quad (8)$$

So

$$f_{1R} = M_1^2 A(\theta)\sqrt{1 - R} \quad (9)$$

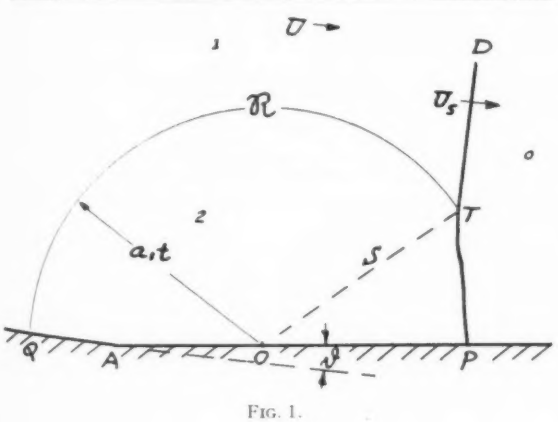

FIG. 1.

Now if Eq. (7) is put into Eq. (4), and we collect terms of the second order, we obtain a differential equation for $f_2(R, \theta)$. Here a term in f_{1RR} appears, and this derivative is infinite at $R = 1$. To avoid infinite f_{2R}, we must choose $r_1(\theta)$ to make the coefficient of f_{1RR} vanish at $R = 1$. The result is $r_1(\theta) \equiv 0$; i.e., no first-order difference between r and R is required in this case. Evaluating the limiting value of this f_{1RR} term as $R \to 1$, we can use the differential equation to calculate $(f_{2R})_{R=1}$; the result is

$$(f_{2R})_{R=1} = [(\gamma+1)/2]\,M_1^4 A^2(\theta) \quad (10)$$

We proceed to find $r_2(\theta)$ by a similar process to that used for $r_1(\theta)$; viz., to make the coefficient of f_{RR} in the differential equation for $f_2(R, \theta)$ vanish at $R = 1$. We find

$$r_2(\theta) = [(\gamma+1)^2/4]\,M_1^4 A^2(\theta) \quad (11)$$

The shock wave is now to be fitted into the region of validity of our results, which we have established to second order. The shock conditions [Eq. (6)] at $r = \eta(\theta)$ are: Since $f = 0$ ahead of shock, so directly behind it

$$f = 0, \qquad f_R = 4(\eta - 1)/(\gamma + 1) \quad (12)$$

The shock comes in the range $R < 1$, and $\eta - 1\ (= \eta_2$, say) is of second order. The first condition [Eq. (12)] is satisfied by Taylor expansion about $R = 1$ to the second order and tells us only that $f_2 = 0$ at $R = 1$ [as has already been assumed in getting Eq. (11)]. The second condition [Eq. (12)] involves two second-order terms; namely, $(f_{2R})_{R=1}$ and the contribution of f_{1R}, which is $M_1^2 A(\theta)\sqrt{r_2 - \eta_2}$. Thus, the second shock condition leads to

$$\left.\begin{array}{ll} \eta_2 = (3/16)\,(\gamma+1)^2 M_1^4 A^2(\theta) & \text{if } A(\theta) > 0 \\ = 0 & \text{if } A(\theta) < 0 \end{array}\right\} \quad (13)$$

For the case of diffraction by a concave corner, as in Fig. 1, $A(\theta) > 0$, and the shock is located at

$$r = 1 + (3/16)\,(\gamma+1)^2 M_1^4 A^2(\theta) \quad (14)$$

Now the pressure change across the shock is

$$\rho_1 \Phi_t = \frac{\rho_1 U^2}{M_1^2}\,(rf_r - f) = \frac{3}{4}\,\gamma(\gamma+1) M_1^4 A^2(\theta)$$

So the shock strength is given by

$$\frac{\Delta p}{p_1} = \frac{4\gamma U^2}{(\gamma+1) M_1^2 a_1^2}\,\eta_2(\theta) = \frac{3}{4}\,\gamma(\gamma+1) M_1^4 A^2(\theta) \quad (15)$$

where

$$A(\theta) = \lim_{r \to 1}\,[(p - p_1)/\rho_1 U^2 \sqrt{1 - r}\,] \quad (16)$$

on linear theory.

This limit as given by reference 3 is of the form

$$A(\theta) = (\text{function of } \theta) \times \vartheta = K(\theta)\vartheta, \text{ say} \quad (17)$$

There is special interest in the strength of the reflected shock at the triple point T, especially in view of the well-known difficulties of interpreting certain experimental results in Mach reflection. According to reference 3, $K(\theta)$ in Eq. (17) is zero at T, so the strength of the reflected shock vanishes there. We conclude, therefore, that while this shock is $O(\vartheta^2)$ over the rest of its front, it can be at most $O(\vartheta^2)$ at T.

It is also of interest to determine the angle at which the reflected shock meets the main shock at T. The question is whether this angle differs, in the second order, from the angle formed by the main shock and the accustic circle with center at 0 (Fig. 1). This can be determined from Eq. (14) above, because the second-order correction to this angle is given by the value of $dr/rd\theta$ at T. This quantity has been worked out using Lighthill's $A(\theta)$ and has been found equal to zero. Thus, the wave is not only of vanishing strength at the triple point, but it is locally tangent to the acoustic circle there.

REFERENCES

[1] Bargmann, V., *On Nearly Glancing Reflection of Shocks*. N.D.R.C. Appl. Math. Panel Report 108.2R. 1945.

[3] Ting, L., and Ludloff, H. F., *Aerodynamics of Blasts*, Readers' Forum, Journal of the Aeronautical Sciences, Vol. 18, No. 2, p. 143, February, 1951.
[3] Lighthill, M. J., *The Diffraction of Blast, I*, Proc. Roy. Soc. A, Vol. 198, pp. 454–470, 1949.
[4] Lighthill, M. J., *The Shock Strength in Supersonic Conical Fields*, Phil. Mag., Ser. 7, Vol. XI, p. 1202, December, 1949.

A Simple Rule for the Velocity Rise with Subsonic Mach Number on Ellipsoids of Revolution

D. Küchemann,
Royal Aircraft Establishment, Farnborough, Hants, England
July 17, 1951

THE SUBSONIC COMPRESSIBLE FLOW over a slender body of revolution can be determined to a first approximation from the Prandtl-Glauert method in the form of the "streamline analogy" by Busemann[1] and Göthert.[2] The velocity increment v_x, in the direction of the main stream, in compressible flow is $1/\beta^2$ times the velocity increment v_{xa} in incompressible flow on an analogous body, obtained by reducing the lateral dimensions of the original body in the ratio $\beta:1$. $\beta = \sqrt{1 - M_0^2}$, and M_0 is the free-stream Mach Number. The problem thus becomes that of finding a relation between the velocity increment v_{xa} of the analogous body and the velocity increment v_{xi} of the given body, both in incompressible flow.

From the results of exact solutions by various authors[3, 4] for the maximum velocity increment on ellipsoids of revolution in incompressible flow we find that the relation

$$v_{xi} = 0.645\delta^{3/2}$$

is a reasonable approximation up to a fineness ratio $\delta = D/L$ of about 0.3. This is shown in Fig. 1. Hence,

$$v_{xa} = 0.645(\beta\delta)^{3/2} = \beta^{3/2}v_{xi}$$

so that

$$v_x = (1/\beta^2)v_{xa} = (\beta^{3/2}/\beta^2)v_{xi}$$

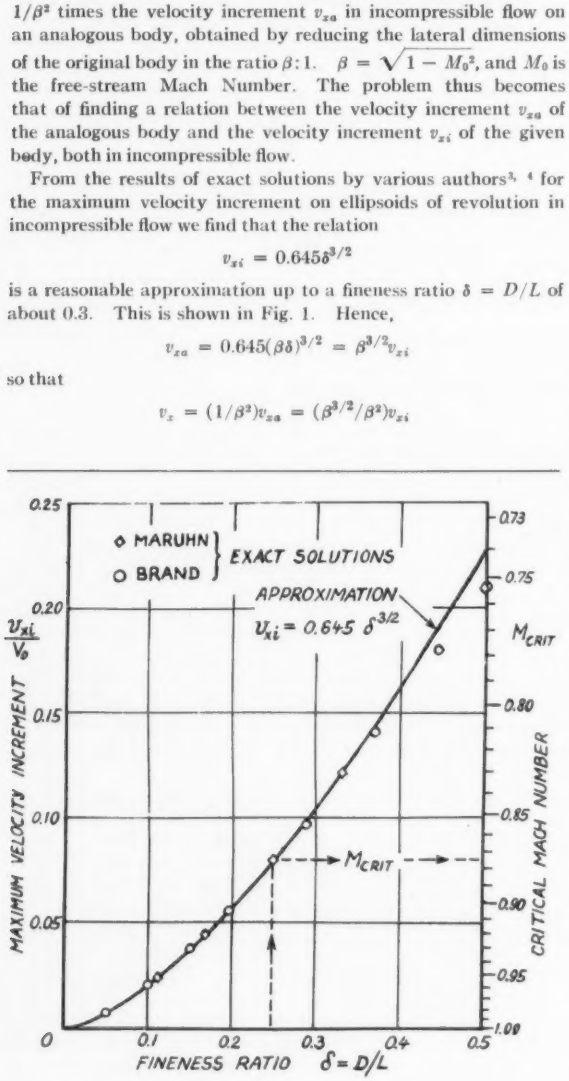

FIG. 1.

and finally,

$$\frac{v_x}{v_{xi}} = \frac{C_p}{C_{pi}} = \frac{1}{\sqrt{\beta}} = \frac{1}{\sqrt[4]{1 - M_0^2}}$$

assuming the usual linearized relation between the pressure coefficients $C_p = (p - p_0)/q_0$ and the corresponding velocity increments. It will be found that this relation agrees well with experimental results.

v_x or C_p can be used to find $M_{crit.}$, the value of the free-stream Mach Number at which sonic speed is reached locally on the body. A scale for $M_{crit.}$ obtained in this way is added to the right of the figure, which thus provides a simple means of estimating the greatest free-stream Mach Number at which ellipsoids of revolution of known fineness ratio will be free from compressibility disturbances.

REFERENCES

[1] Busemann, A., *Profilmessungen bei Geschwindigkeiten nahe der Schallgeschwindigkeit*, Jahrbuch der Wiss. Ges. f. Luftfahrt, 1928.
[2] Göthert, B., *Ebene und räumliche Strömung bei hohen Unterschallgeschwindigkeiten*, Jahrbuch der Deutschen Luftfahrtforschung, p. I 156, 1941.
[3] Maruhn, K., *Druckverteilungsrechnungen an elliptischen Rümpfen und in ihrem Aussenraum*, Jahrbuch der Deutschen Luftfahrtforschung, p. I 135, 1941.
[4] Brand, M., *Druckverteilungen von Rotationskörpern bei axialer Anströmung*, Deutsche Luftfahrtforschung UM 3206, 1944. Translation, Brit. Min. of Supply GDC 10/5489T.

On Slender Wing Theory

John W. Miles*
Fulbright Lecturer, Auckland University College, Auckland, New Zealand
August 29, 1951

STEWARTSON[1] HAS RECENTLY PUBLISHED an analysis of the supersonic flow over a low aspect ratio rectangular wing. His results (a) prove that the slender-wing theory, first applied by Jones[2] to pointed wings, does give the correct lift coefficient for the rectangular wing, albeit not pointed, in the limit of zero aspect ratio and (b) furnish the pressure distribution aft of the regions where the results of Gunn[3] and Lagerstrom[4] are applicable. However, he does not calculate the lift and moment coefficients for other than zero aspect ratio.

An alternative approach to the boundary value problem is to separate the Laplace transform of the potential equation in elliptic coordinates and exhibit the solution as an expansion in Mathieu functions, following the classical analysis of diffraction around a flat strip.[5] With the exception of minor numerical discrepancies, the results are in agreement with those obtained by Stewartson, and we present here only the expressions for the lift and moment coefficients.

Let A.R. be the geometrical aspect ratio, A the effective aspect ratio, viz.,

$$A = (M^2 - 1)^{1/2}\text{A.R.} \qquad (1)$$

and C_L and C_M the lift and moment coefficients (with respect to the leading edge and with the chord as a reference moment arm); then

$$C_L = \pi\text{A.R.}/2\,\{1 + (1/16)A^2 - (3/64)\,[\ln(8/A) - (29/24)]\times A^4 - 1.17\exp(-1.364/A)\cos[(2.22\,8/A) + 0.275]\} \qquad (2)$$

$$C_M = \pi\text{A.R.}/2\,(-(1/8)A^2 + (1/16)\,[\ln(8/A) - (9/8)]A^4 + \exp(-1.364/A)\,\{1.17\cos[(2.22\,8/A) + 0.275] + 0.45A\cos[(2.228/A) + 1.296]\}) \qquad (3)$$

* On leave from University of California, Los Angeles.

The expansions of which Eqs. (2) and (3) give the leading terms are semiconvergent and represent the true results only in an asymptotic sense. In addition to terms of order $A^6 \ln^2 A$, exponential terms are neglected,[1] since only one pole of the Laplace transform has been determined accurately.

The approximation given by Eq. (2) agrees with the exact result $\{C_L = 4(M^2 - 1)^{-1/2}[1 - (2A)^{-1}]\}$ to better than 0.1 per cent at $A = 1$ and is indistinguishable from Lagerstrom's result at $A = 1/2$. The agreement of Eq. (3) with the exact results is, of course, less satisfactory but is within 3 per cent at $A = 1$.

The foregoing results are to be compared with those recently obtained by Lomax and Sluder.[6] Comparison of Eqs. (2) and (3) with the exact results of reference 4 in $1/2 \leq A \leq 1$ establishes Stewartson's analysis as the more accurate.

REFERENCES

[1] Stewartson, K., *Proc. Cambr. Phil. Soc.*, Vol. 46, p. 307, 1950.
[2] Jones, R. T., N.A.C.A. T.R. No. 835, 1946.
[3] Gunn, J. C., *Phil. Trans. Roy. Soc. Lon. (A)*, Vol. 240, p. 327, 1947.
[4] Lagerstrom, P. A., Douglas Aircraft Company Rep. SM-13110, Santa Monica, 1947.
[5] Sieger, B., *Ann. d. Physik*, Vol. 27, p. 626, 1908.
[6] Lomax, H., and Sluder, L., N.A.C.A. T.N. No. 2295, 1951.

Proper Use of the M.I.T. Tables for Supersonic Flow Past Inclined Cones

Antonio Ferri*
Langley Aeronautical Laboratory, N.A.C.A., Langley Air Force Base, Va.

July 27, 1951

IN THE MAY, 1951, issue of the JOURNAL OF THE AERONAUTICAL SCIENCES, a letter with the same title was published from Van Dyke, Young, and Siska of the RAND Corporation, in which expressions for the values of velocity components, density, and pressure at the surface of a conical, circular body were given as function of the values given by the M.I.T. tables.

The expressions given are not valid for the components of velocity and for the density at the surface of the cone but are values outside a vorticose layer existing near the body.[1]

The entropy at the surface of the body must be constant because the flow at the body follows a streamline, and, therefore, Eqs. (1e) and (2e) are not physical at the surface of the body. Near the surface of the body, a vorticose layer exists of zero thickness in the first-order approximation and of a thickness of the order of ϵ when terms in ϵ^2 are retained. Across the layer a variation of entropy occurs from a value

$$S = S_a + \epsilon \sum Sn \cos n\phi + \epsilon^2 \sum Sn \cos n\phi$$

to a constant value

$$S' = S_a + \epsilon S_b + \epsilon^2 S_c$$

The entropy changes the velocity components and density at the surface, and the expressions (2a), (2b), (2c), and (2e) are valid only outside the layer. However, the layer in the first approximation has zero thickness and, therefore, does not produce changes in pressure. When terms of the order of ϵ^2 are retained, expressions of the form

$$p = \bar{p} + \epsilon \sum \eta_n \cos n\phi + \epsilon^2 \sum p_n \cos n\phi$$

$$\rho = \bar{\rho} + \epsilon \sum \xi_n \cos n\phi + \epsilon^2 \sum \rho_n \cos n\phi$$

would produce an entropy distribution at the surface of the form

$$S = S_a + \epsilon S_b \cos \phi + \epsilon^2 \sum S_c \cos n\phi$$

which again is not physical.

The expression of the pressure Eq. (2d) is valid at the surface of the body and is consistent with the approximation accepted for $\epsilon \to 0$; however, it is not sufficient when small but finite angles of attack are considered. In this case, the pressure must be obtained from the complete expression of the velocity.[1] Indeed,

$$V^2 = u_0^2 + 2u_1 u_{0\epsilon} \cos \phi + \epsilon^2 w_1^2 + u_1^2 \epsilon^2 \cos^2 \phi + \text{other terms in } \epsilon^2$$

Now, in Eq. (2d), the terms $\epsilon^2 w_1^2 \sin^2 \phi$ and $u_1^2 \epsilon^2 \cos^2 \phi$ are considered small with respect to $2u_1 u_{0\epsilon} \cos \phi$, which is the only term retained. However, at the surface of the body,

$$\epsilon^2 w_1^2 = -\epsilon^2 u_1^2 / \sin^2 \theta_s$$

and for finite angles of attack, $\epsilon / \sin^2 \theta_s$ is of the order of one. For example, for $\theta_s = 10°$, $\epsilon / \sin^2 \theta_s = 1$ for $\alpha = 1.75°$; therefore, for finite angles of attack, this term must be retained.

REFERENCE

[1] Ferri, Antonio, *Supersonic Flow Around Circular Cones at Angles of Attack*, N.A.C.A. T.N. No. 2236, November, 1950.

* At the present time, Professor of Aerodynamics, Polytechnic Institute of Brooklyn.

Visualization of Boundary-Layer Flow

James S. Murphy and Ralph E. Phinney
Research Associates, Engineering Research Institute, University of Michigan

August 30, 1951

A TECHNIQUE FOR VISUALIZATION of boundary-layer flow has been developed at the University of Michigan Vacuum Type Supersonic Wind Tunnel. The technique was developed during experimental investigations on location of boundary-layer transition[1] by the "China-clay"[2] and "liquid-film"[3, 4] techniques and may be designated as a "China-film" technique, since it is a hybrid of these methods. A wide variety of applications of the technique is evident. It has been used in shock-reflection studies[5] to give indications of boundary-layer streamline directions and information about the line of impingement of a shock wave on a solid surface. In addition, proper application of the technique will yield useful information concerning location of boundary-layer transition, regions of separated flow, tunnel blocking, interference effects, etc.

The technique has its most fruitful application where three-dimensional boundary-layer effects near a surface are large, such as in the neighborhood of a three-dimensional shock reflection from a surface. The position of shock reflection from a surface may become visible in two ways: first, through the sharp change in streamline direction (unless the reflection is strictly two-dimensional, in which case there is no streamline curvature) or second, through the existence of a distinct streak under the shock (presumably due to sharp shear-stress change under the shock foot or a separation bubble). For indicating streamline direction, this method has the advantage over tufts in that there is no flutter problem and a permanent pattern remains on the surface which may be examined and photographed after a run.

Examples of the patterns obtained by use of the method are shown in Figs. 1, 2, and 3. Fig. 1 indicates the streamline pattern on the tunnel floor associated with tunnel blocking. In Fig. 2, the square body has been rotated approximately 45° from its position during the run. The two lines on the wedge are the re-reflection of the wedge shock from the body (where it splits into

two waves). Fig. 3 shows the indication of boundary-layer transition on a flat plate. Oblique lighting was used to obtain this photograph. The others were taken with direct light.

The method requires the preparation of a suspension of China-clay particles in a bonding agent and a volatile liquid that has the proper drying time. A more precise description of the mixture will be given below. Shortly after preparation, a layer of the suspension is applied to the surface to be investigated. A free application by hand to the surface, such that the surface feels oily but the liquid does not run, yields a layer giving a good flow pattern that does not interfere noticeably with the external flow.

After application of the suspension, flow is established over the surface. During the initial period of flow, the volatile liquid is carried along the surface by the action of shear stresses in the boundary layer. As time progresses, the volatile liquid evaporates, leaving the china-clay particles attached to the surface by the bonding agent. These particles are arranged in streaks having approximately the direction of the streamlines in the boundary layer near the surface. In order to provide for a good photograph, it is desirable that the surface be black (see Figs. 1, 2, and 3) so as to contrast with the white China-clay particles. For steel surfaces, treatment with a chemical gun blueing has proved satisfactory.

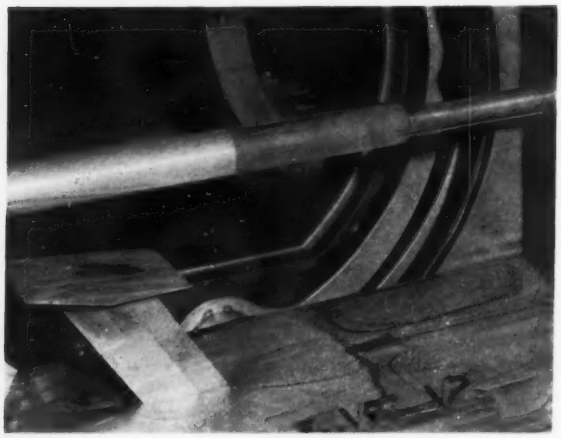

FIG. 1.

FIG. 2.

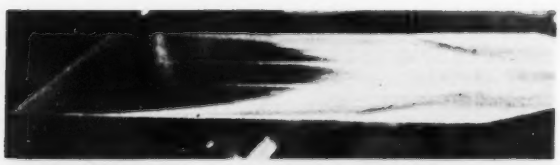

KEY: Dark (wet) surface shows extent of laminar layer
White (dry) surface indicates turbulent layer

FIG. 3.

The suspension may be prepared in the following manner. The bonding agent is attached to the china-clay particles by making a lacquer similar to that in reference 2 or 5. Mixture of this lacquer with a volatile liquid in the ratio of one part lacquer to five parts volatile liquid by volume will give a sufficiently dense suspension of particles. The mixture should not be prepared too far in advance of use, since the China-clay particles tend to coagulate and form a sludge that causes the streamlines to be less distinct.

Choice of volatile liquid is dependent upon the drying time required in a particular application. Reference 2 gives a list of suitable liquids covering a large range of drying times. For a vacuum type supersonic tunnel having an atmosphere stagnation pressure, methyl salicylate and iso-safrole and mixtures of these liquids have been used successfully. For example, at $M = 1.90$, a mixture of one part iso-safrole and three parts methyl salicylate by volume gives a drying time of approximately 30 sec. in regions of laminar flow and 12 sec. in regions of turbulent flow. In such a tunnel, the effect of transient starting conditions on flow of the volatile liquid is negligible, since the transients exist for less than 2 sec. while the steady flowing period is of the order of 15 sec. For continuous tunnels, the effect of transients is more pronounced, and, consequently, a volatile liquid having a longer drying time must be used.[2]

REFERENCES

[1] Murphy, J. S., *Study of Experimental Methods for Determining Location of Transition on Models in the Intermittent Supersonic Wind Tunnel*, Univ. of Mich. WTM-182, October, 1950.

[2] Richards, M. A., and Burstall, F. H., *The China-Clay Method of Indicating Transition*, British R. and M. No. 2126, August, 1945.

[3] Gray, W. E., *A Simple Visual Method of Recording Boundary Layer Transition*, R.A.E. Tech. Note Aero. 1816, August, 1946.

[4] Liepmann, H. W., Roshko, A., and Dhawan, S., *On Reflection of Shock Waves from Boundary Layers*, N.A.C.A. T.N. No. 2334, April, 1951.

[5] Gazely, C., Jr., *The Use of the China-Clay Lacquer Technique for Detecting Boundary Layer Transition*, General Electric Report No. R49A0536, March, 1950.

[6] Morkovin, M. V., Migotsky, E., Bailey, H. E., and Phinney, R. E., *Experiments on Interaction of Shock Waves and Cylindrical Bodies at Supersonic Speeds*, to be published in the Journal of the Aeronautical Sciences.

Local Compressible Pressure Coefficient

V. G. Szebehely
Associate Professor of Research, Virginia Polytechnic Institute

July 23, 1951

IN A RECENT NOTE, Laitone[1] suggests the use of the local Mach Number for computing compressible pressure coefficient and obtains his formula [Eq. (2)] by "analytical continuation." Based on *physical* considerations, the relation between compressible and incompressible pressure coefficients,

$$C_p = C_{p0}/\sqrt{1 - M_L^2}$$

was derived by Truitt.[2, 3] In a thesis[4] under the writer's supervision, the result was compared with experimental data for airfoils and with the von Kármán-Tsien relation. It is interesting to note that the method does not offer always and everywhere on the

surface better results than the von Kármán-Tsien formula. In fact, good agreement was found[5] with experiments around the nose of the airfoil using the formula above. Between 20 and 70 per cent chord points, however, on the upper surface of the NACA airfoil (4412) at $M_\infty = 0.603$ and $\alpha = -2°$, the above formula overestimates the experimental values. Generally, the method appears to predict closer to the experimental values for pressure coefficients that are relatively large.[6]

REFERENCES

[1] Laitone, E. V., *New Compressibility Correction for Two-Dimensional Subsonic Flow*, Readers' Forum, Journal of the Aeronautical Sciences, Vol. 18, No. 5, p. 350, May, 1951.

[2] Truitt, R. W., *North Carolina State College Bulletin No. 44*, 1949.

[3] Truitt, R. W., *North Carolina State College Bulletin No. 47*, 1950.

[4] Truitt, R. W., Thesis submitted for the Degree of Master of Science in Applied Mechanics, Virginia Polytechnic Institute, 1950.

[5] Truitt, R. W., and Szebehely, V. G. Paper presented before the Virginia Academy of Science, May, 1950 and abstracted in the Virginia Journal of Science, Vol. 1, No. 4, p. 377, September, 1950.

[6] Truitt, R. W., Virginia Journal of Science, Vol. 2, No. 2, pp. 94-101, April, 1951.

The Effect of Compressibility of the Material on Plastic Buckling Stresses

Elbridge Z. Stowell and Richard A. Pride
National Advisory Committee for Aeronautics, Langley Air Force Base, Va.

July 23, 1951

IN THE ORIGINAL N.A.C.A. computation of plastic buckling stresses,[1] they were taken to be of the form

$$\sigma_{cr} = \eta\{\pi^2 kE/[12(1-\nu^2)]\}(t/b)^2$$

in which ν is the value of Poisson's ratio which applies in the elastic range of the material and η is the plasticity coefficient applicable to the problem in hand. The η-coefficients were calculated by dividing the plastic buckling stress by the buckling stress that would be obtained if the material remained elastic, with Poisson's ratio taken equal to 1/2 in both stresses for this purpose. In other words, the material was taken to be incompressible as far as the computation of η was concerned, with the result that a small error was introduced into the coefficient η.

In order to obtain an estimate of the magnitude of this error in the η-coefficients, the calculation of plastic buckling stresses has been repeated with allowance made for compressibility of the material. The stress-strain relations used were those of Hencky:

$$\sigma_x = [E_{sec}/(1-\mu^2)](\epsilon_x + \mu\epsilon_y)$$

$$\sigma_y = [E_{sec}/(1-\mu^2)](\epsilon_y + \mu\epsilon_x)$$

$$\tau = E_{sec}\gamma/[2(1+\mu)]$$

where μ is a composite Poisson's ratio of magnitude

$$\mu = (1/2) - [(1/2) - \nu](E_{sec}/E)$$

The resulting expressions for plastic buckling stresses are: for the simply-supported flange

$$\sigma_{cr} = \{\pi^2 kE_{sec}/[12(1-\mu^2)]\}(t/b)^2$$

for the simply-supported plate (with $k = 4$)

$$\sigma_{cr} = \left[\frac{1}{2} + \frac{1}{2}\sqrt{\mu^2 + (1-\mu^2)\frac{E_{tan}}{E_{sec}}}\right]\frac{\pi^2 E_{sec}}{3(1-\mu^2)}\left(\frac{t}{b}\right)^2$$

The trial and error process now requires, in the case of the flange, the use of E_{sec} and μ and, in the case of the plate, the three quantities E_{sec}, E_{tan}, and μ, corresponding to each assumed σ_{cr} until the respective equations are satisfied.

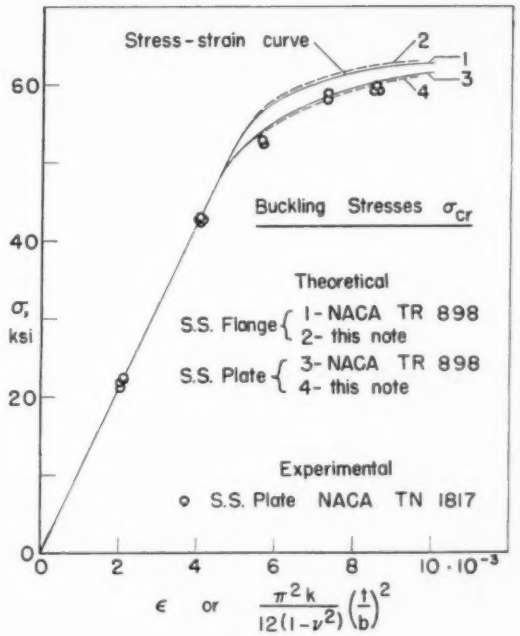

FIG. 1.

The results of such calculations for the 14S-T6 aluminum alloy used in the plastic buckling tests[2] are shown in the figure. The effect of compressibility is to raise the buckling stress for the flange by about 1/2 k.s.i. in 60 and to lower the buckling stress for the plate by about the same amount. Thus, the error in using the original formulas for η is of the order of 1 per cent for this material.

There is no error in using E_{tan}/E as the η-coefficient for a long column.

REFERENCES

[1] Stowell, Elbridge Z., *A Unified Theory for Plastic Buckling of Columns and Plates*, N.A.C.A. Rep. No. 898, 1948.

[2] Pride, Richard A., and Heimerl, George J., *Plastic Buckling of Simply Supported Compressed Plates*, N.A.C.A. T.N. No. 1817, 1949.

An Integral Relation from the Turbulent Energy Equation

Stanley Corrsin
Department of Aeronautics, The Johns Hopkins University

August 14, 1951

FOLLOWING VON KÁRMÁN,[1] integral relations for *mean motion* have found wide application in both laminar and turbulent shear flows of "boundary layer type." The purpose of this note is to demonstrate an integral relation deducible from the "boundary-layer form" of the turbulent energy equation.

For steady state with two-dimensional mean motion,[2]

$$\frac{1}{2}\bar{U}\frac{\partial\overline{q^2}}{\partial x} + \frac{1}{2}\bar{V}\frac{\partial\overline{q^2}}{\partial y} = -\overline{uv}\frac{\partial\bar{U}}{\partial y} - \frac{\partial}{\partial y}\left\{\overline{v\left(\frac{1}{2}q^2 + \frac{p}{\rho}\right)}\right\} + \frac{\nu}{2}\frac{\partial^2\overline{q^2}}{\partial y^2} - \nu\overline{\left(\frac{\partial u_i}{\partial x_k}\right)\left(\frac{\partial u_i}{\partial x_k}\right)} \quad (1)$$

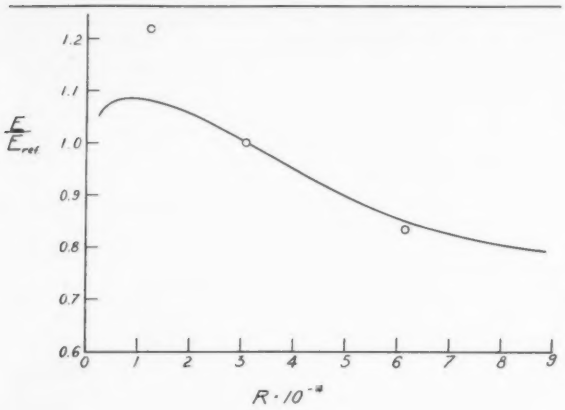

FIG. 1.

where x is the principal flow direction ($\bar{U}$, u); q^2 is the resultant turbulent velocity ($= u^2 + v^2 + w^2$); p is static pressure fluctuation; ρ is density; ν is kinematic viscosity; and the last term is in Cartesian tensor notation, with repeated index indicating summation. The bar denotes average.

Integration of (1) in the y-direction across a shear flow, between boundaries $a(x)$ and $b(x)$, gives

$$\frac{1}{2}\frac{d}{dx}\int_{a(x)}^{b(x)} \bar{U}\bar{q}^2\,dy = -\int_{a(x)}^{b(x)} \overline{uv}\frac{\partial \bar{U}}{\partial y}\,dy - \nu\int_{a(x)}^{b(x)} \overline{\left(\frac{\partial u_i}{\partial x_k}\right)\left(\frac{\partial u_i}{\partial x_k}\right)}dy \quad (2)$$

The first term is x-rate of increase in rate of flow of energy; the last two are total production and dissipation, respectively. Convection disappears, since it is zero at axes of symmetry and/or at edge boundaries, the latter by ordinary choice of boundary.

For sufficiently large Reynolds Numbers, dissipation occurs chiefly in the locally isotropic part of the spectrum, and the last integrand can be approximated by Taylor's isotropic dissipation expression[3]

$$\overline{(\partial u_i/\partial x_k)\,(\partial u_i/\partial x_k)} = 5\overline{q^2}/\lambda^2$$

where λ is the "microscale."

As an example, consider the application of Eq. (2) to prediction of λ in a "half-jet" of the type studied in reference 4, with the additional assumption of similarity (with x) in the turbulent as well as the mean motion and the empirical fact that λ is independent of y in the fully turbulent region. Liepmann and Laufer have used mean motion integral relations and mean flow similarity to demonstrate the linear spread of this particular turbulent shear flow, $a \sim b \sim x$. With the similarity statements [$\bar{U} = \bar{U}_{max.}\cdot f(\eta)$; $\overline{q^2} = \bar{U}_{max.}^2\cdot g(\eta)$ and $\overline{uv} = \bar{U}_{max.}^2\cdot h(\eta)$, where $\eta \sim y/(b-a) \sim y/x$], and with local isotropy, Eq. (2) gives

$$\lambda = [(\nu/A\,\bar{U}_{max.})\cdot x]^{1/2} \quad (3)$$

where A is a numerical constant, dependent upon various integral functions of f, g, and h.

This parabolic variation of λ is in rough agreement with the experimental results given in Fig. 35 of reference 4.

A rough estimate by von Kármán[2] from the differential form of the turbulent energy equation gives $q_0'\lambda^2 \sim \nu\delta$, where δ is a length proportional to the shear region width and q_0' is a measure of the root mean square turbulent velocity. For the particular case of the "half-jet," $\delta \sim x$ and $q_0' = $ const., so that $\lambda \sim x^{1/2}$, as pointed out by Liepmann and Laufer.

In fact, von Kármán's process of dimensional reasoning and estimation in reference 2 is qualitatively the same as using an integral relation plus similarity assumptions.

The second example is an estimate of the change in average turbulence level in fully developed turbulent channel flow as a function of Reynolds Number. With $a(x)$ and $b(x)$ equal to $\pm H$ (the channel boundaries) and the replacement of $\overline{uv}$ in Eq. (2) by its expression in the momentum equation [Eq. (2) in reference 5], there results

$$5\nu\int_{-H}^{H}\frac{\bar{q}^2}{\lambda^2}\,dy = -\frac{1}{\rho}\frac{\partial \bar{P}}{\partial x}\int_{-H}^{H}\bar{U}\,dy - \nu\int_{-H}^{H}\left(\frac{d\bar{U}}{dy}\right)^2 dy \quad (4)$$

which says that the total energy dissipated to heat by the turbulence equals the total rate at which energy is fed into the flow by pressure work minus the energy dissipated directly without passing through the turbulent state. A dimensionless measure of the average turbulent dissipation across the channel follows directly:

$$\frac{10H}{\bar{U}_{max.}^2}\int_{-H}^{H}\frac{\bar{q}^2}{\lambda^2}\,dy = I_1\cdot R\cdot c_f - I_2 \quad (5)$$

where

$$I_1 = \int_{-1}^{1} f(\eta)\,d\eta$$

$$I_2 = \int_{-1}^{1} (df/d\eta)^2\,d\eta$$

$$f = \bar{U}/\bar{U}_{max.}$$

$$\eta = y/H$$

$$R = \bar{U}_{max.}H/\nu$$

$$c_f = \frac{2\tau_0}{\rho\bar{U}_{max.}^2} = -\frac{2H(\partial\bar{P}/\partial x)}{\rho\bar{U}_{max.}^2}$$

$$\tau_0 = \mu\left|d\bar{U}/dy\right|_{y=\pm H}$$

For an estimate of the R-variation in

$$E \equiv (2\bar{U}_{max.}^2 H)^{-1}\int_{-H}^{H}\overline{q^2}\,dy$$

consider λ roughly constant across the channel[5] and estimate $c_f(R)$ from the Blasius calculation on data in tubes;[6] this gives $c_f \approx 0.05R^{-1/4}$. With a (1/7)-power turbulent region and linear sublayer (of thickness ϵ), $I_1 \approx 1.75$ and $I_2 \approx 2(H/\epsilon)^{5/7} \approx 0.1R^{5/8}$, and Eq. (5) becomes

$$E \sim R^{5/8}(\lambda/H)^2(R^{1/8} - 2.0) \quad (6)$$

With the von Kármán estimate mentioned earlier, $(H/\lambda)^2 \sim R$. Therefore,

$$E \sim R^{-3/8}(R^{1/8} - 2.0) \quad (7)$$

which should be roughly true for extremely large R. Note that $E = 0$ for $R \approx 260$, probably the same order as the lower critical R for channel flow. In fact this example partly resembles the Reynolds energy method for estimating this limit.[7] Fig. 1, with ordinate normalized at $R = 30{,}800$, gives a comparison of Eq. (7) with the Laufer data.[5]

REFERENCES

[1] von Kármán, Th., *Über Laminare and Turbulente Reibung*, Z.A.M.M., Vol. 1, No. 1, 1921.

[2] von Kármán, Th., *The Fundamentals of the Statistical Theory of Turbulence*, Journal of the Aeronautical Sciences, Vol. 4, No. 4, pp. 131–138, February, 1937.

[3] Taylor, G. I., *Statistical Theory of Turbulence*, Proc. Roy. Soc. A, Vol. 151, pp. 421–478, 1935.

[4] Liepmann, H. W., and Laufer, J., *Investigations of Free Turbulent Mixing*, N.A.C.A. T.N. No. 1257, 1947.

[5] Laufer, J., *Some Recent Measurements in a Two-Dimensional Turbulent Channel*, Journal of the Aeronautical Sciences, Vol. 17, No. 5, pp. 277–287, May, 1950.

[6] Blasius, H., *The Law of Similitude in Frictional Phenomena in Fluids*, Forschungsarbeit, V.D.I., Vol. 131, 1913.

[7] Reynolds, O., *On the Dynamical Theory of Incompressible Viscous Fluids and the Determination of the Criterion*, Phil. Trans. Roy. Soc. Lond. (A), Vol. 186, pp. 123–164, 1895.

Concerning Hadamard's Solution for a Source in Supersonic Flow

E. V. Laitone
Associate Professor, University of California, Berkeley
August 8, 1951

IN ANSWER TO SERBIN'S COMMENTS on the apparent sign discrepancy in the analogy of "The Source-Flow in Supersonic and Incompressible Theories,"[1] it should be pointed out that in the von Kármán-Moore integral the supersonic pseudo-source strength is proportional to S'', where $S = \pi r^2$ is the cross-sectional area of the body of revolution, while in the Hadamard solution the supersonic source strength is proportional to S', analogous to that for incompressible flow.

This is shown in reference 2 wherein Eq. (17) gives the von Kármán-Moore integral for a slender sharp nose body of revolution as

$$\frac{\phi_r}{U} = -\frac{1}{2\pi r}\int_0^{x-Br}\frac{S''(\xi)\,(\xi - x)\,d\xi}{\sqrt{(x-\xi)^2 - B^2r^2}} \tag{1}$$

and the corresponding Hadamard solution as

$$\frac{\phi_r}{U} = \frac{B^2r}{2\pi}\int_0^{x-Br}\frac{[S'(x-Br) - S'(\xi)]\,d\xi}{[(x-\xi)^2 - B^2r^2]^{3/2}} + \frac{x}{2\pi r}\frac{S'(x-Br)}{\sqrt{x^2 - B^2r^2}} \tag{2}$$

Note that Eq. (2) can be obtained either by integrating Eq. (1) by parts or directly from the Hadamard method as followed in Eq. (8) of reference 2.

The corresponding solution for linearized subsonic flow is given by Eq. (51) of reference 2 as

$$\frac{\phi_r}{U} = \frac{\beta^2 r}{4\pi}\int_0^L \frac{S'(\xi)\,d\xi}{[(x-\xi)^2 + \beta^2r^2]^{3/2}} \tag{3}$$

It is seen that only Hadamard's solution is analogous to the linearized subsonic or incompressible flow ($\beta = 1$) solution, as would be expected.

REFERENCES

[1] Serbin, H., *The Source-Flow in Supersonic and Incompressible Theories*, Readers' Forum, Journal of the Aeronautical Sciences, Vol. 18, No. 6, pp. 431–432, June, 1951.

[2] Laitone, E. V., *The Linearized Subsonic and Supersonic Flow About Inclined Slender Bodies of Revolution*, Journal of the Aeronautical Sciences, Vol. 14, No. 11, pp. 632–633, 639, November, 1947.

On the Unsteady Motion of a Thin Rectangular Wing in Supersonic Flow

N. Rott
Cornell University, Ithaca, N.Y.
August 15, 1951

UNSTEADY SUPERSONIC FLOW PROBLEMS of the rectangular wing have been solved by Miles,[1, 2] Stewartson,[3] and recently (following an idea of Gardner[4]) by Goodman.[5, 6] The following treatment is restricted to the case when the prescribed normal velocity φ_z on the wing is an arbitrary function of the chordwise ordinate x and of time t but is independent of the spanwise ordinate y. A general solution for this case will be presented, based on the potential in the corresponding two-dimensional problem.

Consider a quarter-infinite plate occupying the plane $x \geq 0$, $y \geq 0$. After introduction of polar coordinates r, ϑ in the yz-plane, the potential satisfies the equation

$$\varphi_{rr} + \frac{1}{r}\varphi_r + \frac{1}{r^2}\varphi_{\vartheta\vartheta} = (M^2 - 1)\varphi_{xx} + \frac{2M}{a}\varphi_{xt} + \frac{1}{a^2}\varphi_{tt} \tag{1}$$

The solution is obtained following a method by Lamb[7, 8] in his treatment of Sommerfeld's diffraction problem. With a slight generalization of Lamb's procedure, the following expression will be tried for the spanwise component φ_y of the velocity:

$$\varphi_y = \cos(\vartheta/2)r^{-1/2}F(x, t, r) \tag{2}$$

On the plate—i.e., for $\vartheta = 0$ and $\vartheta = 2\pi$—this yields $\varphi_{yz} = 0$, so that φ_z is a function of x and t only, in accordance with the boundary conditions stated above. Introducing Eq. (2) in Eq. (1), it follows that F satisfies

$$F_{rr} = (M^2 - 1)F_{xx} + \frac{2M}{a}F_{xt} + \frac{1}{a^2}F_{tt} \tag{3}$$

i.e., the potential equation in two spatial dimensions x and r. The spanwise flow will vanish on and outside of the Mach cone

$$r = (M^2 - 1)^{-1/2}x \equiv \alpha x$$

thus

$$F(x, t, \alpha x) = 0 \tag{4}$$

Notice that for $r \to 0$, φ_y must have a singularity of the type $r^{-1/2}$, so that $F(x, t, 0)$ must be finite.

The potential on the plate follows by integration of Eq. (2):

$$\varphi_0(x, t, y) = \int_{-\alpha x}^{y}\varphi_y\,dy = \int_0^y F(x, t, y)\frac{dy}{\sqrt{y}} \tag{5}$$

since $\varphi_y = 0$ for $\vartheta = \pi$.

It will be necessary also to express the potential $\phi(x, t, z)$ in the two-dimensional domain by integrating Eq. (2) along a line $z = \text{const.}$ between the limits given by the two intersections of this line with the Mach cone $r = \alpha x$. This integration may be performed, following Lamb,[7, 8] by the substitution $\sqrt{r}\cos(1/2)\vartheta = \eta$, a method that is also described by Bateman.[9] The result is

$$\phi(x, t, z) = \int_z^{\alpha x} F(x, t, r)\frac{dr}{\sqrt{r - z}} \tag{6}$$

This equation implies that $\phi = 0$ for $z = \alpha x$, on the limit of the disturbed region, a permissible normalization, as the limit is an equipotential surface of the disturbance potential. (If the disturbance velocity does not vanish at the limiting surface, then it is perpendicular to the latter by a general property of discontinuity surfaces.)

The functional relationship between φ_0 and ϕ as established by Eqs. (5) and (6) is sufficient to prove a significant property of the spanwise integral of φ_0 between $y = 0$ and $y = \alpha x$. (Simple expressions in special cases where obtained for this integral by Miles[1, 2] and Stewartson[3] independently.) From Eq. (5) it is found after integration by parts:

$$\int_0^{\alpha x}\varphi_0\,dy = \alpha x\int_0^{\alpha x}F(x, t, y)\frac{dy}{\sqrt{y}} - \int_0^{\alpha x}F(x, t, y)\sqrt{y}\,dy \tag{7}$$

The integral in the first term is

$$\varphi_0(x, t, \alpha x) = \phi(x, t, 0)$$

For the second term, it may be shown that

$$\int_0^{\alpha x}F(x, t, y)\sqrt{y}\,dy = \frac{1}{2}\int_0^{\alpha x}\phi(x, t, z)dz \tag{8}$$

for, substituting ϕ from Eq. (6) into the right-hand side integral, the following change in order of integration will be justified:

$$\frac{1}{2}\int_0^{\alpha x} dz \int^{\alpha x} F(x, t, r)\,\frac{dr}{\sqrt{r-z}} = \frac{1}{2}\int_0^{\alpha x} dr \int_0^{r} F(x, t, r)\,\frac{dz}{\sqrt{r-z}} \qquad (9)$$

The domain covered by this double integral in the rz-plane is a triangle with the corners $r = 0, z = 0$; $r = \alpha x, z = 0$; and $r = \alpha x, z = \alpha x$. The original form of the integral on the left-hand side of Eq. (9) requires the first (inner) integration on strips parallel to the r-axis, while the right-hand form represents the same integral first evaluated on strips parallel to the z-direction. Integration in the latter with respect to z gives

$$\frac{1}{2}\int_0^{\alpha x} dr\; F(x, t, r) \int_0^{r} \frac{dz}{\sqrt{r-z}} = \int_0^{\alpha x} F(x, t, r)\,\sqrt{r}\,dr$$

which proves Eq. (8). Inserting these results in Eq. (7), one obtains

$$\int_0^{\alpha x} \varphi_0(x, t, y)\,dy = \alpha x \cdot \phi(x, t, 0) - \frac{1}{2}\int_0^{\alpha x} \phi(x, t, z)\,dz \qquad (10)$$

Evidently in this equation "potential" may also be replaced by "pressure"; then the statement of Eq. (10) is, in words: The lift of a spanwise strip in the region of the side-edge disturbance is equal to the lift of a corresponding strip in the two-dimensional domain minus one-half of the pressure integral perpendicular to the wing at the same chordwise station in the two-dimensional domain.

The ultimate aim is to find a general connection between φ_0 and ϕ, if ϕ is given, since the two-dimensional problem may be considered as soluble. For this purpose Eq. (6) should be inverted, so that F is expressed explicitly by ϕ. For Lamb's original treatment,[8] Bateman[9] has solved this problem by Abel's inversion formula. In the present case, the solution is

$$F(x, t, r) = -\frac{1}{\pi}\int_r^{\alpha x} \phi_z(x, t, z)\,\frac{dz}{\sqrt{r-z}} \qquad (11)$$

Insertion of Eq. (11) into Eq. (6) gives an identity after the order of integration is changed in the manner described above.

Introducing, finally, Eq. (11) into Eq. (5) and changing the order of integration again, one has the final result (after integration by parts)

$$\varphi_0(x, t, y) = \phi(x, t, 0) - \frac{1}{\pi}\int_y^{\alpha x} \phi(x, t, z)\,\sqrt{\frac{y}{z-y}}\,\frac{dz}{z} \qquad (12)$$

Eq. (12) permits the calculation of the potential on the wing in the domain of three-dimensional disturbance by the use of the two-dimensional solution, which must be known in its whole field of validity. This potential, $\phi(x, t, z)$, can be determined by straightforward extension of the various methods customarily used to calculate the surface values $\phi(x, t, 0)$ only. Applied to the cases treated previously in steady and unsteady motion, the results of Eq. (10) and (12) are in agreement with known solutions. [Actually, the possibility of a general relationship as in Eq. (12) was suggested to the author by inspection of the results of references 1 to 6.]

It should be noted that the steady case permits a simpler treatment, using a general solution of Eq. (3),

$$F(x, r) = f(\alpha x - r)$$

If, moreover, a constant angle of attack is required, then φ must be conical, a condition that is fulfilled in Eq. (2) only by putting

$$f(\alpha x - r) = \text{const.}\,\sqrt{\alpha x - r}$$

The final result in this special case follows by elementary steps only.

The simplicity of the approach outlined here is obviously based on the fact that, by the use of Lamb's form, Eq. (2), the dependence of φ_y from ϑ is explicitly given by a factor $\cos(1/2)\vartheta$. It should be mentioned that the boundary conditions would be satisfied also by the more general factor $\cos[n + (1/2)]\vartheta$, but, if this is used, the differential equation for F will show that the only cases where F may be finite for $r = 0$ are $n = 0$ and $n = -1$, both giving Lamb's form. Only regular and nonvanishing functions $F(x, t, 0)$ will give the required singularity of φ_y for $r \to 0$.

References

[1] Miles, J. W., *Transient Loading of Supersonic Rectangular Airfoils*, Journal of the Aeronautical Sciences, Vol. 17, No. 10, pp. 647–652, October, 1950.

[2] Miles, J. W., *The Oscillating Rectangular Airfoil at Supersonic Speeds*, Quart. Appl. Math., Vol. 9, pp. 47–65, 1951.

[3] Stewartson, K., *On the Linearized Potential Theory of Unsteady Supersonic Motion*, Quart. Jour. Mech. & Appl. Math., Vol. 3, pp. 182–199, 1950.

[4] Gardner, C., *Time Dependent Linearized Supersonic Flow Past Planar Wings*, Com. Pure and Appl. Math., Vol. 3, 33–38, 1950.

[5] Goodman, T. R., *Aerodynamics of a Supersonic Rectangular Wing Striking a Sharp-edged Gust*, Journal of the Aeronautical Sciences, Vol. 18, No. 8, pp. 519–526, August, 1951.

[6] Goodman, T. R., *The Quarter-Infinite Wing Oscillating at Supersonic Speeds*, Cornell Aero. Lab. Rept. No. 36, 1951.

[7] Lamb, H., *On Sommerfeld's Diffraction Problem and on Reflection by a Parabolic Mirror*, Proc. London Math. Soc. (2), Vol. 4, pp. 190–203, 1906.

[8] Lamb, H., *On the Diffraction of a Solitary Wave*, Proc. London Math. Soc. (2), Vol. 8, pp. 422–437, 1910.

[9] Bateman, H., *Partial Differential Equations of Mathematical Physics*, Sect. 115, pp. 486–488; Dover, New York, 1944.